Dissertation
zur Erlangung des Doktorgrades in den Naturwissenschaften
Dr. rer. nat.

Structural Characterization and Temperature-Dependent Behavior of Layered Tungstates

vorgelegt von
Niels Hendrik Lefeld

Bremen, Mai 2023

im
Fachbereich 02 Biologie/Chemie
Universität Bremen

Für Erich

Die vorliegende Arbeit wurde an der Universität Bremen in der Arbeitsgruppe *Chemische Kristallographie fester Stoffe* von Prof. Dr. Thorsten M. Gesing im Zeitraum von Februar 2016 bis Mai 2023 angefertigt.
Änderungen der vorliegenden zur eingereichten Version sind ausschließlich orthographischer Natur.

Die elektronische Version ist unter `https://doi.org/10.26092/elib/2573` abrufbar.

Datum der Einreichung: 12. Mai 2023
Datum des Kolloquiums: 20. Juli 2023

Gutachter:

- Dr. Isaac Abrahams, School of Physical and Chemical Sciences, Queen Mary, University of London
- Prof. Dr. Claudia Weidenthaler, Pulverdiffraktometrie und Oberflächenspektroskopie, Max-Planck-Institut für Kohlenforschung

Prüfungsauschuss:

- Prof. Dr. Tim Neudecker
- Prof. Dr. Thorsten M. Gesing
- Prof. Dr. Anne Staubitz
- PD Dr. Volkmar Zielasek
- PD Dr. Michael Fischer
- Florian Bischoff

Statutory Declaration
Versicherung an Eides Statt

Ich,

Niels Lefeld,

versichere an Eides Statt durch meine Unterschrift, dass ich die vorstehende Arbeit selbständig und ohne fremde Hilfe angefertigt und alle Stellen, die ich wörtlich dem Sinne nach aus Veröffentlichungen entnommen habe, als solche kenntlich gemacht habe, mich auch keiner anderen als der angegebenen Literatur oder sonstiger Hilfsmittel bedient habe.

Ich versichere an Eides Statt, dass ich die vorgenannten Angaben nach bestem Wissen und Gewissen gemacht habe und dass die Angaben der Wahrheit entsprechen und ich nichts verschwiegen habe.

Die Strafbarkeit einer falschen eidesstattlichen Versicherung ist mir bekannt, namentlich die Strafandrohung gemäß § 155 StGB bis zu drei Jahren Freiheitsstrafe oder Geldstrafe bei vorsätzlicher Begehung der Tat bzw. gemäß § 161 Abs. 1 StGB bis zu einem Jahr Freiheitsstrafe oder Geldstrafe bei fahrlässiger Begehung.

Bremen,

Summary

The presented thesis contains the characterization of layered tungstate compounds of the Aurivillius- and Ruddlesden-Popper-type. Both structure types are part of the extensive perovskite family. In the introduction a thorough review of the relevant structure types, their similarities, differences and relationships is given. Especially the distorted coordination spheres and temperature-dependent phase transitions in the Aurivillius compounds are discussed.

The first part of the thesis deals with the Aurivillius-type bismuth tungstate Bi_2WO_6. It was studied by temperature dependent X-ray powder diffraction and Raman spectroscopy supported by DSC.

The compound was studied in the 80 K to 1100 K with a 10 K resolution. The structure models obtained from Rietveld refinement of the diffraction data suffered from large uncertainties on the oxygen positions. An in-depth analysis of the coordinations were performed nonetheless, to probe for trends in the data that show correlations to the previously reported features and up until now undetected features. The coordination spheres were analyzed by the minimal bounding ellipsoid method. The approach consists of calculating the smallest ellipsoid that encompasses all ligand around a central atom. The trends in the obtained parameters confirmed the literature results and gave hints to further structural instabilities in the temperature range 250 K to 700 K.

In the second part, the structure of the Ruddlesden-Popper-type hydrotungstate $H_2W_2O_7$ has been investigated. The compound is known for over 20 years, and although the general idea of the structure has been established from early on, the compound received only little attention in the literature and no structure solution was reported.

$H_2W_2O_7$ is synthetically only accessible via a leaching synthesis from the parent Aurivillius phase $Bi_2W_2O_9$. Since the leaching synthesis results in a highly distorted product and no single crystals of this compound are known, $H_2W_2O_7$ defied a structure solution.

The application of typical powder structure solution approaches turned out to be futile. Some problems associated with the low amount of structural information from X-ray diffraction were partially mitigated by experiments wit neutron radiation. Further ancillary probes like Raman, FTIR and NMR spectroscopy were used to shed light on structural peculiarities and aid the structure solution. From this compound knowledge several structure models were produced and tested simultaneously against neutron and X-ray data in a combined refinement approach. The obtained results were analyzed with regard to a series of quantifiers of structural distortion and compared to parent and related compounds as well as a recently published structure

solution of the compound. It became clear that the distorted nature of the sample challenged the notion of a periodic structure and kept eluding a proper description by standard diffraction.

To get further insight into formation of the distorted structures the leaching process was investigated. In-situ Raman spectroscopy and total scattering experiments were performed to describe the compound on the local range via PDF analysis. The experiments confirmed that the structural integrity of the perovskite layer is kept during the leching.

Zusammenfassung

Die vorliegende Arbeit beschäftigt sich mit der Charakterisierung von Wolframat-Schichtstrukturen vom Aurivillius- und Rudllesden-Popper-Typ. Beide Strukturtypen sind Teil der weitläufigen Perovskit-Strukturfamilie. In der Einleitung wird ein gründlicher Überblick in die relevanten Strukturen, ihre Gemeinsamkeiten, Unterschiede und Zusammenhänge gegeben. Insbesondere werden die verzerrten Koordinationssphären und das temperaturabhängige Phasenverhalten der Aurivillius-Verbindungen beleuchtet.

Das erste Teil der Arbeit beschäftigt sich mit dem Aurivllius-typ Bismuthwolframat Bi_2WO_6. Dieses wurde mittels temperaturabhängiger Röntgepulverbeugung und Raman-Spektroskopie sowie Differential-Thermoanalyse untersucht.

Die Verbindung wurde im Temperaturbereich von 80 bis 1110 Kelvin mit 10 Kelvin Auflösung untersucht.

Die Strukturmodelle, die durch die Rietveld-Verfeinerung der Beugungsdaten gewonnen wurden, litten unter großen Unsicherheiten in den Sauerstoffpositionen. Dennoch wurde eine eingehende Analyse der Koordinationen durchgeführt, um nach Trends in den Daten zu suchen, die Korrelationen zu den zuvor berichteten Merkmalen und bisher unentdeckten Merkmalen zeigen. Die Koordinationssphären wurden mit der Methode des kleinsten umhüllenden Ellipsoiden analysiert. Der Ansatz besteht darin, das kleinste Ellipsoid zu berechnen, das alle Liganden um ein Zentralatom umfasst. Die Trends in den erhaltenen Parametern bestätigten die Literaturergebnisse und gaben Hinweise auf weitere strukturelle Instabilitäten im Temperaturbereich von 80 bis 1110 Kelvin

Im zweiten Teil der Arbeit wurde die Struktur des Ruddlesden-Popper-typ Hydrowolframats $H_2W_2O_7$ untersucht. Obwohl die Verbindung seit über zwanzig Jahren bekannt ist die generelle Idee des strukturell Aufbaus bekannt war, erhielt es nur wenig Beachtung in der Literatur und ließ eine Strukturlösung vermissen.

$H_2W_2O_7$ ist nur über eine säurebasierte Auslaugreaktion aus dem Aurivillius-typ $Bi_2W_2O_9$ darstellbar. Da das Produkt der Synthese stark verzerrt und auch sonst keine Einkristalle der Verbindung bekannt sind, hat es sich seither einer Stukturlösung entzogen.

Die Anwendung typischer Pulverstrukturlösungsansätze erwies sich als aussichtslos. Einige Probleme, die mit der geringen Menge an strukturellen Informationen aus der Röntgenbeugung verbunden sind, konnten teilweise durch Experimente mit Neutronenstrahlung umgangen werden.

Weitere Hilfssonden wie Raman-, FTIR- und NMR-Spektroskopie wurden verwendet, um strukturelle Besonderheiten zu beleuchten und die Strukturlösung zu unterstützen. Aus diesem Wissen über Verbindungen wurden mehrere Strukturmodelle

erstellt und gleichzeitig gegen Neutronen- und Röntgendaten in einem kombinierten Verfeinerungsansatz getestet. Die erhaltenen Ergebnisse wurden im Hinblick auf eine Reihe von Verzerrungsmerkmalen analysiert und mit Ausgangs- und verwandten Verbindungen sowie einer kürzlich veröffentlichten Strukturlösung der Verbindung verglichen.

Es wurde deutlich, dass die verzerrte Natur der Probe die Vorstellung einer periodischen Struktur in Frage stellte und sich immer wieder einer korrekten Beschreibung durch Standardbeugungsmethoden entzog.

Acknowledgements

I would like to express my deep gratitude to my supervisors Prof. Dr. Thorsten M. Gesing and PD Dr. M. Mangir Murshed for the acceptance of my project proposal, the provision of facilities to pursue it and their scientific guidance throughout its course. I especially appreciate them for dealing with my stubbornness and not giving up on me.

Furthermore, my thanks go out to all past and current members of the *Chemische Kristallographie fester Stoffe* group, in particular Mathias, for bumping ideas, helping each other out, great lunch breaks and overall putting a huge cherry on top of my time in the group.

I would like to thank my collaborators, who aided me in the collection of vital data. In particular Lkhamsuren Bajarayagal, Uni Frankfurt, tested for SHG; Volodimir Baran, MLZ/TU München, measured NPD; Patrick Bottke, Uni Oldenburg, measured NMR; Wilke Dononelli, Uni Bremen, calculated the DFT+PDF models; Li exchange and CV measurements were done by Michael Gockeln, Fraunhofer IFAM; Volker Kahlenberg, Uni Innsbruck, probed for water sorption; the NPDF was measured by Jue Liu, SNS, Oak Ridge National Laboratory, and Marko Schowalter, Uni Bremen, did the TEM measurements.

Größter Dank gilt meiner Familie und meinen Freunden.
Sie sind es, die mir diese Arbeit erst ermöglichten – mich mit klugem Rat zum Besseren lenkten, mir im Wald voller Bäume die Richtung wiesen, mich mit aufbauenden Worten durch dunkle Täler trugen, mir auch nach Funkstille mit Verständnis antworteten und mir ein steter Quell von Freude sind.

Ich danke Rolf für und bin sehr stolz auf unsere tolle Zusammenarbeit in einer außerordentlich fordernden aber ebenso produktiven wie lehrreichen Projektphase.

Ich danke Malte für die gemeinsame Zeit und Britta, Jörg und Nils für ihre Nähe, Halt und Trost in einer der schwersten Lebensphasen.

Von tiefstem Herzen danke ich meiner Partnerin Andrea, meinen Eltern Sigrun und Wilfried und meinen Brüdern Niklas und Marik. Eure unbedingte Unterstützung über die vielen Jahre ist schwerlich in Worten zu würdigen. Ich schätze mich über alle Maßen glücklich, euch an meiner Seite zu wissen.

Contents

Summary v

1 Introduction 1
- 1.1 Structural hierarchies of tungstates . . . 1
  - 1.1.1 Tungsten trioxide: the non-layered perovskite analogue . . . 1
  - 1.1.2 Aurivillius phases . . . 5
  - 1.1.3 Ruddlesden-Popper phases . . . 16
  - 1.1.4 Related structural motifs . . . 23
- 1.2 Properties of layered tungstates . . . 25
- 1.3 Intention of this research . . . 26

2 Experimental & analytical methods 28
- 2.1 Synthesis . . . 28
  - 2.1.1 Aurivillius-type $Bi_2W_nO_{3n+3}$ . . . 28
  - 2.1.2 Ruddlesden-Popper-type $H_2W_2O_7$ . . . 28
- 2.2 Analytics . . . 29
  - 2.2.1 Diffraction . . . 29
  - 2.2.2 Spectroscopy . . . 32
  - 2.2.3 Thermoanalysis . . . 33
  - 2.2.4 Microscopy & Elemental analysis . . . 34

3 Thermal Behavior of Aurivillius-type Bismuthtungstates 35
- 3.1 Analysis details . . . 35
- 3.2 Diffraction experiments . . . 37
  - 3.2.1 Autocorrelation and Rietveld parameters . . . 37
  - 3.2.2 Atomic positions . . . 39
  - 3.2.3 Derived bond lengths and ellipsoid analysis . . . 41
- 3.3 Raman spectroscopy . . . 47
- 3.4 Thermoanalysis . . . 51
- 3.5 Conclusion . . . 52

4 Synthesis and Structure of Ruddlesden-Popper-type $H_2W_2O_7$ 55
- 4.1 Formation and Morphology . . . 55
- 4.2 Spectroscopic characterization of hydrogen environment . . . 57
- 4.3 Comparison of different structure model candidates . . . 63
  - 4.3.1 Related compounds (RCs) . . . 73
  - 4.3.2 Model in space group $Pna2_1$ . . . 75
  - 4.3.3 Model in space group $P222$ . . . 81

4.3.4 Model in space group $P222_1$ 82
4.3.5 Model in space group $Pnam$ 86
4.3.6 Model in space group $P2_1/n$ 92
4.3.7 Discussion on the Rietveld refinements 97

Appendix **99**

List of Figures **103**

List of Tables **105**

List of Abbreviations **107**

Bibliography **109**

1 Introduction

1.1 Structural hierarchies of tungstates

When introducing the concept of atomic structures and internal arrangement of solids to laymen, the picture of a regular three-dimensional (3D) grid of chemical species is brought up at first. A highly symmetric, perfectly ordered closed packed Si or cubic NaCl crystal usually serves as an example, wherein each main orthogonal spatial direction shows exactly the same arrangement and properties. However, nature offers vast possibilities to assemble atoms and to form solids.

This thesis deals with tungstate systems known for their structural diversity and for showing atomic arrangements which are of low dimensionality, low symmetry and/or low order. Starting with the concepts of well-ordered systems helps to understand those deviating from the perfect, simple state. Accordingly, we approach the family of two-dimensional (2D) layered tungstates via the more regular 3D tungsten trioxide. After that, the peculiarities of the layered bismuth tungstates of the Aurivillius family are introduced, followed by the closely related Ruddlesden-Popper structures and the respective hydrotungstates. Finally, a short overview over further related structures such as the tungsten bronzes is given.

Figure 1.1 gives a schematic overview over different structures and structural motifs covered in this thesis.

1.1.1 Tungsten trioxide: the non-layered perovskite analogue

In the structure of the simple tungsten trioxide, tungsten is sixfold coordinated with oxygen in an octahedral fashion (Figure 1.2c). Adjacent octahedra share their oxygen atoms to form a three-dimensional network. At ambient conditions, the WO_3 structure exhibits the thermodynamically stable γ-modification with monoclinic space group (SG) $P21/n$ (No. 14) and lattice parameters $a = 730.084(7)$ pm, $b = 753.889(7)$ pm, $c = 768.962(8)$ pm and $\beta = 90.892(1)°$. [1] The topology of the corner-sharing octahedral network is similar to those of two related structure types: the ReO_3-type and the perovskite-type.

The binary compound rhenium trioxide (ReO_3) crystallizes in a highly symmetric primitive cubic unit cell with SG $Pm\bar{3}m$ (No. 221). [2, 3] The rhenium and oxygen atoms forming the centers and corners of platonic octahedra (Figure 1.2a). This structure motif is the ideal of the corner-sharing octahedra building scheme and represents the high-symmetric and non-layered parental structure type for all crystal structures covered in this thesis.

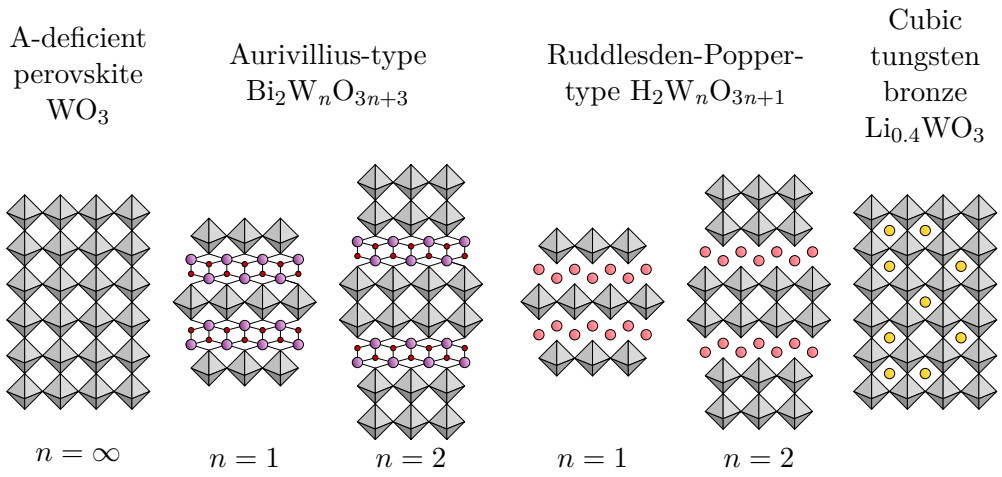

Figure 1.1: Schematics of structure types covered in this thesis or related to those.

Structure of the perovskite type exhibit an atom in the center of the void spanned by eight interconnected octahedra (Figure 1.2b). The chemical composition of these perovskites is generally denoted as ABX_3, with A as the void occupying species and B and X forming the octahedra center and corners, respectively. The crystal chemistry of perovskites is vast with numerous combinations of elements reported. [4] The structural arrangement of combinations of A, B and X with different sized species can be estimated from geometric considerations via the famous Goldschmidt relation

$$t = \frac{r_A + r_B}{\sqrt{2}(r_A + r_X)}$$

based on their respective ionic radii r_i. [5] The Goldschmidt tolerance factor t serves as a measure to estimate the stability and symmetry of the respective combinations. Perovskite oxides, i.e. X is O^{2-}, exist within their stability range of t from 0.71 to $\approx$1.1 with $t = 1$ representing the ideal cubic symmetry. For an extensive overview of perovskites, related structures and the resulting properties the reader is referred to the recent book of Tilley which gives an ecclectic introduction into the manifoldness of this field. [6]

Due to their close correlation, the WO_3 structure is frequently described as a distorted ReO_3-type, where the distortion from the highly symmetric arrangement is based on two mechanisms. Both distortive effects are also relevant factors for the structures of the layered tungstates covered in this thesis as they apply for perovskites in general.

The first mechanism concerns the local coordination shell of the tungsten atom, which deviates from that of a platonic octahedron. The deviation is caused by an off-centering of the tungsten atom in direction of mainly one of the edges and slightly one adjacent face as well as a slight deformation of the oxygen ligand sphere. [1] This lowering of local symmetry can be mostly attributed to the pseudo Jahn-Teller effect

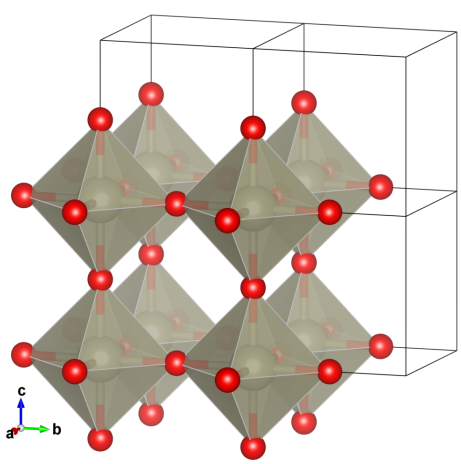

(a) The highly symmetric, primitive cubic crystal structure of ReO_3 (SG $Pm\bar{3}m$), consisting of corner-sharing platonic octahedra.

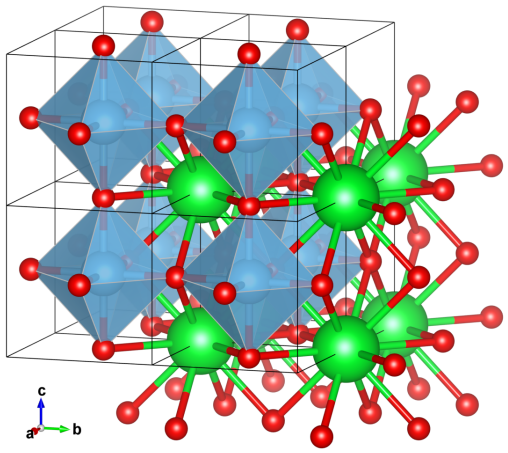

(b) Ideal cubic ABX_3 perovskite structure of $SrTiO_3$ (SG $Pm\bar{3}m$), showing the additional 12-fold coordinated Sr atom in between the corner-sharing TiO_6 octahedra.

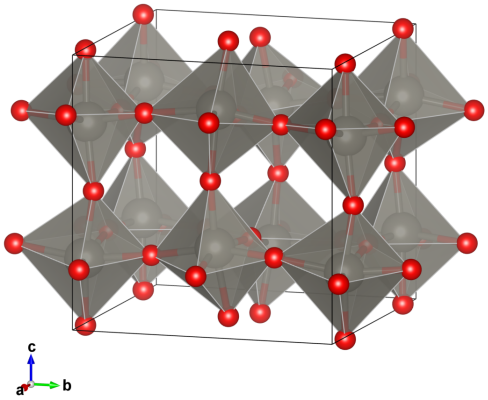

(c) Room-temperature structure of the γ-WO_3 (SG $P2_1/n$), also described as distorted ReO_3-type or A-deficient perovskite-type.

Figure 1.2: Three-dimensional networks of octahedra in the perovskite and perovskite-like structure types.

(PJTE), also called second-order Jahn-Teller effect (SOJTE), with additional effects playing a supportive role. Cations in d^0-configuration, like W^{6+}, are prone to this type of distortion. [7]

One condition for distortion to occur due to PJTE is a sufficiently small gap between the highest occupied molecular orbital (HOMO) and lowest unoccupied molecular orbital (LUMO). In the bulk WO_3 case, it is the valence-conduction band gap between the filled p-orbitals of the ligands and empty d-orbitals of the central atom. If the electronic states are sufficiently close to each other and can engage in a vibronic coupling, they fulfill the prerequisite of pseudo-degeneracy. An additional symmetry breaking, e.g. out-off-center distortion, can lift this pseudo-degeneracy, however, this distortion only occurs if it is ultimately more beneficial towards a lower final total energy. [8] For the lower final energy the effect needs to outweigh the usually counteracting intrinsic structural energy in highly symmetric, electronically non-degenerate systems, e.g. through a covalency gain due to enhanced orbital overlap. [8] This is in contrast to the regular Jahn-Teller effect (JTE), which is mainly electrostatically driven and where an actual degeneracy in the initial state of a susceptible electronic configuration is present. Its subsequent lifting by symmetry breaking towards a non-degenerate final state always leads to a lowering in total energy of the system. [9]

The second mechanism is the deformation of the corner-hinged octahedral network via compliant tilting/rotation of the octahedral axes away from the unit cell axes. It is also one of the supportive effects determining the direction of the above-mentioned off-centering distortion. Octahedral tilting in perovskite-like structures is usually described in the Glazer notation comprised of three letters each with a superscript. [10–12] Each pair describes the relative magnitude (letter) and direction/phase of rotation (superscript) of neighboring units with respect to the three principal axes of a cubic aristotype, i.e. along the connections of the corner-sharing network. The aristotypic ReO_3 belongs to the "zero tilt" group $a^0a^0a^0$, with the triple a indicating the same magnitude of tilting for all directions, which actually is zero as indicated by the 0 superscript. Indeed, in the high symmetry cubic rhenate structure there is no tilting present in any direction.

The γ-modification of WO_3 in SG $P2_1/n$, that is thermodynamically stable at ambient conditions, belongs to the "three tilt" group $a^-b^+c^-$ (or equivalently $a^+b^-c^-$, depending on cell choice). It exhibits different magnitudes of octahedral rotation with respect to the cell axes (indicated by different letters), an in-phase rotation of adjacent units about one axis (positive superscript, here the **b**-axis) and an anti-phase behavior in the two other principal directions (negative superscript). [13, 14] This tilting pattern is attributed to the absence of d-electrons in W^{6+}, contrary to the rhenate case, where an additional electron is available due to the d^1 configuration of Re^{6+}. That electron fills the anti-bonding π^*-orbitals driving the system towards orthogonality and stabilizes the cubic symmetry of the rhenate structure.

Due to the structural flexibility induced by these distortion mechanisms, the WO_3 structure shows a pronounced polymorphism in the temperature range 0 K to 1200 K. [15] At least two low-temperature (LT) and four high-temperature (HT)

phase transitions (PTs) with changes of space group symmetries and even further LT PTs based on dielectric anomalies have been reported. [15–17] Each of the different polymorphs is characterized by different degrees of octahedral tilting and out-off-center distortion. However, even with the usual tendency of structures adopting higher symmetries with elevated temperatures, tungsten trioxide does not seem to adopt a ReO_3-like cubic high-temperature phase. [18] Interestingly though, a cubic WO_3 modification has been reported in a metastable form, being synthetically accessible only by subtle thermal decomposition of layered tungstate precursors. [19, 20] As can be expected from symmetry considerations, the reported cubic lattice parameter of ∼373 pm corresponds to about half of the γ-modification's lattice parameters or roughly twice the typical WO-bond distance, i.e. the distance between opposite octahedral corners.

Another consequence of the WO_3 lattice's flexibility is the possibility for accommodation of differently sized chemical species on its vacant A site, which will be addressed later in subsection 1.1.4. As such, the classification as an A-deficient perovskite is preferred by the author from a crystal-chemical standpoint instead of the symmetry focused referral to the tungsten trioxide as being ReO_3-like. Accordingly, throughout this thesis WO_3 and the related layered tungstates discussed herein will be denoted as being "perovskitic".

On a side note, the structure of γ-WO_3 is actually one of the first examples that were confirmed with the Rietveld refinement analysis applied to data from neutron powder diffraction. [21, 22] Both methods were also used extensively over the course of the project to characterize the related layered tungstate compounds.

1.1.2 Aurivillius phases

With the concept of the perovskite as a 3D network of octahedra in mind, we approach the related 2D layered tungstates by introducing the Aurivillius-type compounds.

In 1949 the first of a series of publications by Aurivillius reported on the eponymous family of compounds with the general formula of $(Bi_2O_2)(A_{n-1}B_nO_{3n+1})$. [23–25] Their building scheme consist of n corner-sharing octahedral layers stacked on top of each other forming the perovskitic domains $(A_{n-1}B_nO_{3n+1})^{2-}$ which are separated by fluorite-like $(Bi_2O_2)^{2+}$ layers. Some archetypal compounds of this class are shown in Figure 1.3 as examples for different layer thicknesses n.

Members of the Aurivillius family usually show a (pseudo-)tetragonal or orthorhombic crystal symmetry at ambient conditions. [26] They tend to adapt space groups $A2_1am$ (non-standard setting of $Cmc2_1$, No. 36) for even and $B2eb$ (non-standard setting of $Aea2$, No. 41 [cited with former nomenclature $B2cb$ in reference]) for odd values of n, both related to a (hypothetical) tetragonal aristotype in $I4/mmm$ (No. 139). [27]

The non-standard space group settings are related to the stacking direction usually being assigned as the crystallographic c-axis with the thickness of the perovskite slab dictating the c lattice parameter. Individual neighboring perovskite layers are

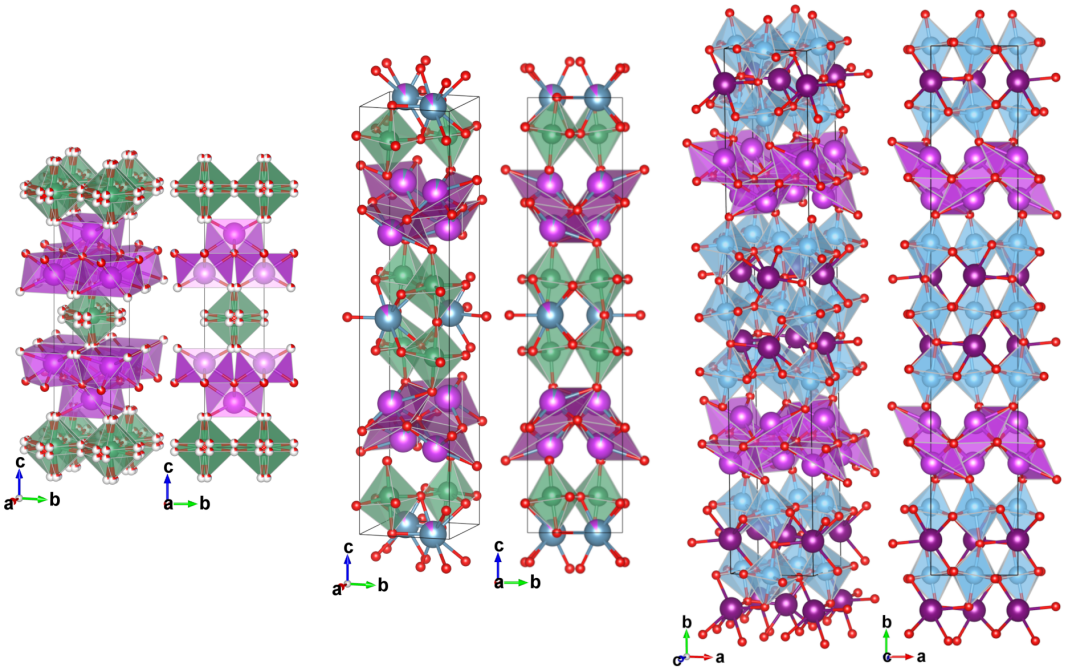

Figure 1.3: Examples of Aurivillius-type structures with $n = 1$ to 3 showing the typical alternating sequence of perovskite-type layers intergrown with fluorite-like BiO-layers. (left) $n = 1$ Bi_2NbO_5F (ICSD152994, $I4/mmm$, No. 139), an oxyfluoride with ligand site disorder and average aristotype symmetry. Note also the fairly regular Bi coordination. (center) $n = 2$ $Bi_2CaNb_2O_9$(ICSD36108, $A2_1am$, No. 36), note the common partial mixing of Bi on the A-site and vice versa, related to Bi as the A-site cation in (right) $n = 3$ $Bi_4Ti_3O_{12}$ (ICSD152994, $Aba2$, No. 41).

shifted against each other by a shift vector of $\mathbf{s} = (\mathbf{a} + \mathbf{b})/2$, i.e. diagonally by half the lattice vectors in the ab-plane.

The range of n starts from $n = 1$ for a single perovskitic layer and can reach up to $n = 5$ for the higher-order Aurivillius phases, while the respective pure perovskite ultimately can be thought of as the $n = \infty$ end member of the series. The perovskite-like slab generally shares the features of the perovskite system, however, its chemical variability is slightly reduced in the Aurivillius phases. Here, the range for the Goldschmidt tolerance factor t is negatively correlated to the layer thickness n and furthermore limited to combinations which form interfaces spatially commensurate to the bismuth oxide layer. Otherwise, the internal strain would get too high preventing the formation of stable structures. [27, 28]

The bismuth-oxygen coordination in the fluorite-like interlayer is sometimes described as an asymmetrically distorted antiprism. One hemisphere can be described as a fairly regular square pyramid with four of the central oxygen atoms in the fluorite layer as the basal plane and Bi forming the apex. The other hemisphere

towards the perovskite layer does not adhere to a strictly regular pyramidal bonding scheme, thus challenging the idea of an antiprism. The notion of an antiprism stems from a hypothetical bonding scheme with the apical oxygen atoms of the four closest neighbor perovskite octahedra. Depending strongly on the nature of the perovskite block and its octahedral rotation pattern the distance distribution between Bi and the octahedra apices can become severely disparate. Another factor influencing the geometry is the stereochemical activity of the bismuth 6*s* lone-pair. [29] The presence of a lone-pair is not a strict prerequisite as recent publications report on partial substitution of interlayer bismuth with iso-, aliovalent and also non-lone-pair cations, e.g. with Pb^{2+}, Ca^{2+} or La^{3+}. [4, p. 45] This interlayer flexibility partially lifts above-mentioned limitations of the structural stability with regard to chemical compositions of the perovskite block. [30] As such, the bismuth oxide interlayer has somewhat lost in significance as the family defining feature, which now could more generally be thought of as an intergrowth of fluorite- and perovskite-type.

In addition to the chemical complexity, another dimension is introduced by the system's ability to form intergrowths of different perovskite slabs A and B with distinct sizes ($n_A \neq n_B$) and/or composition. [31]

The $n = 1$ bismuth tungstate Bi_2WO_6

One of the simplest representatives of the Aurivillius group of compounds is the $n = 1$ member γ-Bi_2WO_6, also known under the mineral name russellite. The crystal structure consists of single layers of corner-sharing WO_6-octahedra separated by the Aurivillius-typical bismuth oxide layers, depicted in Figure 1.4. The symmetry of this structure has been the subject of considerable debate. Amongst other possibilities it has been described in the Aurivillius-typical space group $B2eb$ by Wolfe, Newnahm and Kay (given as $B2cb$). [32] However, later determination by Knight assigned the orthorhombic space group $Pca2_1$ (No. 29). [33, 34] To stay in the usual scheme in Aurivillius phases of assigning the stacking direction to the *c*-axis and the polar axis to the *a*-axis, the non-standard setting $P2_1ab$ is used within this thesis. With orthogonal lattice parameters of $a = 545.84(2)$ pm, $b = 543.73(2)$ pm and $c = 1643.02(5)$ pm the unit cell is relatively close to be tetragonal. This relates to the aforementioned hypothetical aristotype in $I4/mmm$ with a tetragonal lattice parameter $a_T \approx (a_O + b_O)/(2\sqrt{2}) = 385.22$ pm. This is comparable to the cubic tungsten trioxide with $a_C \approx 373$ pm and illustrates the close relationship of Bi_2WO_6 and WO_3 as the $n = 1$ and $n = \infty$ members of the Aurivillius family, respectively.

As in the non-layered WO_3, the perovskite-like tungsten oxide layer exhibits a distorted WO_6 octahedron. In contrast to WO_3, the presence of the bismuth interlayer and the stereochemical activity of its lone electron pair provides an additional mechanism contributing to the distortion in the system. The bismuth oxide layer externally acts on inter- and to some extent also the intra-octahedral distortion of the WO-layer, which in the pure tungstate case in subsection 1.1.1 was referred to as a supportive effect. Halasyamani refers to these contributions as primary and, in this case of a heteroatomic influence, secondary distortive effects, respectively. [35]

The WO_6 octahedra in Bi_2WO_6 show an off-centering of the tungsten atom, attributed to the d^0-related SOJTE of W^{6+} as well as pronounced octahedral tilting influenced by the BiO-layer. Notably, Halasyamani points out that the direction of this off-centering is governed by the supportive or secondary distortive effect of the bismuth lone-pair. [35] In this compound, the WO bond-lengths, the related off-centering of the tungsten atom and deviations of the octahedral ligand sphere from a platonic body are comparable to those of tungsten trioxide. [36]

The tilting of the WO_6-octahedra can be described in terms of the Glazer notation, however, due to the layered nature of the structure it is not strictly applicable. The notation is with respect to the tetragonal aristotype in $I4/mmm$, whose principal axes run through the corner connection points, e.g. along the [110], [1$\bar{1}$0] and [001] viewing directions of the $P2_1ab$ structure. Within the plane of the corner-sharing layer, the octahedra are rotated anti-phase by the same amount in both directions. [37] There are no directly connected octahedra in **c**-direction, however, considering the in-phase rotation of octahedra in neighboring sheets the classification is $a^-a^-c^+$.

As mentioned above, the anion hemisphere around bismuth towards the perovskite block is distorted and especially in Bi_2WO_6 differs strongly from a hypothetical regular antiprism. The coordination around both Bi positions are shown in Figure 1.5 depicting the distorted antiprismatic BiO_8 polyhedra and respective distances. Additionally, the distance to the respective closest oxygen atom O4/O5 in the corner-sharing WO network is given for both Bi positions. Notably, the two long distanced oxygen atoms of both antiprisms are significantly farther away than O4/O5 in the perovskite layer. Even O4/O5 are outside of what would be considered the first coordination sphere. [38]

Knight attributed the asymmetry of the antiprismatic Bi-O environments, and thus also the related octahedral tilting in the perovskite layer, to electrostatic repulsion between the Bi lone electron pairs and oxygen anions. [33] The distorted antiprism pinacoids with the respective two short and two long Bi-O distances would thus be a result of a repulsive interaction in the picture of the valence structure electron pair repulsion (VSEPR) model. [38] This interpretation was doubted recently by Okudera et al. [36] The maxima of residual electron density found in the structure are interpretable as the lone pairs of the Bi ions. Both maxima are situated almost normal to the layer plane above the Bi atom and in that point along c towards the perovskite blocks and not towards the long distanced oxygen atoms. [36] The distances from the Bi^{3+} cation to maxima of the electron density is less than $\sim$100 pm (gauged from their positions relative to the oxygen layers in [36, Fig. 3]), which is in line with the reported distances of 98 pm [39] and 65.9 pm [40].

The results of Stoltzfus et al. also show that the 6s lone-pair of Bi^{3+} is not as localized as found at other lone-pair active ions due to relativistic contraction. [41] Furthermore, the report illustrates that the lone-pair stereoactivity in bismuth and the respective distortion is also a result of the SOJTE. The interaction of the lone Bi 6s with O 2p leads to a pseudo-degenerate state, that is again lifted by further mixing with vacant p-orbitals of bismuth, similar as for the distortion in WO_3 de-

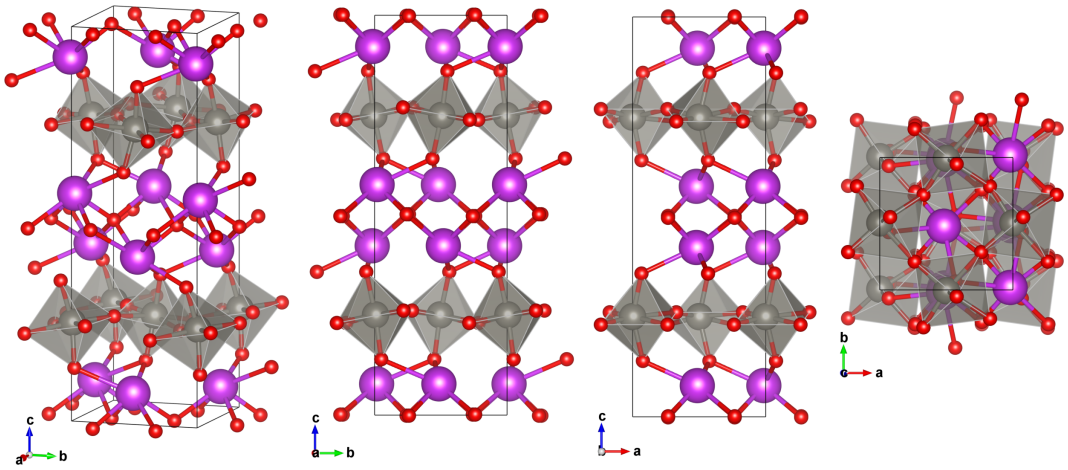

Figure 1.4: Structure of the $n = 1$ member γ-Bi_2WO_6 ($P2_1ab$, No. 29), also called russellite

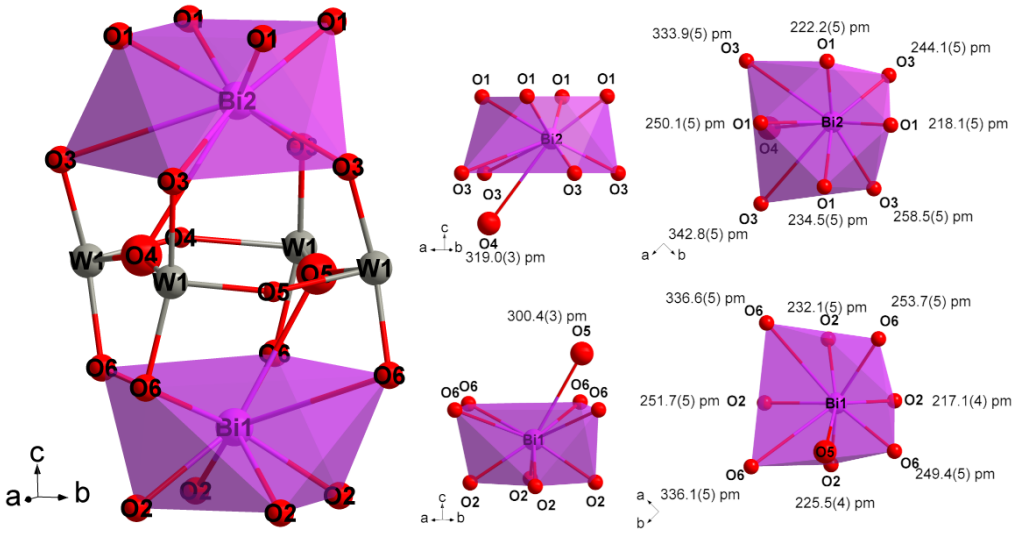

Figure 1.5: Severely distorted antiprismatic coordination sphere around the two Bi positions in Bi_2WO_6. The distances to bridging oxygens in the WO-layer show comparable lengths.

scribed above. Most notably, Stoltzfus et al. argue that the energies of systems with distorted and symmetric Bi environments are energetically competitive. [41] External influences are hence important for the occurrence of a SOJTE and direction of the distortions, as has been described above. Subtle interactions, e.g. with anions at farther distance or higher order coordination shells, can play minor but significant roles in the overall bonding situation, as has been described for other lone-pair stereoactive elements. [38]

The role of the bismuth bonding environment was also studied theoretically by *ab initio* calculations. [42] The study revealed the strong influence of the bonds within the fluorite-type BiO-layer on the stabilization of the ferroelectric structure and the interaction of Bi 6*s* with O 2*p* states with regard to the lone pair activity. [42]

The uneven bonding situation and affiliated tilting thus can not be explained by the lone pair alone in terms of simple electrostatic repulsion. However, it is part of a cooperative distortion due to the SOJTE and π-bonding in conjunction with the distortive forces in the WO-layer. [35]

High-energy X-ray total scattering and pair distribution function (PDF) analysis of Bi_2WO_6 revealed a deviation from the previously reported average structure model in the BiO-environment. [43] The deviation was attributed to a slight shifting of bismuth atoms in stacking direction and a resulting difference in the coherence length between the BiO- and WO- layers. The thermal behavior of this shifting is closely coupled to the Bi atoms atomic displacement parameter (ADP). The disorder vanishes at the phase transition at approx. 993 K, where both bismuth positions of the room-temperature (RT) phase become crystallographically indistinct. [43]

In general, the temperature-dependent polymorphism of Bi_2WO_6 is quite rich. Several phase transitions have been reported with various degrees of structural changes. As the distortion in the tungsten and bismuth polyhedra introduces polarity even minute structural changes have major impact on properties such as spin ordering, i.e. prevalent ferroelectricity.

In the low temperature region, a phase transition exists below 200 K indicated by appearance of additional shoulders on some Bragg reflections at lower temperatures. [44] Rietveld refinement of the room-temperature structure in $P2_1ab$ to data from those measurements are less satisfactorial, albeit changes in the average structure could not be extracted unambiguously by the authors. [44] In their respective PDF analysis of the local structure, however, a peak splitting in the region of BiO-WO-interlayer correlations was identified and attributed to a shifting of bismuth atoms. [44]

Displacement of Bi along the stacking direction also causes a phase transition at 288 K indicated by an anomalous thermal behavior of reflections at about $Q = 80.0\,\mathrm{nm}^{-1}$ and drastic changes in permittivity. [45] However, the average structure and symmetry was not reported to be significantly affected.

The γ-Bi_2WO_6 phase is stable up to the intermediate temperature region at about 933 K where a subtle phase transition exists as detected by differential thermal analysis (DTA)[46], X-ray diffraction (XRD)[47], neutron powder diffraction (NPD)[34], differential scanning calorimetry (DSC) and permittivity measurements [47, 48]. It

was identified to be displacive and of ferroelectric-ferroelectric type. The higher temperature phase is also of orthorhombic symmetry, however, in space group $B2eb$ (No. 41), which is actually typical for odd-n Aurivillius-type compounds. [49] The symmetry changes due to a gradual loss of the octahedral rotation about the c-axis with increasing temperature. This as resulting in the checkerbox arrangement where only the tilt about the a-axis remains, as can be seen in Figure 1.6.

With further increasing temperature the a-axis tilt also reduces, however, does not vanish completely before the next set of two phase transitions in the high-temperature regime. [34] Dielectric measurements showed the first at 1203 K where a change from ferro- to paraelectric type occurs with a predicted higher temperature symmetry of $Fmmm$. [48] At only slightly higher temperatures, i.e. 1233 K, another, more drastic phase transition takes place. [46, 47] Unusual for high-temperature phases, the symmetry lowers in a reconstructive fashion from orthorhombic $B2eb$ or $Fmmm$ to monoclinic $A2/m$ (non-standard setting of $C2/m$, No. 12, again to conform with the stacking direction in c). Theoretical calculations have shown the hypothetical aristotypic tetragonal $I4/mmm$ polymorph to be significantly higher in energy and thus unfavorable compared to the monoclinic structure. [37] Unique amongst the Aurivillius and other related phases, during the phase transition the 2D corner-sharing architecture of the WO-sheet disbands. Instead, quasi-one-dimensional ribbons of edge-sharing WO-octahedra dimers linked by their apices form as visualized in Figure 1.7. [34] While polarity still exists locally due to off-centering of the metal atoms within their respective oxygen environments, it is mutually canceled out and the structure is net paraelectric. The ribbon-like structural feature is also present in the $Bi_{2-x}Ln_xWO_6 (\sim 0.3 < x <\sim 1.3, \mathrm{Ln} =$ most of the lanthanides) group of compounds at ambient conditions. [50] Other interesting features are the heating/cooling rate dependence of the phase transition onset and the large hysteresis of Curie temperature T_c of about 100 K between heating and cooling. [48, 51]

The sequence of reported temperature-induced phase transitions (adapted from [52]) can be described as follows:

γ', HT | >1233 K | $A2/m$ (No. 12) | $Z = 4$ | paraelectric | -
γ'' | 1233 K to 1203 K | $Fmmm$ (No. 69) | $Z = 4$ | paraelectric | symmetry only predicted [48]
γ''', IT | 1203 K to 933 K | $B2eb$ (No. 41) | $Z = 4$ | ferroelectric | -
γ, LT | 933 K to 288 K | $P2_1ab$ (No. 29) | $Z = 4$ | ferroelectric | -
γ'''' | 288 K to ~200 K | $P2_1ab$ (No. 29) | $Z = 4$ | ferroelectric | identified by dielectric and high-Q intensity anomalies [45]
γ''''' | < ~200 K | $P2_1ab$ (No. 29) | $Z = 4$ | ferroelectric | symmetry tentative, identified by reflection splitting and local structure analysis [44]

It has to be noted that this bismuth tungstate is isomorphic to $BiMoO_6$, also known as koechlinite. In fact, the structure of the molybdenum compound served as the starting model for structure refinement by Knight. [49] It exhibits the same

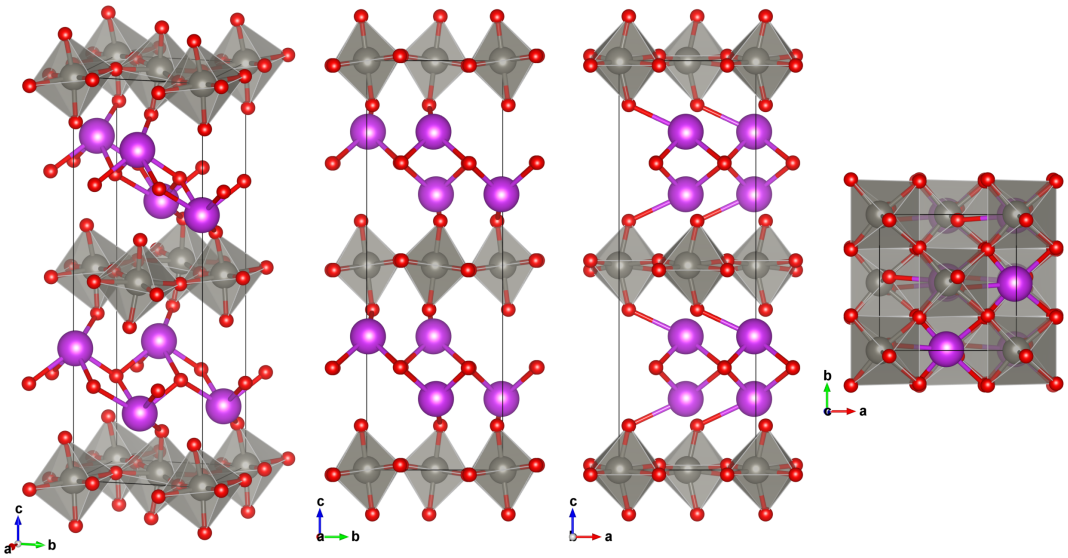

Figure 1.6: Structure of γ'''- or IT-phase of Bi_2WO_6 ($B2eb$, No. 41) stable within temperature range of 1203 K to 933 K showing the loss of octahedral rotation around the c-axis.

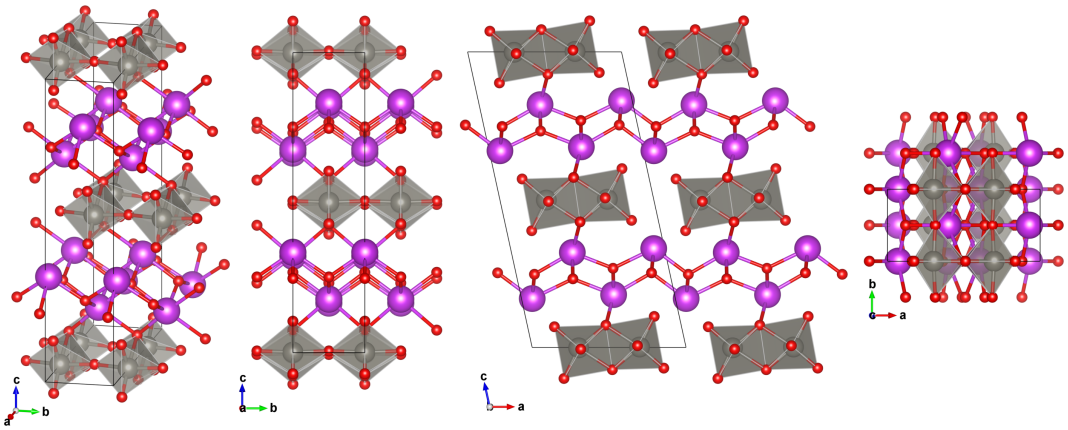

Figure 1.7: Structure of γ'- or HT-phase of Bi_2WO_6 ($A2/m$, No. 12) stable above 1233 K, note the perovskite-like arrangement broken into dimeric chains.

octahedral tilting and a comparable temperature-dependent behavior, however, with different phase transition temperatures. [46–48] Furthermore, solid solution between these compounds have been reported. [53, 54]

The $n = 2$ bismuth tungstate $Bi_2W_2O_9$

Extension of the perovskite block with a second layer of tungsten oxide octahedra results in $Bi_2W_2O_9$, the $n = 2$ member of the Aurivillius-type bismuth tungstate (see Figure 1.8). An important feature of this compound is the empty void spanned by four adjacent octahedra within the perovskite-like WO-block. Similar to WO_3 being referred to as an A-site deficient perovskite, $Bi_2W_2O_9$ represents an A-site deficient analog of the Aurivillius phases. In fact, it is the only known structure of this type.

The first structural description of $Bi_2W_2O_9$ as a layered compound and member of the Aurivillius family was reported by Watanabe and Goto. [55, 56] Based on their powder XRD and electron microscopy results they assigned the space group $Pna2_1$ (No. 33) which was confirmed only after 20 years later by a structure determination from single crystal XRD by [57] However, recently over the course of this project two reports were published independently that redetermined the structure to actually be of higher symmetry in centrosymmetric spacegroup $Pnab$ (No. 60, non-standard setting of $Pbcn$). [52, 58] The lattice parameters were determined to be $a = 543.349(7)$ pm, $b = 541.326(7)$ pm and $c = 2369.02(3)$ pm. The a and b lattice parameter, again close to each other with a hypothetical tetragonal lattice parameter $a_T \approx 383.491$ pm, are slightly smaller than those of the Bi_2WO_6. The c lattice parameter differs by $726.00(6)$ pm between the $n = 1$ to $n = 2$ member. This difference is about two times the size of a WO-octahedron or roughly two times a_T, illustrating the concept of the lattice parameters being direct functions of the perovskite block size.

The centrosymmetric nature of the structure and apparent absence of ferroelectricity is in strong contrast to the $n = 1$ compound Bi_2WO_6 and other Aurivillius phases, where this property is frequently encountered. One of the main reasons for ferroelectricity in the $n = 1$ bismuth tungstate, i.e. polar WO_6-polyhedra due to off-centering of the tungsten atom, is also present in the $n = 2$ member with comparable magnitude. However, the direction of the off-centering between the two individual octahedral layers per perovskite block is antiparallel thus cancelling each other out and resulting in no net polarity. [58] The WO bond lengths in $Bi_2W_2O_9$ are comparable to Bi_2WO_6 and WO_3. The tilting pattern in $Bi_2W_2O_9$ is slightly different to both related compounds, as no in-phase tilting can be found in any direction. The in-plane tilting, again with respect to the Aurivillius aristotype in $I4/mmm$, is anti-phase in both directions and thus similar to the $n = 1$ compound. The two stacked octahedra per sheet, however, are also rotated in an anti-phase manner in **c**-direction, hence, the tilting is described as $a^-a^-c^-$.

DFT calculations show the off-centering, i.e. polar distortion modes, is the main energy gain factor for structure stabilization in $Bi_2W_2O_9$ as well as for WO_3, how-

ever, for Bi_2WO_6 the energy gain of tilting is comparable. [58] This is supported by pressure- and temperature-dependent Raman measurements indicating a higher similarity of BiW_2O_9 and WO_3 with respect to the WO environment and its phonon modes. [59, 60] This illustrates the increased rigidity and "3D character" of the extended perovskite sheet. [52]

The bismuth coordination closely resembles that of Bi_2WO_6, also forming a highly anisotropic square antiprisma with on one side a fairly regular pinacoid as part of the BiO-layer and on the other side an irregular pinacoid towards the perovskite layer, as previously described. Also, the distance to one oxygen atom of the WO-network, i.e. O4, is shorter than to two of the latter pinacoid's oxygen atoms, analogous to the $n = 1$ structure(see Figure 1.9).

Although the role of the bismuth lone pair has not been studied in detail for $Bi_2W_2O_9$, it is reasonable to assume that the same underlying principles working in Bi_2WO_6 are also in effect in this structure. Theoretically calculated distances of the lone pair to the Bi^{3+} cation by Pirovano et al. suggest a slightly reduced lone pair of separation of only 51.6 pm (65.9 pm in Bi_2WO_6). [40] Unfortunately, no information about the localization of residual electron densities were reported from the single-crystal (SC)-XRD experiments in [52].

The thermal behavior in $Bi_2W_2O_9$ exhibits no known drastic phase transition related to the average symmetry, however, the compound has also been less extensively studied than $n = 1$ member. In general, for the low temperature region no structural changes have been reported and only minute ones in the high-temperature range. Tian et al. reports on presumed local changes identified by their influence on the materials dielectric permittivity at around 293 K while no features shows in LT-DSC. [52] Furthermore, their data of specific heat and dielectric permittivity give hints to the existence of a phase transition somewhere in the range 883 K to 1013 K, whose origin could not be identified with certainty. [52] The most prominent features in specific heat and dielectric permittivity data speak for the existence of a second-order phase transition at ∼1063 K which is assumed to lead to a high-temperature ferroelectric structure. [52] Peculiarities of some bands in high-temperature Raman measurements in combination with results from pressure-dependent Raman studies support the existence of a second-order phase transition at that temperature leading to a lowering of symmetry. [59, 60] Upon further heating the compound melts incongruently around 1153 K to 1163 K. [55]

The known temperature-dependent phase transitions (adapted from [52]) can be summarized as follows:

- | >1163 K | - | - | incongruent melting
β' | 1163 K to ∼1063 K | orthorhombic | $Z = 4$ | ferroelectric (assumed) | -
β'' | ∼1063 K to ∼1013 K | orthorhombic, probably *Pnab* (No. 60) | $Z = 4$ | paraelectric | first dielectric anomalies occur as low as 883 K
β | ∼1013 K to ∼293 K | *Pnab* (No. 60) | $Z = 4$ | paraelectric | -
β'''' | < ∼293 K | orthorhombic | $Z = 4$ | paraelectric | -

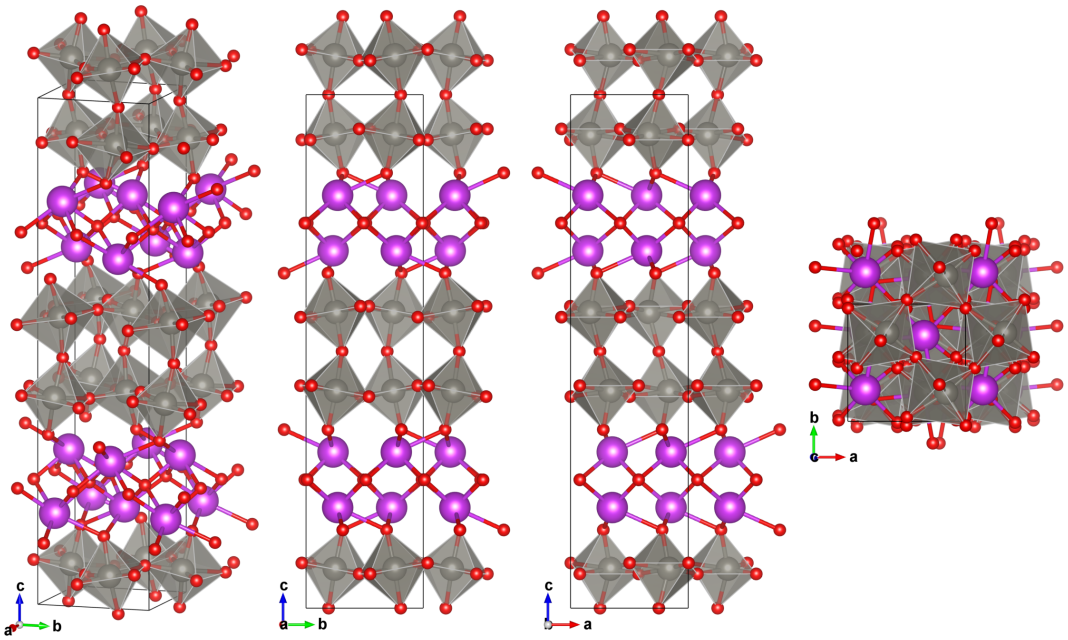

Figure 1.8: Structure of the $n = 2$ member $Bi_2W_2O_9$ (*Pnab*, No. 60). Note the empty void in between the WO_6-octahedra classifying the compound as the only known A-site deficient Aurivillius-phase.

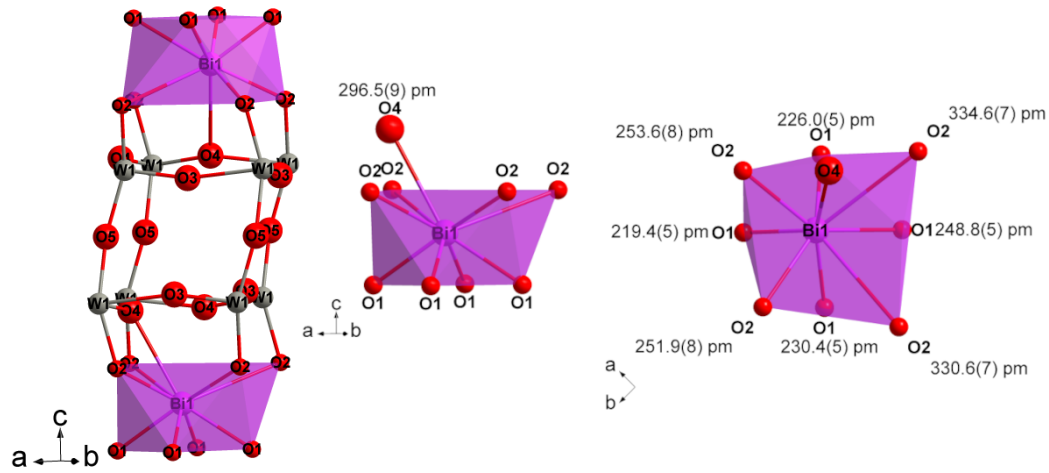

Figure 1.9: Severely distorted antiprismatic coordination sphere around the Bi position in $Bi_2W_2O_9$, with the comparable distance to one of the bridging oxygen atoms in the WO-layer.

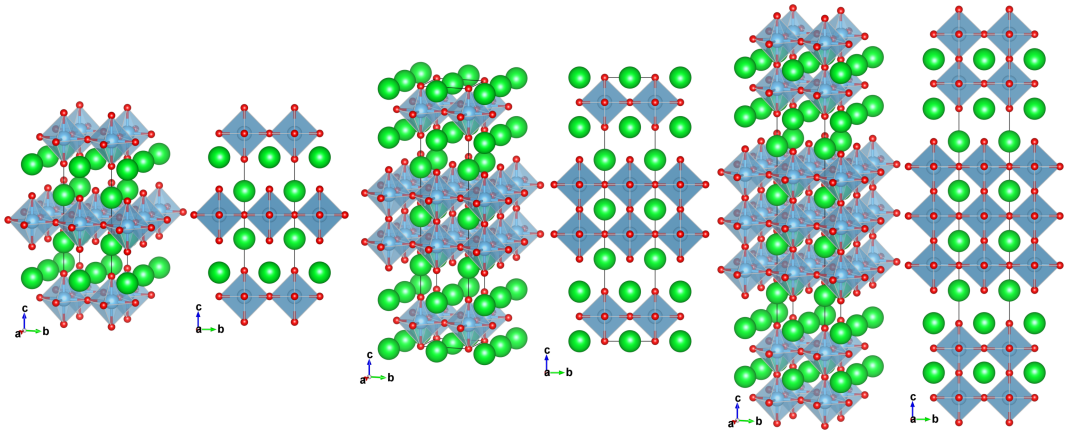

Figure 1.10: Examples of Ruddlesden-Popper-type strontium titanate structures with $n = 1$ to 3 showing a rock-salt-like intergrowth between the perovskite-like layers.

For the sake of completeness, it also has to be noted that a compositional Mo analog $Bi_2Mo_2O_9$ exists as well. In contrast to the $n = 1$ W-Mo homologes it is not isomorphic thus not belonging to the Aurivillius-type family as it rather features Bi_3O_2 chains, Mo tetrahedra and single Bi atoms bound to the latter. [61]

1.1.3 Ruddlesden-Popper phases

Another family of layered perovskites owes its name to the publications by Ruddlesden and Popper from 1957 and 1958. [62, 63] In those the authors described a series of compounds with the general formula $A'_2A_{n-1}B_nX_{3n+1}$.

BX_6 octahedra form the known perovskite-typical corner-sharing framework of variable thickness n. The structure of the $n = 1$ members of the series is also known as K_2NiF_4-type. Members with $n \geq 2$ exhibit the 12-fold coordinated A position in between four adjacent octahedra and the $n = \infty$ member, again, is the classic perovskite structure.

Ruddlesden-Popper (RP) compounds, and especially the oxide members, i.e. X=O, are closely related to and share many features with the Aurivillius phases. They show the same $(\mathbf{a} + \mathbf{b})/2$ shift between adjacent blocks (see Figure 1.10) and similarly a tetragonal aristotype in SG $I4/mmm$ (No. 139).

Instead of the mostly covalent fluorite-like $Bi_2O_2^{2+}$ interlayer known from the Aurivillius phases the RP structures exhibit rock-salt-type A′O layers between the perovskite blocks, which are considered to be mostly ionic.

Stable oxide structures up to $n = 3$ have been synthesized via classic methods, i.e. solid state syntheses[64], however, higher order members seem to be synthetically challenging due to incongruent melting behavior and marginal energy gains towards increasing n. [65, 66] Epitaxial techniques have been applied to produce high-quality structures with higher n, e.g. $Sr_{n+1}Ti_nO_{3n-1}$ with $n = 1$ to $5, 10$. [67]

The chemical variability of the perovskite is retained in the RP phases and tolerance limits based on ionic radii similar to the Goldschmidt factor have been proposed for these phases as well. [65, 68]

The anionic lattice bears possibilities for substitutions, e.g. in oxyhalides, or for substoichiometric compounds, e.g. oxygen deficiencies., which can spark unusual physical phenomena, for instance famously shown in the high-T_c superconducting cuprates. [69]

The rock-salt interlayer introduces another rich dimension of chemical complexity since the A and A′ species are not required to be the same. Both position are occupied mostly by alkali, alkaline earth or rare earth elements, depending on composition and oxidation states within the perovskite part, and introduction of mixed occupation on these sites is a frequently encountered way of influencing the physical properties. Due to the ionic character of the interlayer the A′-species is susceptible to ion-exchange reactions and thus chemically highly variable. [70] Redox-active exchange reactions have been reported in which aliovalent substitution results in a respective altered valences in the perovskite block. The A′ species can also be exchanged with ionic molecules, e.g. with long alkylic tails, enabling organic-inorganic intergrowth and chemical exfoliation of the perovskite sheets. [71] Several RP-phases with various compositions intercalate water in to the interlayer depending on factors like size of A′, oxygen defect density and valence of B cation. [72, and refs. therein]

A plethora of combinations exist with regard to chemical species, defects, further intergrowth patterns and and deviant polyhedral motifs and a comprehensive description is beyond the scope of this thesis. A glimpse of the structural and compositional variability of the Ruddlesden-Popper phases can be found in [65] and [73].

The $n = 1$ hydrotungstate H_2WO_4

Reports on WO-based RP phases are rare. Considering the most frequent oxidation state of +6 for the tungsten atom only monovalent cations are viable options for the interlayer species.

Compositional alkali metal candidates (i.e. A′ = Li, Na, K, Rb and Cs) crystallize in other structure types and all show tetrahedrally coordinated tungsten. [74–77]

However, within the class of hydrotungstates, or "tungstic acids", RP-like structures have been reported.

The structure of the compound H_2WO_4, also known as tungstite or with the formula $WO_3 \cdot H_2O$, is comprised of layers of corner-sharing WO_6 octahedra, similar to the $n = 1$ Aurivillius phase Bi_2WO_6 albeit with two protons in the interlayer instead of ${Bi_2O_2}^{2+}$, and in that represents a $n = 1$ RP phase. [78]

Scheele already synthesized tungstite in 1781 during his analysis of the mineral with formula $CaWO_4$ named "tungsten" (literally meaning "heavy stone") in Swedish. [79] The mineral later was named scheelite in his honors, however, the name stuck as the English and French name for element W. [80]

Similar to what Scheele performed, frequently applied synthesis routes are the

combination of sodium tungstate solutions with strong acids, e.g. HCl or HNO_3, to form the bright yellow compound with a platelet morphology.[81, 82]

Indications of a layered structure for tungstite were already reported in 1959 but a structure determination was not reported until 1984 enabled by the availability of naturally occurring single crystals. [78, 81]

The results by Szymanski and Roberts confirmed the layered building scheme and assigned an orthorhombic symmetry in space group *Pnma* (No. 62). [78] A different setting, i.e. *Pmcn* is used within this thesis to conform with the layer stacking direction along the crystallographic *c*-axis and is depicted in Figure 1.11.

However, a recent study combining different neutron scattering techniques and *ab initio* calculations suggest a structure with lower symmetry in space group $P2_12_12_1$ (No. 19) as shown in Figure 1.12. [83] Lalik et al. argue that the structure model in *Pmcn* is actually unstable, especially with regard to the hydrogen positions. [83] The accuracy of these positions determined from the X-ray single crystal diffraction and data refinement by Szymanski and Roberts can be questioned considering the low scattering contributions of hydrogen. Szymanski and Roberts themselves state that a refinement of the positions were not feasible, instead the positions were deduced based on a difference synthesis. [78]

The reported lattice parameters are $a = 524.90(20)\,\mathrm{pm}$, $b = 513.30(20)\,\mathrm{pm}$, $c = 1071.1(5)\,\mathrm{pm}$ for the *Pmcn* model and $a = 524.86(6)\,\mathrm{pm}$, $b = 514.74(5)\,\mathrm{pm}$, $c = 1065.37(10)\,\mathrm{pm}$ in case of the $P2_12_12_1$ model. While *a* and *b* are comparable there is a slight difference in the *c* lattice parameter. This difference might be based on the different measurement temperatures, i.e RT vs. 1.5 K, or an effect of the sample form, i.e. single crystal vs. powder.

As can be expected from the previously discussed tungstates the perovskite layer exhibits significant distortions. The octahedral rotation of the different proposed models with respect to the $I4/mmm$ aristotype can be described in the Glazer notation as $a^-a^-c^0$ for the model in *Pmcn* and $a^-a^-c^-$ for the model in $P2_12_12_1$. The latter features an additional rotation of the octahedra around the axis parallel to the stacking direction.

The bonds to the equatorial oxygen atoms shared between the adjacent octahedra are comparable to those found in the non-layered WO_3. The apical bonding situation, however, differs strongly from the compounds discussed so far, which is related to the peculiarities of the interlayer.

H_2WO_4 violates the more rigorous definition of Ruddlesden-Popper-type compounds of exhibiting a rock-salt-type interlayer due to what can be considered a cooperative distortion of the proton positions. Firstly, the protons are not located in the typical ninefold oxygen coordination, i.e with about equal distances, known from other RP phases but are closely attached to only the apical/terminal oxygens. Secondly, the protons are not uniformly distributed, i.e. forming a hydroxy-motif on every terminal oxygen, but instead aggregate in pairs forming an aqua-motif. Freedman as well as Szymanski and Roberts point out that the latter property renders the common nomenclature of a "tungstic acid" incorrect and argue for tungstic oxid hydrate or aquatungsten oxide as the valid names, respectively. [78, 81] The term

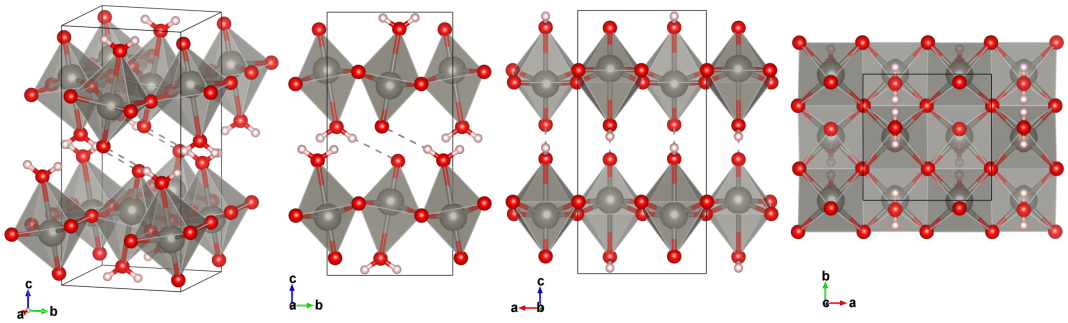

Figure 1.11: Structure of the $n = 1$ RP-like hydrotungstate H_2WO_4 in SG *Pmcn* (No. 62). [78]

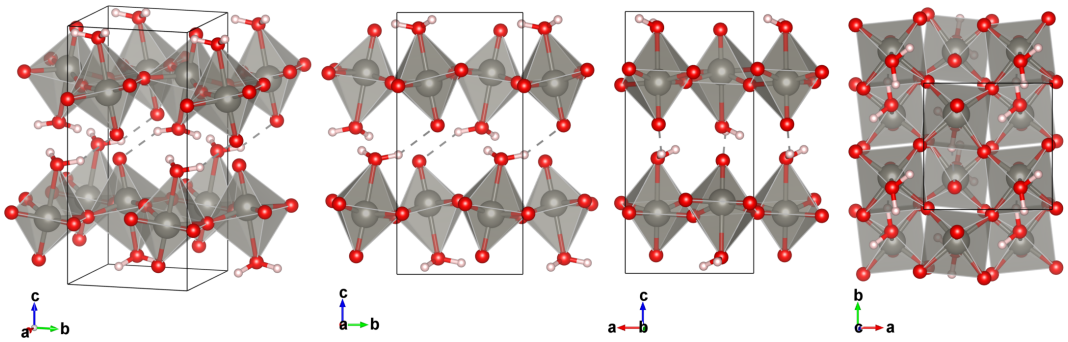

Figure 1.12: Structure of the $n = 1$ RP-like hydrotungstate H_2WO_4 in SG $P2_12_12_1$ (No. 19). [83]

hydrotungstate is used throughout this thesis and the formula H_2WO_4 is preferred over the elsewhere frequently used $WO_3 \cdot H_2O$ in order to highlight the structural aqua-motif as opposed to intercalated water (see below).

The aggregation of protons in the aqua-motif fashion results in a distinctively elongated WO bond to the hydrogen bearing apical oxygen atom, as can be seen from Figure 1.12. This reduced bonding contribution of the aqua-motif is compensated by a stronger attraction of the opposite apical oxygen, i.e. formation of a higher-order or even double bond and a respective short bond length. [84] This feature is referred to as the long-bond-short-bond motif in latter parts of this thesis. Therefore, the off-centering of the W atom is towards an octahedral corner/apex and in that contrasting the shift towards an edge or face prevalent in the the other discussed tungstates. The two different apices carry opposite partial charges, with the aqua-motif and double bonded oxygen being partially positive and negatively charged, respectively Every other octahedron is flipped upside-down compared to the adjacent $WO_5(OH_2)$ octahedra, which can be interpreted as means reduce the electrostatic repulsion and lower the energy of the system. Neighboring perovskite sheets are held together only by weak interactions between their apical functions, like hydrogen bonds and van-der-Waals (vdW) forces. [83] This loose bonding of adjacent layers is in contrast to the significantly stronger ionic and covalent bonds in other RP- and Aurivillius phases, respectively. While the structure model in *Pmcn* suggest linear chains of hydrogen bonds along the crystallographic *b*-axis, the recent study by Lalik et al. employed MD simulations revealing an hydrogen bonding network similar to that of confined water in single walled carbon nanotubes. [78, 83]

An interesting feature of the interlayer is the possibility to host additional water molecules with an according increase in the cell dimensions and distance between the perovskite layers giving $H_2WO_4 \cdot xH_2O$, also known as hydrotungstite. [85] It has been shown that additional water molecules in the interlayer lead to changes in the electrochemical response and an improved proton conduction behavior. [86, 87]

The compound dehydrates upon heating and intercalated water is driven from the interlayer at temperatures over 323 K, even in aqueous media. [81, 85] Subsequently, above ∼423 K the perovskite sheets condensate by removal of the aqua-motif, loss of the layer shifting and linking of the sheets to give the $n = \infty$ 3D connected A-site deficient perovskite structure of WO_3. As previously mentioned, a cubic WO_3 polymorph is reported as a metastable intermediate present in the dehydration process at around ∼573 K. [20]

The isomorphism of the $n = 1$ Aurivillius compounds Bi_2MO_6 (M=Mo, W) is also encountered in the related protonated Ruddlesden-Popper with the hydromolybdate showing the same layered structure and octahedral distortions. Due to the similarity of powder diffraction patterns isomorphism with the respective Mo compounds was hypothesized from early on. [85, 88] Indeed, the layered hydromolybdates again was the first to be described and served as a reference for the structure solution of the tungstate homologue. [78, 89]

The $n = 2$ hydrotungstate $H_2W_2O_7$

Extension of the perovskite sheet by another octahedral layer gives the $n = 2$ compound $H_2W_2O_7$. While this extension is theoretically straightforward, synthesis and analysis of this compounds provides severe complications.

The synthesis of this compound was first described by Schaak and Mallouk in 2002 and shortly thereafter independently by Kudo, Ohkawa et al. [90, 91] It is produced from the Aurivillius-type $Bi_2W_2O_9$ as parent material by selective leaching of the bismuth interlayer with hydrochloric acid. The perovskite layers presumably are only affected little and stay virtually unaltered, based on the transmission electron microscopy (TEM) observation of locally similar layering patterns of educt and product as well as absence of dissolved tungsten species in the reaction fluid. [91] This method and reaction class of *chemie douce* ("soft chemistry") topochemical conversion are frequently employed in the synthesis of metastable compounds due to the low thermal energies involved preventing the formation of only thermodynamically stable products. [92] There is only one other report known to the author claiming a different synthesis route for the double layer hydrotungstate by simple mixing of HCl acidified aqueous sodium tungstate and strontium chloride solutions. [93] However, the as such produced sample was reported to be of extremely low crystallinity and identification as the $n = 2$ compound was based on a single broad reflection. [93]

A particularly interesting feature of this structural concept is the empty void in between four adjacent octahedra. This makes it the rare case of an A-site deficient Ruddlesden-Popper phase. Surprisingly and despite the fact that the general structural concept has been established from early on, no further structural investigations to determine the symmetry and a complete structure model have been found to successfully reach a state beyond "preliminary" before the start of this project. The *chemie douce* synthesis route produces only powders and the problems associated with a structure solution from these are attributed to a low crystallinity and/or small average crystallite sizes as a result of leaching induced disorder. Similarly, development of a structure model for the $n = 1$ hydrotungstate from diffraction data was also not successful until a naturally grown single crystal of sufficient quality was available. [78] Especially in weakly bonded systems like the layered hydrotungstates plausible disorder schemes are numerous, e.g layer shifting, rotations, variations in the interlayer distance, condensation to locally increased n, dislocations, local perforation etc. The longer range, relative turbostratic disorder in a set of layers , e.g. *via* shifting and rotation, pose considerable difficulties for a successful data interpretation, even when in a first order approximation local defects are discarded and a known structure is assumed to be regular laterally in individual layers, e.g. in this case the perovskite-like arrangement. [94] Sophisticated PDF modelling techniques are capable to estimate the magnitude of these disorder schemes but require access to high-quality data, as have been shown for different layered perovskite phases produced by leaching syntheses. [95] The need for PDF analysis for a meaningful description was also identified in this study as the peculiarities of this compound turned out to be intangible by classic powder structure solution procedures.

Only very recently in 2021, during the course of this project, a study by Wang, Sun et al. has been published in which a conclusive structure model for this compound is proposed. [96] The structure model in monoclinic space group $P2_1/n$ (No. 14, unique axis c, cell choice 2) was generated by density-functional theory (DFT) calculations and checked independently against X-ray diffraction data as well as neutron total scattering based PDF data. [96] A representation of the PDF refined model is given in Figure 1.13. However, for the sake of aligning the stacking direction along c, the model was transformed to the space group setting with unique axis b, cell choice 2, which is used throughout this thesis.

The lattice parameters are $a = 514.9(5)$ pm, $b = 524.8(5)$ pm, $c = 1850.0(20)$ pm, $\beta = 89.40(10)°$ for the model refined against neutron PDF data (up to 4 nm real space range). [96] The X-ray powder diffraction (XPD) refined model has lattice parameters of $a = 515(22)$ pm, $b = 524.30(30)$ pm, $c = 1859(15)$ pm, $\beta = 89.4(21)°$ with quite large uncertainties on a, c, and β, possibly due to correlation of these in the refinement. [96]

While being switched by the space group symmetry, the corresponding in-plane lattice parameters a and b of the single and double layer hydrotungstates are almost identical. The c lattice parameter differs by ∼786 pm between the $n = 1$ to $n = 2$ member, depending on the choice of the respective structure models. This difference is significantly larger compared to the value of 726.00(6) pm for the bismuth tungstates, i.e. the individual octahedral layers are thicker in the hydrotungstates. Additionally taking the leaching induced reduction in a and b from bismuth to hydrotungstate into account indicates a relaxation in the perovskite-like arrangement due to the removal of the bismuthyl layer. [91] The fact that this "off-switching" of the bismuthyl layer results in significant changes in the perovskite layer is a fascinating experimental support of and completely in line with the previously discussed strong influence of the BiO-environment (see subsection 1.1.2). The relaxation probably is a strain reduction by octahedral rotation and partial un-tilting. Some degree of tilting remains, however, resulting in a classification of $a^-a^-c^-$ with regard to the hypothetical $I4/mmm$ aristotype, which is ultimately not surprising considering the given tilting in WO_3.

As known from the $n = 1$ member, also in this model the terminal aqua-function leads to the long-bond-short-bond motif. Notably, this motif is further transferred into the second octahedral layer via the shared apical oxygen (see Figure 1.13) An in-depth analysis of the coordination environment of this model refined to our data and a comparison with other structure model candidates is given in section 4.3.

Similar to the $n = 1$ $H_2WO_4 \cdot xH_2O$, the possibility to host additional interlayer water is also given in the $n = 2$ hydrotungstate. [91] Heating to 393 K removes any present interlayer water and subsequently at temperatures above 473 K dehydration to WO_3 takes place. [91]

Finally regarding the similarities to the molybdates, no report on a $n = 2$ hydromolybdate homologue is known to the author as is the case with the $n = 2$ Aurivillius compound.

1.1.4 Related structural motifs

Other forms of tungsten trioxide(-hydrate)

The motif of corner-sharing octahedra can also be found in a hexagonal WO_3, which is synthetically accessible via a hydrated precursor structure. [98] This orthorhombic precursor $WO_3 \cdot \frac{1}{3} H_2O$ is produced by hydrothermally and is characterized by staggered layers of hexagonal rings. [97] Similar to the other hydrotungstates the water molecule is bound in a $WO_5(H_2O)$-octahedra with long-bond-short-bond-motif and points into the empty space of next layers' six-membered ring. It offers an interesting thermal behavior as upon mild heating, i.e. to ∼623 K, it first yields a supermetastable h-WO_3 from in which the staggering is conserved, however, the water molecules reversibly leave the structure leading to some only five-fold coordinated tungsten atoms. [100] Further heating to ∼663 K irreversibly transform the structure to the metastable h-WO_3 by removal of the staggering and alignment of the hexagonal rings to tunnels along [001] (see Figure 1.14), however, not by layer shifting but in a reconstructive fashion involving nucleation and growth of the hexagonal phase. [100, 101] Finally, above ∼773 K the hexagonal structure transforms to the stable monoclinic WO_3. [100]

Closely related are the cubic pyrochlore polymorphs of WO_3 and the corresponding hydrotungstate with composition $WO_3 \cdot 0.5\,H_2O$. [99] They are synthesized directly hydrothermally or via ion exchange of other tungsten pyrochlores $(A_2O)_xW_2O_6$ ($A = Cs, Rb, NH_4$) with nitric acid, however, the latter route is prone to form layered perovskite-like $H_2WO_4 \cdot xH_2O$ side product. [99, 102] The pyrochlore-like structures feature hexagonal rings of corner-sharing WO octahedra albeit these rings do not form staggered layers like above but interconnected tetrahedral cages with a central void, which host the water molecule in case of the hydrotungstate (see Figure 1.14). [102] Heating to above 373 K removes the water from its cage in a zeolite-like fashion, i.e. this is reversible in ambient humidity. [101] Further heating also leads to a transformation to perovskite-like monoclinic WO_3. [99]

Tungsten bronzes

The perovskite-like WO_3 was described as A-site deficient so far, however, it is in fact able to accommodate guest species in those interstitial cuboctahedral voids within the network of WO-polyhedra. These intercalation compounds form the family of the perovskite-type tungsten bronze (PTB), owing the "bronze" part of their name to their drastically changed electro-optic properties reminiscent to those of metals and alloys, i.e. metallic conductivity, coloration and luster. Probably the most prominent member of this family is the sodium tungsten bronze Na_xWO_3, first described by Wöhler in 1824. [103]

The general formula is given by A_xWO_3 and apart from sodium numerous other intercalates, e.g. mostly alkali, transition metals and lanthanides, have been investigated with various amounts x. [104, 105]

Depending on the size and amount of the A species other structure types than

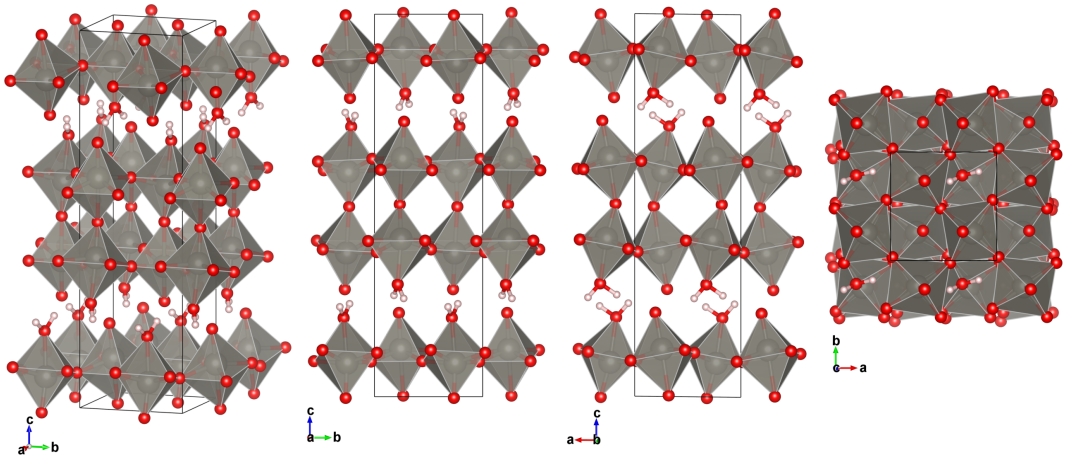

Figure 1.13: Structure of $n = 2$ RP hydrotungstate $H_2W_2O_7$ from neutron PDF refinement up to 4 nm real space range. [96]

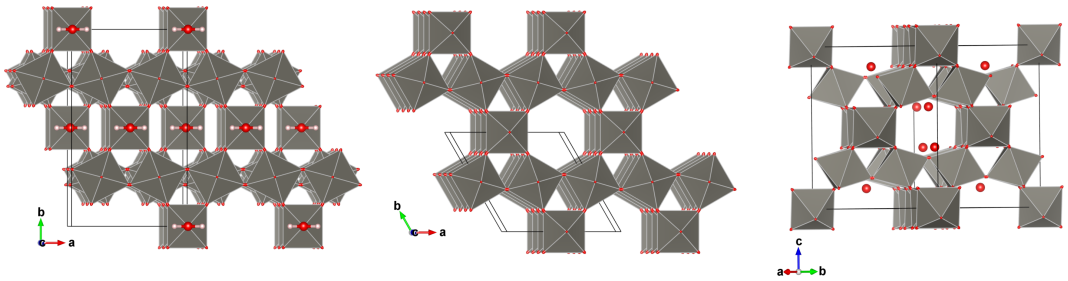

Figure 1.14: Related structural motifs with corner-sharing WO-octahedra. (left) Orthorhombic $WO_3 \cdot \frac{1}{3} H_2O$ (ICSD15514, $Fmm2$, No. 42) characterized by staggered layers of hexagonal rings and $WO_5(H_2O)$-octahedra with the water molecule pointing in the void of the six-ring (positions of the hydrogen atoms were not reported and added manually by the author). [97] (center) h-WO_3 (ICSD32001, $P6/mmm$, No. 191) with aligned hexagonal rings forming tunnels along [001]. [98] (right) Cubic pyrochlore-type $WO_3 \cdot 0.5\,H_2O$ (ICSD202875, $Fd\bar{3}m$, No. 227) featuring water filled interconnected tetrahedral cages formed by hexagonal rings (hydrogen positions not reported). [99]

PTB are known to form, for instance, the hexagonal tungsten bronze (HTB) family is based on the hexagonal tungsten trioxide as the host and mixtures of their respective structural motifs also known, i.e. intergrowth tungsten bronze (ITB). [101, 106]

The property changes are attributed to the donation of the intercalate's electrons into the unoccupied 5d-orbitals of tungsten giving rise to metallic conductivity above a certain stoichiometric threshold. [104] Filling of these orbitals has a stabilizing effect with regard to WO bond angles of 180° and thus generally is driving the structure towards cubicity with increasing intercalate concentration. [13, 104] The same phenomenon has been described above in the comparison of tilting behavior between the trioxides of tungsten and rhenium.

The hydrogen bronze differs in several ways from other bronzes with e.g. Li or Na. Generally the A cation in A_xWO_3 sits in the center of the cuboctahedral void limiting the value of x to one. However, in case of the hydrogen tungsten bronze $H_{0.5}WO_3$ the protons were found to bind closely to the framework oxygens producing hydroxo-functionalities. [107] DFT calculations showed the formation of aqua-motifs on bridging atoms to be energetically less favorable, theoretically increasing the limit of intercalated hydrogens to the number of bridging oxygen atoms vacant for the formation of hydroxyl-groups. [108] This is in line with positions and transport mechanisms of additional protons in the bronzoid-analogues of the hydrotungstates. [86, 96, 109]

Further related structures

The low energy barriers between different tungstate polymorphs allow for easy introduction of shear planes, columnar rotations, tricluster or channels and an extensive overview of further related tungstate structures and their crystal chemistry is given by Tilley. [110]

For more information on how the previously mentioned structure types relate to and are located in the dendritic hierarchy of other perovskite-like structures the reader is referred to the comprehensive review by Aleksandrov and Beznosikov. [111]

Techniques for chemical modifications and transitions between different (layered) perovskite-like structure families have been reviewed and summarized by Schaak and Mallouk. [70]

1.2 Properties of layered tungstates

The properties of tungsten oxides have been studied for a many years and a few of the most prominent fields of application are electrochromism[112–114], photocatalysis[115, 116], superconductivity[117–119]. Many of these are based on the structure type, particle morphology and/or some kind of intercalation/vacancies. Especially the layered hydrotungstate have proven to be a versatile basis for property tuning in the tungsten oxide system.

Property investigations on the hydrotungstates are mostly concerned with H_2WO_4 while publications on $H_2W_2O_7$ are less abundant. Relevant studies often focus on

their use as precursor material for different tungstate morphologies[120] like platelets[121, 122], nanosheets[90] , -belts[123], -tubes[124, 125], -rods[126] and snowflakes[127], often via intercalation of organic molecules of variable length into the interlayer and subsequent exfoliation of the perovskite layers[128]. The properties of WO_3-like nanomaterials are an extensively studied topic and a broad range of applications have been identified. [120, 129]

Focusing on the non-exfoliated, bulk hydrotungstates some of the already mentioned general properties, such as ionic conductivity and associated electrochromism, as well as some highly peculiar ones, i.e. pseudocapacitance, have been found. The $n = 1$ hydrotungstate H_2WO_4 behaves similar to 3D the tungsten bronzes upon intercalation of Li[130] and H[131]. In fact, the achieved fast protonic charge/discharge rates and the inertness of the structure classify as pseudocapacitive storage behavior, i.e. redox reaction with only electrostatic instead of chemical-covalent bonding, like in batteries. [86] Interestingly, the transport mechanisms differ and efficiencies in H_2WO_4 without interlayer water are lower compared to WO_3 or $H_2WO_4 \cdot xH_2O$ with interlayer water. [109, 132] $H_2WO_4 \cdot xH_2O$ furthermore features photocatalytic activity for water oxidation under visible light. [133] Bronzoid behavior and associated chromism upon proton insertion have also been demonstrated for the $n = 2$ member $H_2W_2O_7$ with charge capacities exceeding those of the single layer hydrotungstate. [96] Photocatalytic studies are not known to the author but a respective activity seem to be highly probable due to the close correlation between the hydrotungstates. Again, the lack of studies targeted at the $n = 2$ compound is remarkable and future investigations offer high potential for further findings.

Also in the bulk Aurivillius-type bismuth tungstates a range of intriguing properties have been found and studied for prospective application. Bi_2WO_6 is well known to for its oxygen ionic conductivity[47, 134] and for exhibiting ferroelectricity[36, 51]. $Bi_2W_2O_9$ lacks ferroelectricity as previously discussed, however, the possibility for antiferroelectricity has been proposed although experimentally not achieved so far. [58] Chromism of the usually white bismuth tungstates can also be observed, e.g. ultraviolet (UV)-light induced and thermally reversible in the $n = 1$ member or electrochemically for both. [135, 136] Light absorption in the visible range makes them also interesting for photocatalytic applications, such as for the decomposition of organic dyes[137, 138] or for water splitting[139–141].

Structural and chemical modifications of layered tungstates thus is an extensive playground and offers many possibilities to tune the resulting properties. This makes the in-depth structural characterization of these compounds an essential waypoint to have a baseline for further modifications.

1.3 Intention of this research

The here presented studies are aiming to shed light on the structural peculiarities of layered tungstate materials.

Firstly, the thorough thermal characterization of the widely known visible-light

photocatalyst Bi_2WO_6 by means of temperature-dependent X-ray diffraction, Raman spectroscopy and DSC. A focus lies on the distortion analysis of the coordination spheres and relation to previously reported phase transitions.

Secondly, structural elucidation of the until now rather unexplored $n = 2$ hydrotungstate $H_2W_2O_7 \cdot xH_2O$ with the initial goal of finding a reasonable average structure model. Over the course of the project additionally the question gained importance how the previously reported defects actually form and whether possible ways of improving structural quality can be identified. A deeper understanding of defects and structural distortions in this compound is crucial for tuning of its synthesis conditions and the materials properties. With regard to the intercalation possibilities of the vacant A-site the $n = 2$ hydrotungstate $H_2W_2O_7 \cdot xH_2O$ is highly interesting for potential applications in a wide range of fields, e.g. electric and/or ionic conduction as well as storage, photocatalysis or chromic devices.

2 Experimental & analytical methods

2.1 Synthesis

2.1.1 Aurivillius-type $Bi_2W_nO_{3n+3}$

The samples of the composition $Bi_2W_nO_{3n+3}$ with $n = 1$ and 2 were prepared by standard solid state synthesis techniques, following the report of Schaak and Mallouk. [90]

Stoichiometric mixtures of Bi_2O_3 (Alfa Aesar, $\geq 99\%$) and WO_3 (Sigma Aldrich, $\geq 99\%$) powders were ground under acetone in an agate mortar to achieve homogeneous distribution of the metals. The mixtures were placed in alumina crucibles and heated uncovered at 1073 K for 48 h with a heating rate of $5\,\mathrm{K\,min^{-1}}$ in a muffle furnace (Carbolite CWF 1200). At roughly half of reaction time, samples were taken out of the furnace for an intermittent grinding under acetone.

The yellowish green starting mixtures resulted in bright white powders after reaction.

2.1.2 Ruddlesden-Popper-type $H_2W_2O_7$

For the synthesis of $H_2W_2O_7$ Aurivillius-type $Bi_2W_2O_9$ precursors were prepared as described above. Usually, 1 g of precursor material was suspended in 200 mL of $6\,\mathrm{mol\,L^{-1}}$ hydrochloric acid and stirred at room temperature for 48 h in a closed reaction vessel. The canary yellow precipitate was washed/sonicated three times with 20 mL fresh acid to remove the BiOCl side product and dried in a drying oven at 393 K.

The leaching procedure was adjusted for preparation of deuterated samples for neutron powder diffraction. All steps were performed under dry nitrogen atmospheres applying typical Schlenk techniques. Empty reaction vessels were heated to remove surface bound water and were assembled in hot state. A total of 10 g of target compound $D_2W_2O_7$ was produced from 19.2 g of parent material in 4 batches ($\sim$5 g parent material each). Instead of regular hydrochloric acid 50 mL 6 M DCl in D_2O was used (50 mL per batch) and injected into the reaction vessel. After the reaction, the product was let to sediment. The used DCl supernatants of each batch were removed by pipette, combined and distilled under nitrogen atmosphere to remove unwanted bismuth side products. The distillate was reused for the washing procedure and each batch was washed three times with qty10ml recycled DCl. After check for complete removal of bismuth by energy dispersive X-ray spectroscopy (EDX) and phase purity by XPD, the batches were combined and dried. The drying

took place in an evacuated desiccator, placed in a drying oven at 393 K overnight. The dried sample was stored under nitrogen atmospheres.

2.2 Analytics

2.2.1 Diffraction

In-house X-ray

For routine structure analysis, powder diffractograms were measured on a Panalytical X'Pert Pro (Panalytical, Almelo, The Netherlands) in Bragg-Brentano geometry with Ni-filtered $Cu_{K\alpha_{1,2}}$ radiation and an X'Celerator linear position sensitive detector. If not stated otherwise, the standard measuring covered angles of 5° 2θ to 85° 2θ with a step size of 0.0167° and a measuring time of 2 s/step. Samples with flat surfaces were prepared via manual pressing into sample holder cavities (backload process) or as slurries on silicon single crystals.

Additional measurements were carried out on a D8 Discover (Bruker AXS GmbH, Karlsruhe, Germany) in Bragg-Brentano geometry with $Cu_{K\alpha_{1,2}}$ radiation. The knife-edge formed beam was detected using a LynxEye-XET detector and energy discrimination.

High-resolution data were collected on a Stoe StadiMP (Stoe & Cie, Darmstadt, Germany) with Ge(111) monochromatized Mo radiation equipped with a Mythen 1K linear position sensitive detector (Dectris, Baden-Daettwil, Switzerland). Room-temperature diffractograms were acquired in transmission geometry with samples filled in 0.3 mm capillaries in an angular range from 5° 2θ to 55° 2θ ($H_2W_2O_7$).

Temperature-dependent measurements below ambient conditions were obtained on the Stoe StadiMP with a PheniX cryo attachment (Oxford Cryosystems, Oxford, United Kingdom) in Bragg-Brentano geometry in the range from 300 K to 13 K in 10 K steps. Samples were prepared as slurries and fixated with silver containing adhesive for good thermal contact.

For high-temperature studies the X'pert was equipped with an HTK 1200N oven (Anton Paar, Graz, Austria). Temperatures were elevated in 10 K steps from ambient up to 600 K and 1100 K for $H_2W_2O_7$ and $Bi_2W_nO_{3n+3}$, respectively, with 5 min equilibration time on each step.

Synchrotron

High Q-range and high-resolution diffraction data were measured in Debye-Scherrer geometry with high energy synchrotron radiation (100.6 keV) on the Swedish material science beamline P21.1 at Deutsches Elektonen Synchrotron (DESY, Hamburg, Germany). Samples for measurements at ambient conditions were prepared in 1 mm Kapton capillaries. For temperature-dependent experiments 2 mm Quartz capillaries were used. The horizontally oriented capillaries were only filled halfway to allow for decomposition products to escape freely. During the temperature-dependent experiments the sample was heated by a hot-air blower from RT to approx. 628 K with

a heating rate of roughly 4.4 K min^{-1}. The diffraction patterns were recorded on a Perkin Elmer XRD1621 flat panel detector. The instrument geometry parameters were evaluated against a Ni standard and subsequently the 2D patterns were radially integrated using *pyFAI* software package. [142]

Neutron

High-resolution powder diffraction experiments with neutrons were performed on the SPODI diffractometer at the Research Neutron Source (FRM II) at the Heinz Maier-Leibnitz Zentrum, Garching, Germany. [143] The neutron radiation was monochromatized by means of a Ge(551) wafer stack to a wavelength of 154.8 pm, comparable to those of copper X-rays. A deuterated hydrotungstate sample was contained in a vanadium canister inside a helium cryostat and a series of diffraction patterns in the angle range from 3° 2θ to 155° 2θ were recorded from cryogenic to room temperature (4 K, 20 K to 300 K with 20 K steps).

Rietveld refinements

The *DIFFRAC.TOPAS v6* software package (Bruker AXS GmbH, Karlsruhe, Germany) was used for the analysis of powder diffractograms by Pawley fitting and Rietveld refinements. The software employs a fundamental parameter approach during the refinement to account for the instrumental contributions, which were determined from NIST SRM 660b LaB_6 standard material. Diffuse background scattering was generally treated as 5th order Chebyshev polynomials. In routine evaluations, refined parameters included sample displacement error, cell parameters, crystallite size and atomic positions.

The analysis of the temperature-dependent series of both bismuth tungstates was performed in the same manner. The two data sets at 300 K from LT- and HT-setups were corefined accounting for the respective instrumental contributions. The refined structures served as the starting models for the sequential refinements which were then performed on each data range individually, including once more the 300 K data sets, towards high and low temperatures, respectively.

A combination approach was used for elucidation of the $H_2W_2O_7$ structure. Based on the aforementioned hypothesis that the tungsten oxide sheets of the parent $Bi_2W_2O_9$ remain intact while the $Bi_2O_2{}^{2+}$-layers are removed and exchanged against protons during leaching, different structure models were built. Each model was then simultaneously refined against ambient diffraction data from both, X-ray and neutron scattering experiments. The refinements were set up in a manner that the individual instrumental contributions were accounted for as well that hydrogen positions were only refined against the neutron data.

In refinements of data from samples prepared as slurries additionally the contributions due to surface roughness were treated.

Visualization of structure models

Visual inspection of the structure models and production of respective figures were performed with *VESTA* (JP-Minerals)[144], *Diamond Version 4* (Crystal Impact) and the *Atomic Simulation Environment ASE*[145].

Coordination environment analysis

The polyhedral coordination in different structure models was analyzed with a series of derived parameters.

From the bond lengths $l_{\mathrm{WO}} = r_{ij}$ the bond valences s_{ij} and the bond valence sum BVS were calculated according to Brown and Altermatt,

$$BVS = \sum_j s_{ij} = \sum_j \exp\left(\frac{r_0 - r_{ij}}{B}\right) \tag{2.1}$$

with the bond valence parameter nominal bond length $r_0 = 191.7(4)\,\mathrm{pm}$ for the pairing $\mathrm{W^{6+}}$ / $\mathrm{O^{2-}}$, $r_0 = 209.4\,\mathrm{pm}$ for the pairing $\mathrm{Bi^{3+}}$ / $\mathrm{O^{2-}}$ as well as $B = 37\,\mathrm{pm^{-1}}$ for both. [146] The bond valence model relates the individual bond lengths to a valence contribution, which in sum should match the nominal valence of the central cation, e.g. six for $\mathrm{W_6}^+$. It has to be noted though that these are experimental parameters based on surveys of literature published structure models. As such and without further adjustment the bond valence model is strongly biased towards the bonding situation at ambient conditions.

Another approach to describe arbitrary coordination polyhedra is the fitting of a minimal bounding ellispoid (MBE) implemented in the *pieface* software package. [147] The MBE encompasses all ligands of a central atom irrespective of the actual polyhedral geometry. The volume and orientation of the ellipsoid is reduced and adjusted, respectively, until a given fitting tolerance is achieved (chosen here to be 10^{-5}). Consequently, the three ellipsoidal radii R_1, R_2, R_3 and ellipsoid volume V_{ellip} are functions of the bond length distribution around the central atom. If the coordination polyhedron resembles a platonic body, e.g. a regular octahedron, the MBE is spherical with equal radii and its shape parameter

$$S = R_3/R_2 - R_2/R_1 \tag{2.2}$$

has a value of $S = 0$. Any derivation from the platonic geometry leads to disparate radii and either a prolate ($0 < S < 1$) or oblate ($0 > S > -1$), i.e. lengthened or flattened ellipsoids, respectively. The mean radius $\langle R \rangle$ and radii variance $\sigma^2(R)$ are thus measures of the polyhedral distortion. The position of the central atom with respect to the ellipsoid center also serves as quantifier for the off-centering frequently encountered in *d*0-elements and being especially typical for $\mathrm{W_6}^+$. Cumby and Attfield show that the ellipsoid analysis is highly sensitive to the tilting behavior in perovskites. [147] Furthermore, changes in the shape parameter S are indicative of phase transitions in perovskite structures, with symmetry forbidden transition

always changing the sing of S. [147] Although not explicitly addressed by Cumby and Attfield, similar applicability to Aurivillius- and Ruddlesden-Popper-type structures is assumed since both are part of the perovskite-like family.

In case of the hydrotungstate structure models, the software packages *VESTA* was used to extract additional geometric and distortion parameters. [144, see also the software manual] These include the polyhedral volume V_{poly}, average bond length $\langle l_{WO} \rangle$ and bond length variance $\sigma^2(l_{WO})$. Distortion quantifier based on the relations to regular polyhedra are the quadratic elongation $\langle \lambda \rangle$ and the bond angle variance $\sigma^2(\phi)$ defined by Robinson, Gibbs and Ribbe [148] as

$$\langle \lambda \rangle = \frac{1}{n} \sum_{i=1}^{n} \left(\frac{l_{WO_i}}{l_0} \right) \sigma^2(\phi) = \frac{1}{m-1} \sum_{i=1}^{m} (\phi_i - \phi_0)^2 \tag{2.3}$$

with l_0 as the center-apex-distance of a regular polyhedron of same volume, m the number of bond angles in the polyhedron and phi_0 the ideal angle.

Furthermore, the distortion index D as defined by Baur [149] is calculated by *VESTA* according to

$$D = \frac{1}{n} \sum_{i=1}^{n} \frac{|l_{WO_i} - \langle l_{WO} \rangle|}{\langle l_{WO} \rangle} \tag{2.4}$$

In addition to distortion index D provided by *VESTA*, another distortion index Δ as defined by Brown and Shannon [150] is calculated via the slightly different relationship

$$\Delta = \frac{1}{n} \sum_{i=1}^{n} \left(\frac{l_{WO_i} - \langle l_{WO} \rangle}{\langle l_{WO} \rangle} \right)^2 = \frac{\sigma^2(l_{WO})}{\langle l_{WO} \rangle^2} \tag{2.5}$$

2.2.2 Spectroscopy

Infrared spectroscopy

For routine Fourier-transform infrared spectroscopy (FTIR) measurements in the mid-infrared range, a Nicolet iS 10 with Smart iTR attenuated total reflection (ATR) attachment (Thermo Scientific) was used. Sample powders were pressed onto the diamond crystal in a repeatable manner by a pressure screw. Additional spectra were recorded on a Vertex 70v (Bruker Optik, Bremen, Germany), with pressed discs from mixtures of 2 mg sample in 200 mg KBr.

Raman spectroscopy

Raman spectra were recorded on a LabRAM Aramis spectrometer (Horiba/Yvon) including an Olympus BX-41 confocal microscope and Synapse CCD detector. The grating exhibits 1800 grooves/mm and a slit aperture width of 100 µm was chosen. For the bismuth tungstate samples a laser wavelength of 532 nm was chosen whereas for hydrotungstate samples a laser with 785 nm wavelength was used to prevent radiation damage.

For temperature-dependent Raman studies in the ranges 80 K to 500 K and 300 K to 1100 K samples were placed in THMS350V and TS1200 stages (Linkam), respectively.

Second-harmonic generation

Presence of second-harmonic generation (SHG) was probed at crystallography department, Uni Frankfurt, to check for centrosymmetry in $H_2W_2O_7$ powders. Fundamental pump waves with several wavelengths (1096 nm, 1136 nm, 1196 nm, 1236 nm, 1276 nm, 1316 nm, 1354 nm, 1394 nm, 1434 nm and 1474 nm) were generated by means of a Q-switched Nd:YAG laser (5 ns to 6 ns, 10 Hz, Continuum, Surelite) with optical parametric oscillator. Any frequency doubled intensity at the related regions of half the pump wavelengths was separated by short-pass filtering and detected by a grating spectrometer (Acton, SP- 2356) equipped with a CCD detector (Pixis 256E) with varying collection time per window. Quartz and Al_2O_3 served as references for SHG-active and -inactive materials, respectively. The setup schematics are shown in [151].

Nuclear magnetic resonance spectroscopy

The solid-state nuclear magnetic resonance (NMR) spectra were recorded with an Avance III HD 500 spectrometer connected to an Ascend 500 WB (Bruker BioSpin GmbH, Ettlingen, Germany). The nominal 11.7 T magnetic field strength corresponds to a Lamor frequency of 500.45 MHz for the ^{1}H nucleus. The experiment used a 1D *hahnecho* pulse program with 1.67 µs pulse length with a power level of 73.35 W. The sample was spun under magic-angle spinning conditions at 40 kHz with temperature-controlled bearing gas (300 K), which resulted in a sample temperature of approximately 338 K.

Data analysis

FTIR, Raman and NMR spectroscopic data with peak-shaped signals were analyzed by means of Levenberg-Marquardt least-squares fitting of pseudo-Voigt functionals. In case of the in-situ Raman measurement series (temperature-dependent and leaching) the IDL-based software *LAMP* was used. [152] In other cases fitting was performed with the help of the python package *LMFit* and the *fityk* software. [153, 154]

2.2.3 Thermoanalysis

High-precision DSC measurements of the bismuth tungstates were recorded on a DSC3+ (Mettler Toledo) in the temperature range from 80 K to 680 K with a heating rate of 10 K min^{-1}.

2.2.4 Microscopy & Elemental analysis

Particle morphology and elemental analysis via scanning electron microscopy (SEM) and EDX was performed on a JMS-6510 (JEOL) equipped with an X-Flash 410-M detector (Bruker) with an acceleration voltage of 20 kV. Sample powders were sprinkled on carbon sticky tabs and subsequently Au sputtered for 20 s to 30 s in a low-pressure Ar atmosphere.

Additionally, TEM micrographs were produced on a FEI Tecnai Titan 80/300 G1 using an acceleration voltage of 300 kV. Sample powders were prepared as ethanolic slurries and washed onto copper grid supported amorphous carbon films.

3 Thermal Behavior of Aurivillius-type Bismuthtungstates

The thermal behavior of the $n = 1$ Bi_2WO_6 has been studied for some time (see introduction in subsubsection 1.1.2), however, advances in instrumentation and analysis techniques can provide new insights also into well studied systems. For the $n = 2$ $Bi_2W_2O_9$, temperature-dependent investigations were scarce at the start of the project and especially the LT region was not addressed in detail before the publication by Tian et al. in 2018 [52] to the best of the author's knowledge. The intention of this study is a detailed investigation bridging both LT and HT regions and a comparison of the results with literature reported features. A special focus is given to correlating our findings with tentative results or yet unaddressed features in literature data.

Due to time constraints the detailed analysis of the $n = 2$ $Bi_2W_2O_9$ compound did not make its way into this thesis. The comparative study between the two Aurivillius tungstates is subject of future works.

3.1 Analysis details

Two problems affect the expressiveness of the obtained results.

The first problem is related to strongly differing scattering contributions of the compounds constituents. The information contained in the diffractograms are dominated by the high-Z elements tungsten and bismuth, whereas information on oxygen is comparably low. This can be circumvented by neutron diffraction, however, the experimental facilities are few and usually long data collection times are needed. For a study of a large temperature range with high-resolution in the temperature domain this is not possible. Another possibility is to use restraints on the metal-oxygen bond lengths or refining fixed coordination, i.e. rigid bodies, as additional observations from chemical knowledge. However, the application of restraints can to some extent bias the results. The chemical knowledge the restraint is building upon is often related to room-temperature experiments only and/or statistical averages in which distorted structures are possibly underrepresented.

In this study a different approach was chosen. All atomic positions were refined freely apart from restrains imposed by the symmetry of the structure model and an anti-bump to prevent light atoms "falling into" heavy atoms. The aim of this study lies not in the refinement of the models with exact positions and precisely derived parameters, which for these compounds is hardly achievable with X-ray diffraction. Instead, the extraction of relative trends and points of structural instabilities over a

wide temperature range is sought. These trends can serve as a basis for more precise investigations at that specific regions with more suitable probes.

A second problem with temperature-dependent (TD) studies is the fact that experimental setups only cover limited ranges. This problem is usually addressed by measuring with sufficiently sized region of temperature overlap. Unfortunately, our diffraction measurement setup can not provide a continuous examination around the RT regime. The switch from LT to HT setup at 300 K allows only this temperature to be measured on both setups. The observed discontinuity in some fractional coordinates of the atomic positions and respective derived parameters can therefore not exclusively be attributed to an actual structural phenomenon. The influence of the setup change and can neither be clearly separated nor its magnitude be estimated with sufficient confidence. Without additional continuous measurements around the 300 K mark, most of the sudden changes, i.e. steps between the LT and HT ranges, have to be attributed to the change in measurement setup. Nonetheless, the relative trends and discontinuities within the respective temperature ranges, also in the vicinity of the setup switch are considered legit sample effects.

Even without precise atomic positions, as outlined above, the cation coordination environments were investigated by fitting the MBE encompassing the coordination polyhedron as described in subsubsection 2.2.1. The results shown below illustrate that the coordination analysis is an ill-posed problem due to lack of appropriate data and information on precise oxygen positions. While not providing physically meaningful absolute values, respective trends in the parameters could nonetheless give hints towards structural changes and instabilities.

The results of the ellipsoid analysis of the Bi environments are not considered in detail. Since it could only be performed on the first coordination sphere within a 30 pm radius instead of the full antiprism the interpretability in terms of comparison to platonic bodies is not given. Increasing the radius to also include the long-distanced oxygen atoms of the full antiprism poses the problem of including unwanted symmetry-equivalents. Unfortunately, the as-provided software executable for ellipsoid analysis *pieface*[147] is not capable of excluding specific symmetry-equivalent atoms. The calculation on the full antiprism thus requires significant more work to write a respective analysis script which is beyond the project limits and subject of future investigations.

The data from diffraction experiments are compared to the results of temperature-dependent Raman spectroscopy measurements. For these also two setups were used in the ranges 85 K to 500 K and 300 K to 1100 K The large overlap from 300 K to 500 K and the LT-setup continuously covering the RT region provides a solid reference.

Additionally, high-resolution DSC measurements in the temperature range from 125 K to 600 K are presented for reference.

3.2 Diffraction experiments

3.2.1 Autocorrelation and Rietveld parameters

The identification of changes in the sample state during investigations based on external parameters, i.e. here temperature, can be a difficult task. The autocorrelation analysis as described by Robben provides a valuable tool. [155] It is sensitive even to small changes in peak shapes and intensities given sufficient data quality. These changes in the raw data show as discontinuities, e.g. steps or gradient changes in the plot of the autocorrelation parameter λ'. Depending on the chosen lag value, i.e. the shift between the identical datasets when calculating their correlation value, autocorrelation parameter λ' is more sensitive to sharp and broad features at lower and higher lag values, respectively.

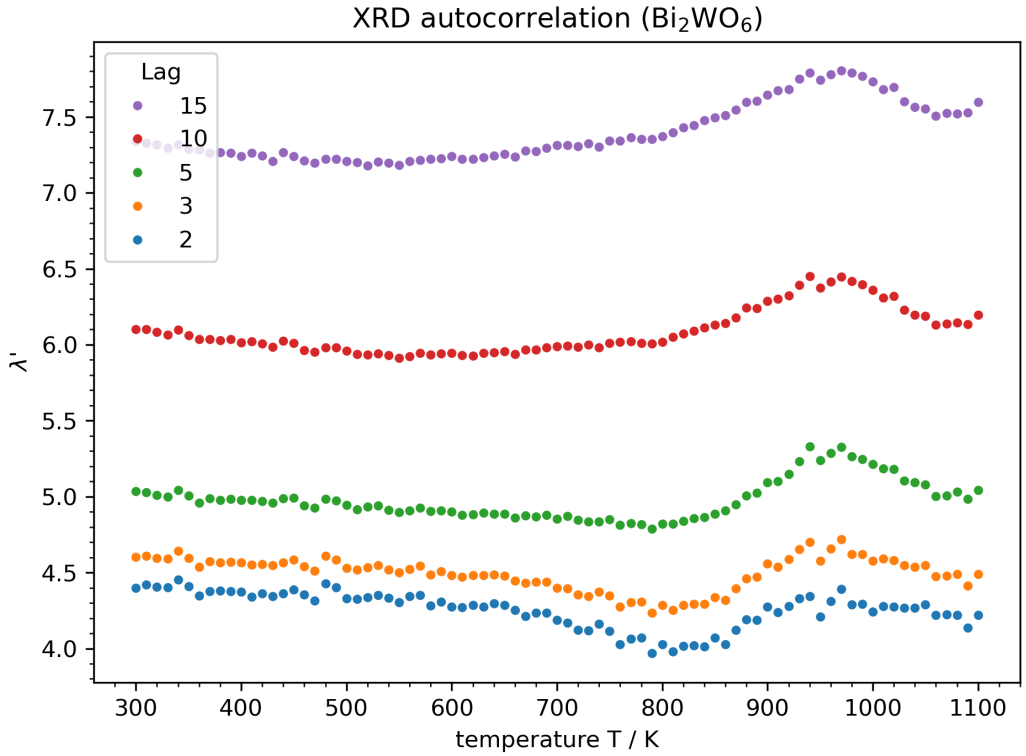

Figure 3.1: Values of the autocorrelation parameter λ' with different lags calculated from the HT X-ray diffraction data.

The autocorrelation analysis of the LT measurements can not provide any useful information as the low Q-resolution together with the signal-to-noise ratio (SNR) overshadow any minor changes in the reflection peak shape. For the HT measurements, the results are presented in Figure 3.1. Minute steps in the low lags of the autocorrelation at 350 K and 500 K, followed by a change of slope at 650 K to 700 K

are indicative of small changes on sharp signals. The slope of high-value lags change continuously over the temperature range, while for the low-value lags a clear change in slope appears at 800 K. The discontinuity at 930 K visible for all lags is a clear indicator for the reported phase transition at that temperature.

The diffraction data were analyzed by Rietveld refinement and the starting model was corefined to the 300 K data sets of both setups. The sequential Rietveld refinement runs started with this room-temperature structure model. An overall good agreement with the data is indicated by the low R_{wp} residual values over the investigated range from ~20 K to 1100 K (Figure 3.2). Further general parameters such as cell parameters, sample displacement and crystallite size are also plotted in Figure 3.2.

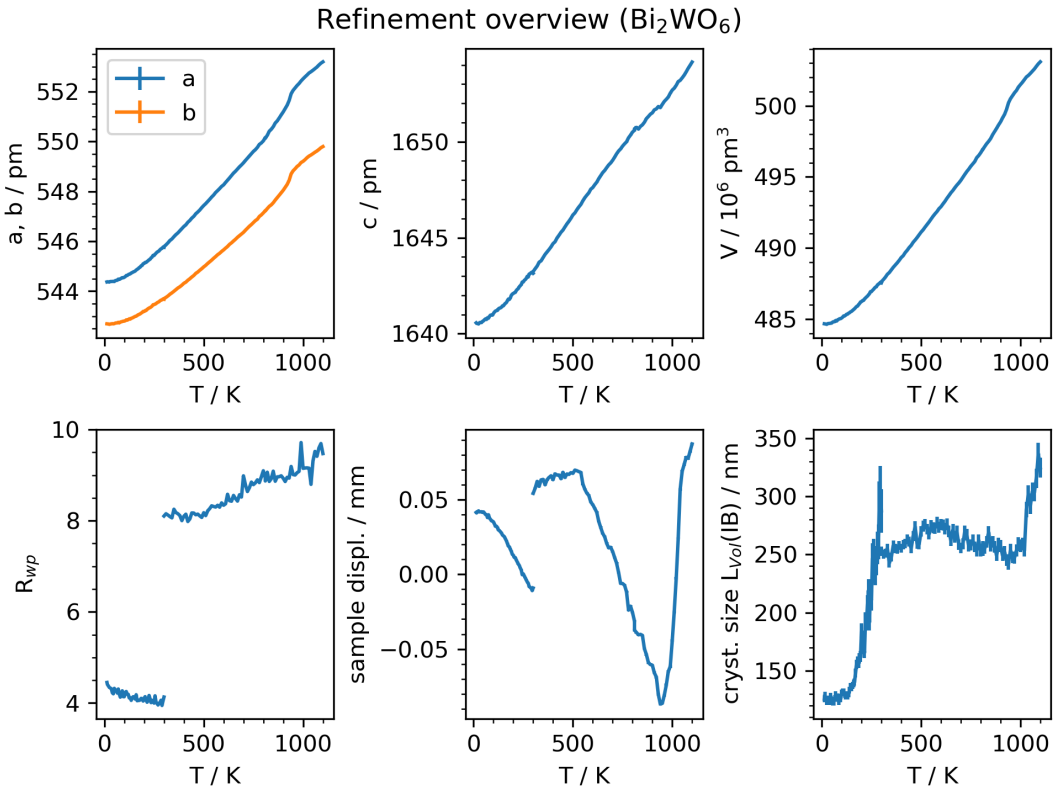

Figure 3.2: Parameters obtained from Rietveld refinement of Bi_2WO_6. Shown are the unit cell parameters, agreement factor, sample displacement and crystallite size.

The R_{wp} in the LT regime gets slightly better with increasing temperatures up to the setup change at 300 K, however, the improvement is small. The model agreement is constant from room temperature on and starts to worsen from 520 K on. After reaching a plateau at about 800 K the R_{wp} starts to worsen again after reaching the phase transition temperature of 930 K.

After a smooth change of the lattice parameters a and b up to RT, a constant thermal expansion is apparent over the whole temperature range up to approx. 920 K. From there, an abrupt slope change is indicative of the proximate reported phase transition at 930 K after which the increase is approximately linear again. In the c lattice parameter there is small downwards step at 820 K and we see only a small step at the phase transition temperature of 930 K The small first step in the c lattice parameter is not reflected in cell volume behavior as it only shows the phase transition at 930 K.

The LT development of the sample displacement corresponds to the thermal expansion of the system of sample and holder and the large step is due to the setup. However, in the sample displacement behavior from the HT setup there is an inflection at 540 K with a massive change in slope. While the origin of this feature is not fully clear it is tentatively attributed to the buckling of the sample due to thermal expansion. At 940 K, the sample displacement behavior reverses which is attributed to a collapse of the previously buckled sample as a result of changes in the particle shape/size during and after the phase transition.

The development of the refined crystallite size at low temperatures correlates strongly with the reported phase transition (order-disorder transition by Bi shifting) below 200 K. [44] While this attribution is tentative the correlation is striking and could be explained by ever so small reflection broadening due to the proposed increased disorder on the bismuth position at LT which is captured by the refinement algorithm in terms of a reduced the crystallite size. Due to the low Q-resolution a comparison of the reflection widths in LT diffraction raw data is not conclusive. However, any influence from particle growth can be excluded at this low temperatures. In the HT range the crystallite size slowly increases to a local maximum around 590 K after which it slowly decreases again. The origin of this behavior is also not clear but is attributed not to an actual crystallite growth but also to an effect of peak broadening due to local disorder, i.e. lattice strain. After the phase transition at 930 K, first a gradual, then after passing a temperature of 1020 K a steep increase in the crystallite size occurs, which can be ascribed to an actual particle growth.

3.2.2 Atomic positions

The atomic positions extracted from the Rietveld refined structure models generally show significantly higher uncertainties in the LT results due to the lower data resolution.

The oxygen position behavior (shown in Figure A1 and Figure A2 in the appendix) is not considered in detail here and is discussed in terms of the resulting bond lengths. On a general note, the oxygen positions exhibit large uncertainties on their fractional coordinates. In some cases large abrupt changes occur, especially in the LT oxygen positions. For the oxygen atoms O1 and O2 located within the bismuth layer the positional uncertainties are highest, illustrating the difficulty associated with scattering contrast of low- and high-Z elements in proximity, as discussed above. With regard to general motifs in the oxygen positions in the HT range,

two temperatures show some sort of abrupt change or discontinuity. The first one around 700 K is clearly visible as a rather sharp peak in almost all coordinates. This feature is attributed to some sort of structural instability and is discussed in more detail further below. The second discontinuity at 930 K is expected and attributed to the phase known transition.

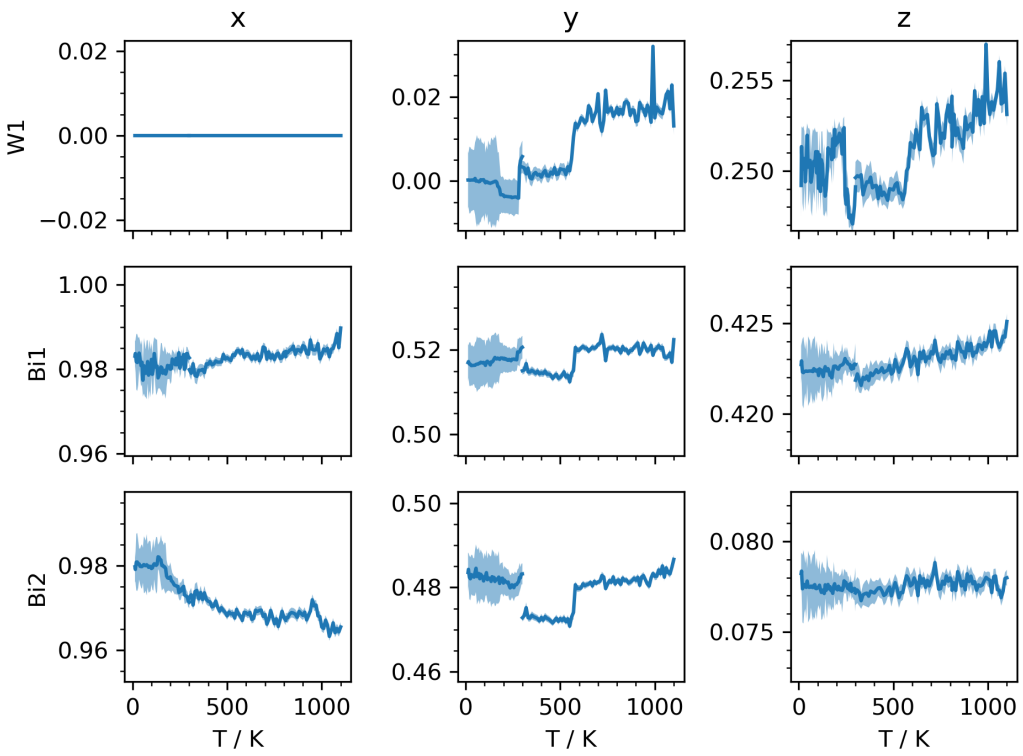

Figure 3.3: Temperature dependent positional coordinates of W1, Bi1 and Bi2 in Bi_2WO_6

The refined cation positions are presented in Figure 3.3 The W1x-coordinate was fixed to a value of zero in order to improve the refinement stability.

As expected from the scattering power, the positional uncertainties in general are significantly lower compared to oxygen. Also for the cations, the uncertainty in the x and y coordinates is comparably large below 150 K. Notably though, a sudden decrease in uncertainty occurs at that mark. This is accompanied by a notable step in W1y and W1z and a change in the slope of Bi2. It seems highly likely that this behavior is of the same origin as the phase transition described by Yoneda, Takeda and Tsurumi. [44] They attributed this to a change in the BiO-WO-interlayer correlations due to a bismuth movement, while here it seems to be shift of both, Bi and W.

Furthermore, the study by Hirose, Kawaminami and Obara suggests that the PT

at 280 K results from a Bi displacement along the stacking direction. [45] This is also in contrast to our results, in which the most drastic changes occur in the z-coordinate of tungsten and only marginally for bismuth. However, all cations shift in the layer plane, as indicated by the step in their y-coordinates, again more obvious for tungsten.

Another very pronounced shift in the y-coordinates appears at 550 K. From this temperature on, the electric permittivity of Bi_2WO_6 starts to increase as shown in Fig. 10 of [48].

Notably, the discontinuity around 700 K seen in the oxygen coordinates is not reflected by the cations. Similarly, only subtle changes at the phase transition temperature of 930 K are visible in the cation positions. This reflects the accepted concept that the phase transition is mainly driven by the oxygen sublattice, i.e. loss of octahedral rotation, while the cation sublattice stays mostly unchanged.

The spike at 990 K in the tungsten y- and z-coordinate might be correlated to the reported strong increase in permittivity around 1000 K. [48] However, since this spike affects only a single data point a refinement artifact seems to be the more plausible cause. Since it also lies close to the upper limit of our investigated temperature range an interpretation in terms of trend changes is not possible.

3.2.3 Derived bond lengths and ellipsoid analysis

Tungsten environment

The resulting bond lengths for the WO coordination are plotted in Figure 3.4, the bond valence sum (BVS) in Figure 3.5, the average bond length $\langle l_{WO} \rangle$ and variance $\sigma^2(l_{WO})$ together with further ellipsoid parameters in Figure 3.6. In the appendix, magnifications of Figure 3.6 in the range below and above 500 K can be found under Figure A3 and Figure A4, respectively.

The parameters show a fair amount of scatter, especially at the high-temperature end. To enhance visibility of the underlying trends a rolling average of five data points is plotted along.

The WO bond lengths of in-plane oxygen atoms O4 and O5 with min/max values of around 150 pm and 270 pm are clearly out of reasonable absolute values. NPD results from literature show that even at elevated temperatures the bond lengths do not exceed 172 pm and 230 pm, respectively. [34] The massive outlier in O4 bond length at 1040 K is considered a refinement artifact at which the anti-bump restraint was eluded.

Neglecting the unphysical absolute values, the most prominent features are a kink centered around 700 K in the behavior of bonds to the O4 atom and an inflection for the O6 bond. For other bonds the effect is marginally, although shifts in the positional coordinates are visible for all oxygen atoms as discussed above. This might be related to a particular instability of O4 atom. As the other equatorial oxygen atom in the octahedron O5 is not affected, the O4 feature is not related to the rotation around the c-axis, which drives the higher temperature phase transition

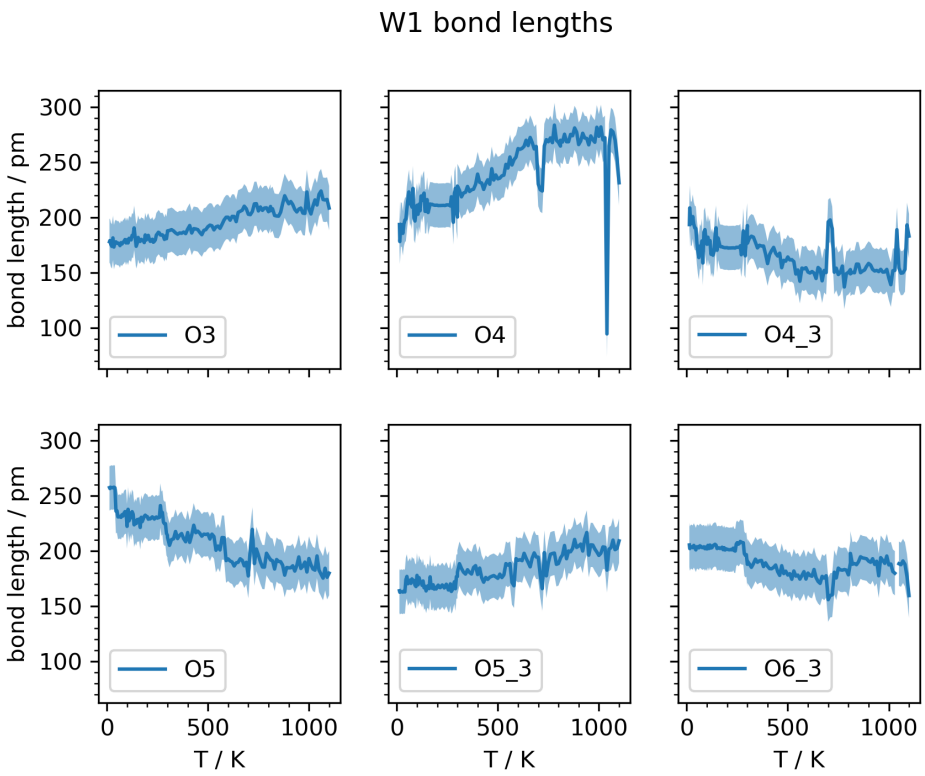

Figure 3.4: Bond length development for the tungsten coordination in Bi_2WO_6

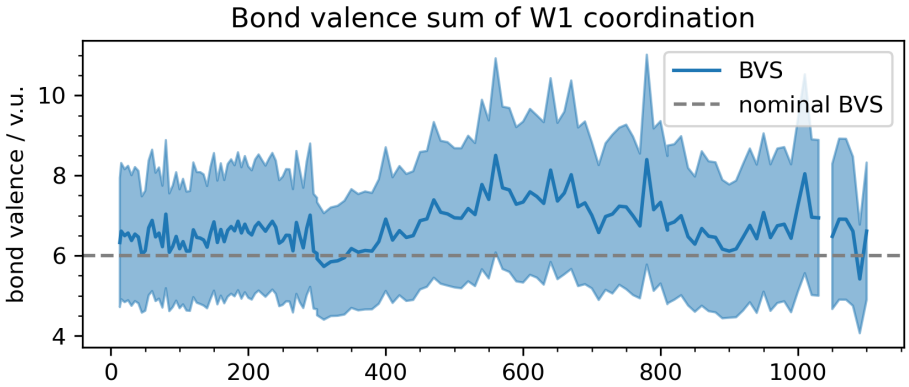

Figure 3.5: Temperature-dependent bond valence sum for the tungsten coordination in Bi_2WO_6

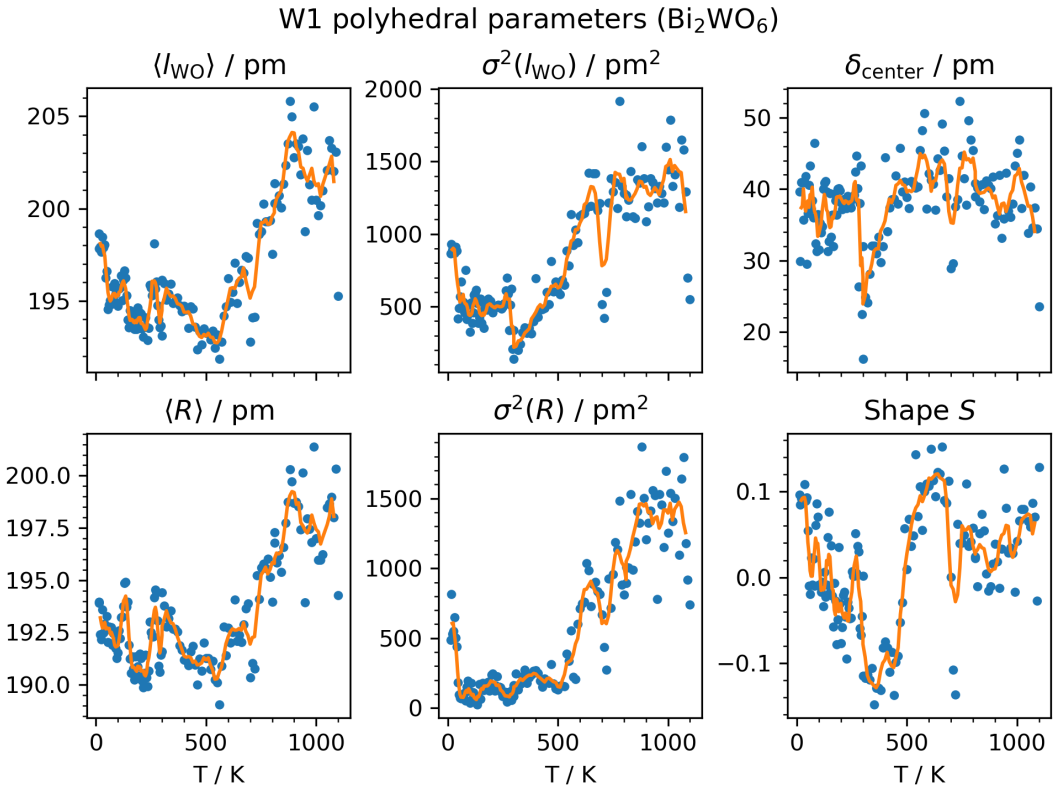

Figure 3.6: Bond length average $\langle l_{WO} \rangle$ and variance $\sigma^2(l_{WO})$ as well as ellipsoid parameters average radius $\langle R \rangle$, radius variance $\sigma^2(R)$, cation off-centering and shape parameter for the tungsten coordination in Bi_2WO_6. The respective lines are rolling averages with a window size of five data points which serves as guide for the eye.

at 930 K.

The kink in the O4 bond length at 700 K is of mutually opposite sign for the two O4 atoms in the coordination sphere. Therefore, the derived BVS shown in Figure 3.5 is only marginally affected, i.e. no major change in trends can be observed at that temperature. The high BVS values of up to 8.5 v.u. reflect that some bonds are extremely short. No distinct discontinuity is apparent in the LT regime and the BVS increases linearly above room temperature until reaching a maximum at 500 K. The subsequent decreases up to the phase transition temperature at 930 K is again followed by an increase to higher temperatures. The discontinuity in the plot is due to the above-mentioned O4 bond length outlier.

As shown in Figure 3.6, the average bond length $\langle l_{WO} \rangle$ and the average ellipsoid radius $\langle R \rangle$ behave similarly and decrease over the whole range from LT to 500 K. The magnification in Figure A3 reveals a slight difference. The average bond length $\langle l_{WO} \rangle$ exhibits a pronounced step around 50 K. This step can also be found in the bond length variance $\sigma^2(l_{WO})$ and the radius variance $\sigma^2(R)$. It is not clear whether this is an actual sample effect or a refinement artifact. While this step is also visible in the O4 and O5 bond lengths, it is within the apparent scattering range of those data points. The LT PDF study by Yoneda, Takeda and Tsurumi gives no hint on changes between 10 K and 100 K. [44] Since no other of our techniques reaches down to those temperatures, a cross correlation is not possible.

In vicinity to above identified critical points at 140 K and 280 K, also $\langle l_{WO} \rangle$ and even more so $\langle R \rangle$ show peak and step features. Above RT, both parameters decrease up to the 500 K mark, from where again an increase to 700 K is apparent. The 700 K discontinuity appears in all of the parameters presented in Figure 3.6. From there on $\langle l_{WO} \rangle$ and $\langle R \rangle$ increase up to the reported phase transition at 930 K. After that, a local minimum at 1000 K is apparent which correlates to the permittivity changes in [48].

The bond variance $\sigma^2(l_{WO})$ drops sharply at 280 K to immediately increase again from 300 K up to 700 K. After the 700 K discontinuity no more drastic changes are visible.

Apart from the 50 K step and a barely visible 280 K minimum, the radius variance $\sigma^2(R)$ shows only a weak decrease at up to the 500 K mark. Different from the bond length variance, the radius variance increase does not seize at the 700 K mark but continues up to 930 K.

The off-centering of tungsten from the ellipsoid center shows only the sharp drop at 280 K and immediate increase again from 300 K. Above 500 K it stays fairly constant although with strongly scattered values.

The sign of shape parameter is a measure of the whether the ellipsoid is prolate (elongated, positive values), oblate (flattened, negative values) or of spherical shape, indicated by a value of zero. Cumby and Attfield showed that symmetry-forbidden phase transitions in perovskites are always associated with a zero crossing of the shape parameter. In our results we can observe zero crossings at 150 K, 280 K, 500 K and possibly also at 700 K. In the regions below and above, some more data points come close to zero or cross it by minimal amounts. However, the data points

also scatter rather strongly in those regions and are therefore not considered legit. Whether the underlying structural changes in this structure actually qualify as symmetry-forbidden phase transitions cannot be determined with certainty. Nonetheless, the possibility that this criterion is also applicable to layered perovskites is highly intriguing.

Bismuth environments

The presence of critical points at 150 K, 280 K, 500 K, 700 K and 930 K has been established above. Without going into the same detailed examination, these critical point also show up in the parameters of the bismuth environments. Notably, however the trends around these critical point are significantly different for the two bismuth coordinations.

The bond lengths are not discussed individually in here but are given for reference in the appendix (Figure A5 and Figure A5)

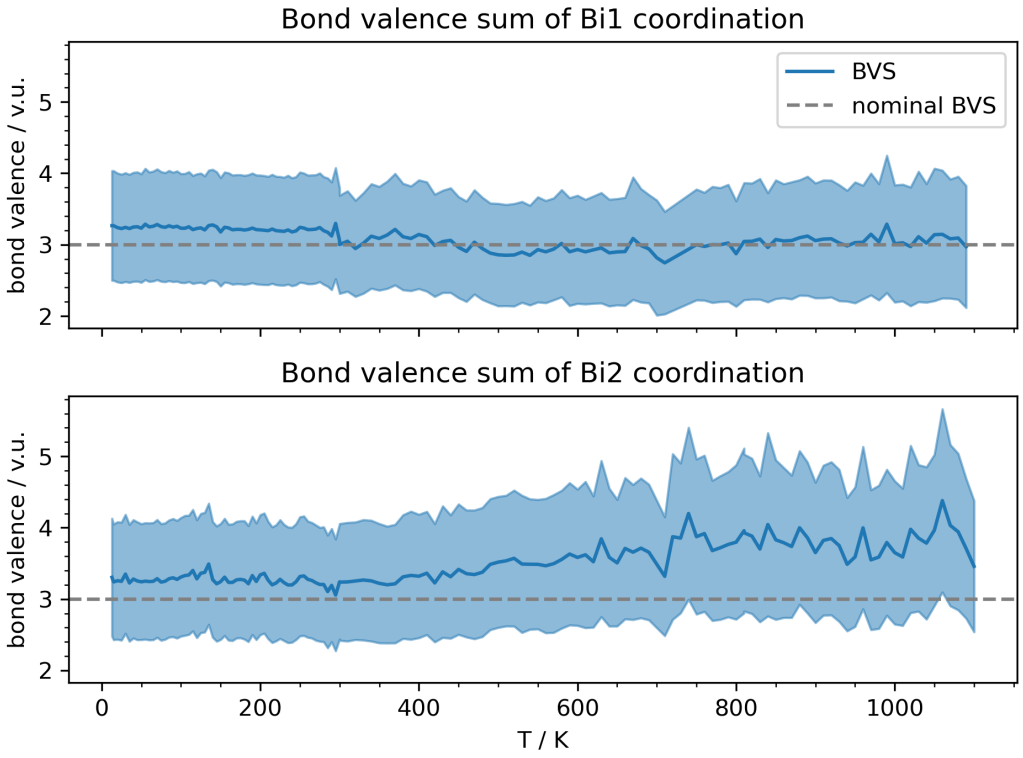

Figure 3.7: Temperature-dependent bond valence sum for both bismuth coordinations in Bi_2WO_6

The bond valence sums shown in Figure 3.7 exhibit only few features. The BVS of Bi1 does not deviate from its formal value of three over the complete temperature range and exhibits no pronounced steps or distinct maxima. Only subtle or slope

changes at the temperatures around 300 K, 500 K and 700 K can be identified. In case of Bi2, three linear segments with the center segment between 300 K and 700 K can be discerned. The BVS increases from its formal value of three to about 3.8 over the range of the center segment. Additionally, a maximum at 1040 K can be seen.

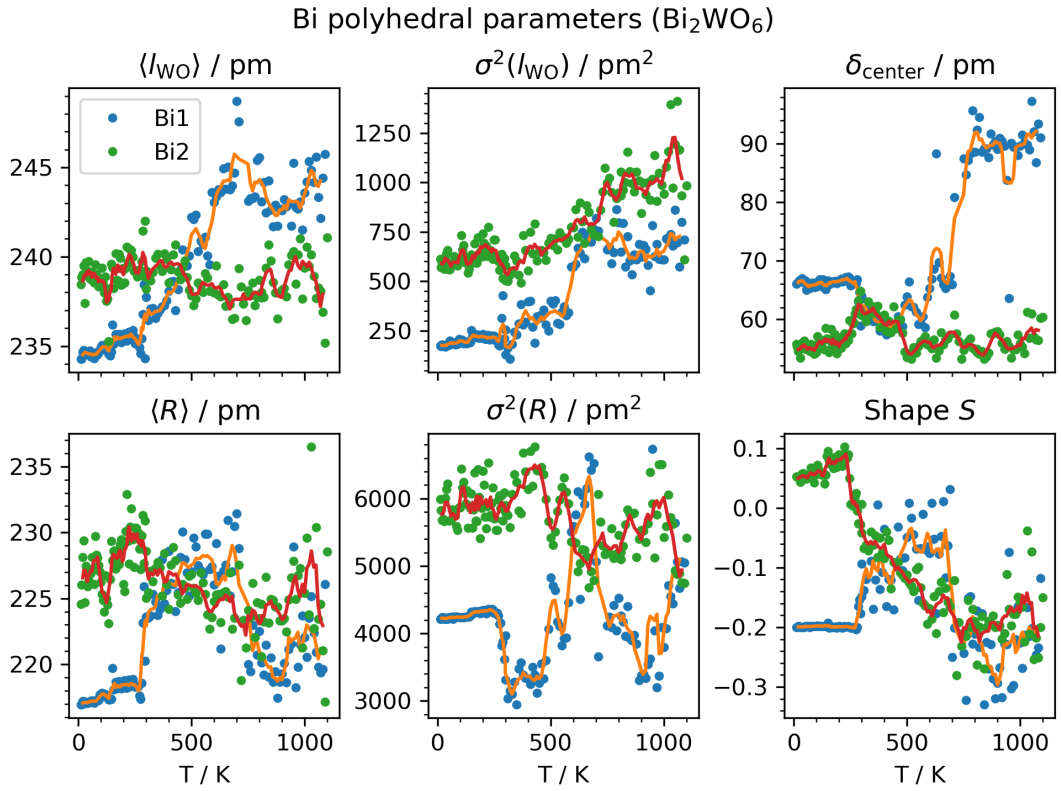

Figure 3.8: Bond length average $\langle l_{WO}\rangle$ and variance $\sigma^2(l_{WO})$ as well as ellipsoid parameters average radius $\langle R\rangle$, radius variance $\sigma^2(R)$, cation off-centering and shape parameter for both bismuth coordination in Bi_2WO_6. The respective lines are rolling averages with a window size of five data points which serves as guide for the eye.

The results from the MBE fitting are presented in Figure 3.8. Interpretation of the ellipsoid off-centering and shape parameters for the bismuth atoms is difficult since their coordination environment is so strongly asymmetric and far from a platonic body. This is for instance reflected by the difference in behavior between the average bond length and radius of the Bi1 coordination. They serve here only as proxy parameters for sudden changes in the coordination.

Notably, there are no only small changes in the ellipsoid parameters of the Bi1 atom, whereas Bi2 shows significant discontinuities. Although the Bi position indeed are symmetry inequivalent to begin with, this distinctively different behavior is quite

surprising. Bi1 and Bi2 are not part of the same intergrowth layer rather each bismuth position is located within its own layer. The different behavior could be interpreted as a modulation, e.g. ABAB stacking sequence, of the bismuth oxide substructure, in which the interaction with the perovskite layer is stronger to one of A or B while the other is less affected However, the tentative nature of this analysis due to the uncertainty in the coordination sphere has to be kept in mind.

3.3 Raman spectroscopy

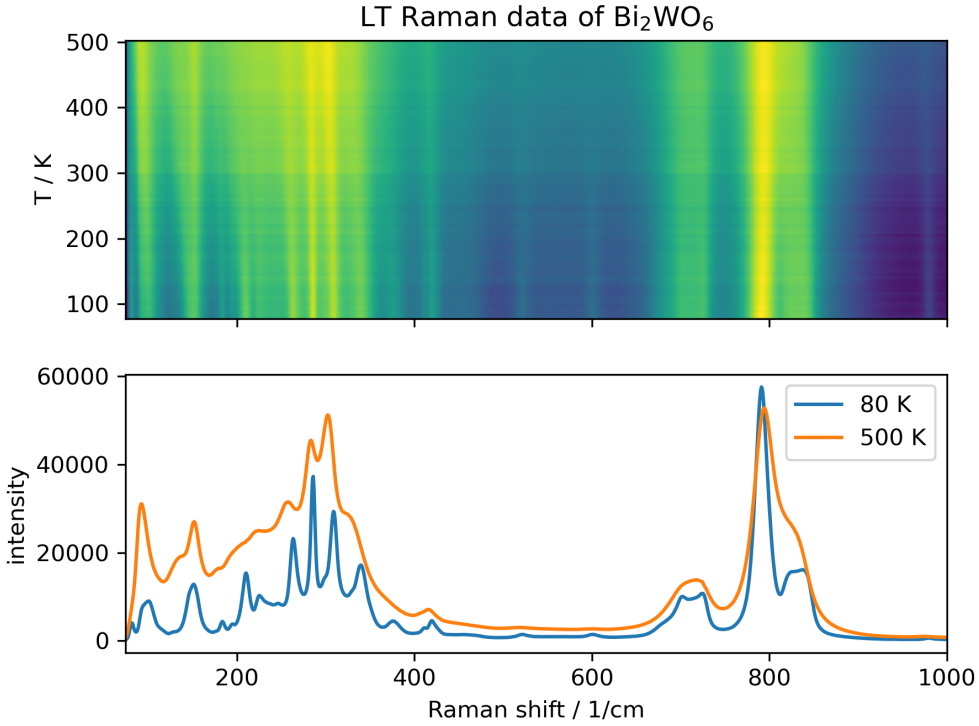

Figure 3.9: Low-temperature $BiWO_6$ Raman spectra

The temperature-dependent Raman spectra from the LT and HT setup are shown in Figure 3.9 and Figure 3.10, respectively. The autocorrelation of these is plotted in Figure 3.11.

The autocorrelation curves show a rather steep development, which is attributed to the broadening of the Raman modes. Since this is a fairly strong effect it is hard to visibly discern smaller changes in the autocorrelation.

The first discernible effect occurs at around 330 K as the slope of all curves in the LT range decreases. For the lags values of 25 and 60, a pronounced change in slope can be observed at around 480 K and a distinct feature in form of a small dip at 580 K

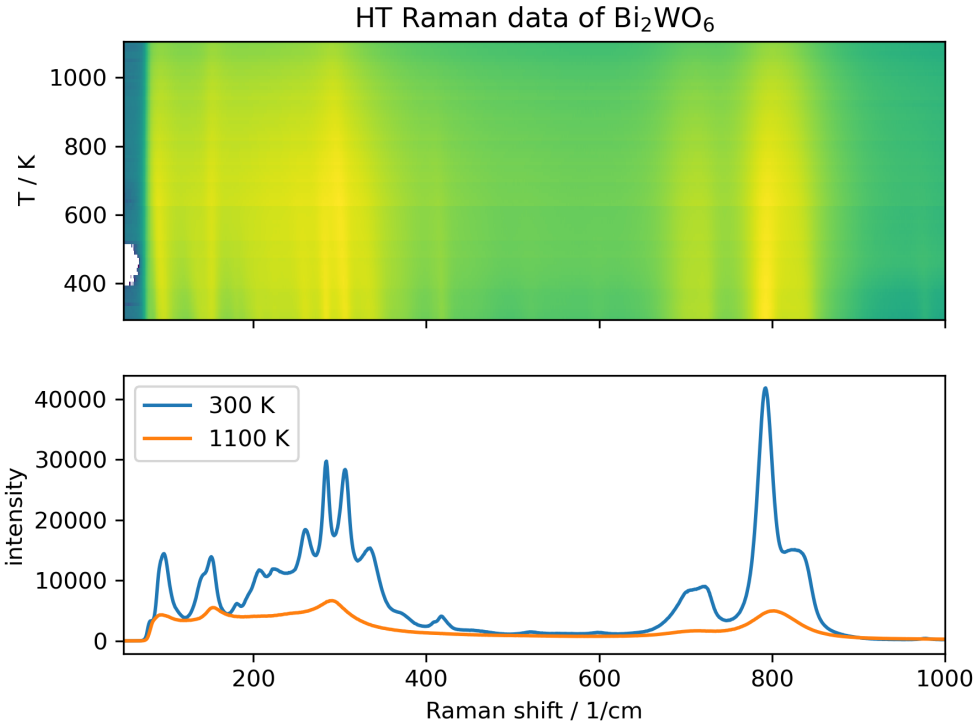

Figure 3.10: High-Temperature $BiWO_6$ Raman spectra

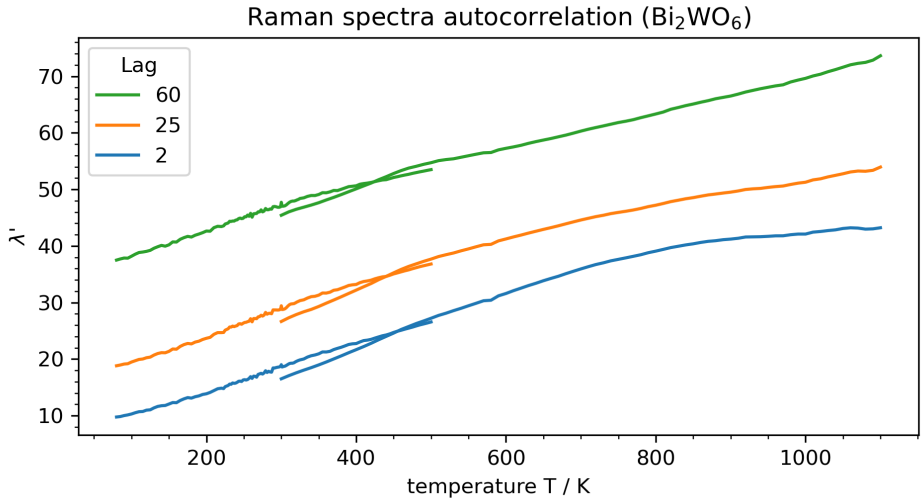

Figure 3.11: Autocorrelation of the $BiWO_6$ Raman spectra

can be seen in all curves. In the low and medium lag a gradual slope change happens to about 960 K, where an inflection seems to exist. Finally, at 1060 K another small dip is visible for all curves.

The temperatures are in line with some effects discussed above, however, only few features are apparent.

The signals in the collected Raman spectra were deconvoluted by peak fitting. Figure 3.12 shows the temperature dependent behavior of selected modes. The mode assignment of the Raman spectra is based on the reports by Maczka, Hanuza et al. [59, 156]

Most modes show softening with increasing temperatures with two exceptions. Firstly, the mode (3) is related to a translational mode of the bismuth lattice along the stacking direction and shows virtually no change of peak position over the whole temperature range. Mączka, Macalik and Kojima also noted this thermal stability and deduced a low anharmonicity of this mode. [59] Secondly, mode (18) shows hardening with increasing temperature. It is related to the symmetric WO-stretching vibration of apical oxygen atoms connected to the bismuth layer. The hardening implies an increase in bond strength or shortening of bond length with temperature. The WO-bond to apical oxygen O6-3 in Figure 3.4 actually shows such a bond length decrease.

With regard to temperature changes in selected modes some example will be discussed.

At low temperatures around 250 K the modes at low wavenumbers (1) to (5), except for the rigid mode (3), show a small discontinuity in the peakwidth as well as in intensity development, except for the rigid mode. Modes (1), (2), and (4) are related to a bismuth displacement along the stacking direction which was identified by Hirose, Kawaminami and Obara to be the reason for the permittivity spike the found. Around 300 K we observe changes in the broadening also for the high-wavenumber asymmetric WO vibrations

Above 500 K, for several modes the peak width increases drastically and hit the bound set in the fitting routine. This abrupt change in broadening behavior is in line with the prominent slope change in the autocorrelation. The increasing peak overlap lead to an increased difficulty to separate neighboring peaks. Broadness and intensity of individual peaks thus get more and more correlated with each other and therefore the parameters of overlapping peaks. The loss of clearly separated features also increases the correlation with the "background" subtraction, which in the first place also models all non-separable elements of the spectrum.

Another two critical points become apparent in the Raman spectra at around 700 K and 800 K, where several peaks become indistinguishable. The results from Mączka, Macalik and Kojima show this behavior, too, however it is not commented on. [59] Especially Figure 2 in [59] suggest that from 500 K and 700 K on, several low wavenumber modes are not separable anymore. Figure 3 therein also shows two slope changes in the width of the 56 cm^{-1} mode. [59] The thermal behavior of modes at higher wavenumbers were not investigated in [59].

Notably though, there is no distinct feature at the reported phase transition tem-

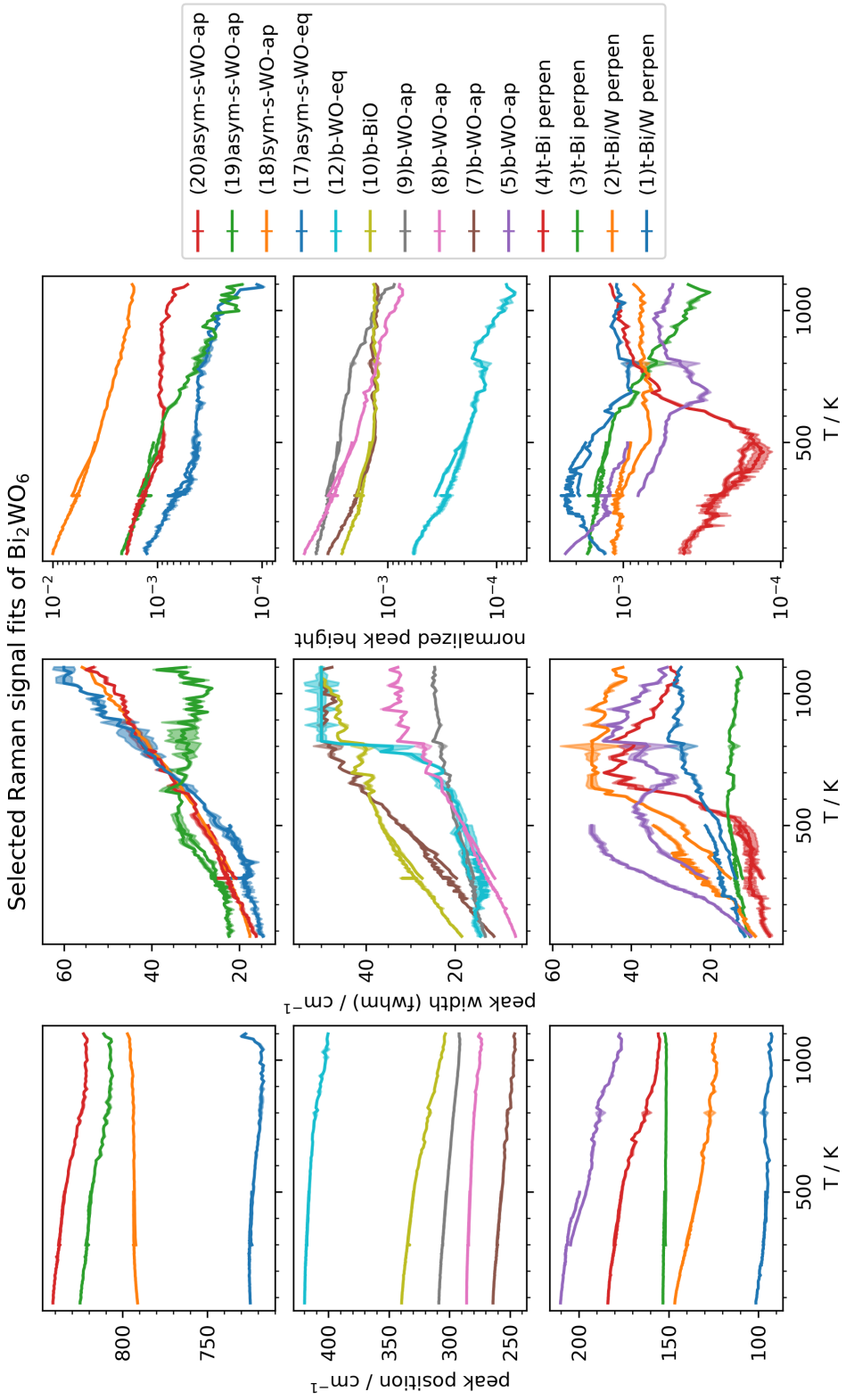

Figure 3.12: Selected modes from Raman peak fitting. Naming scheme: s - stretch, b - bending, t - translational, ap - apical oxygen, eq - equatorial oxygen.

perature. A possible explanation could be that the temperatures of the sample do not coincide with those the measurement device targets. The laser used in Raman spectroscopy introduces heat in the sample and laser damage is frequently encountered. As such, the local sample temperature might actually be higher due to heating by the laser. The recorded features around 700 K and 800 K actually could be related to the phase transition, however, this is just a hypothesis.

3.4 Thermoanalysis

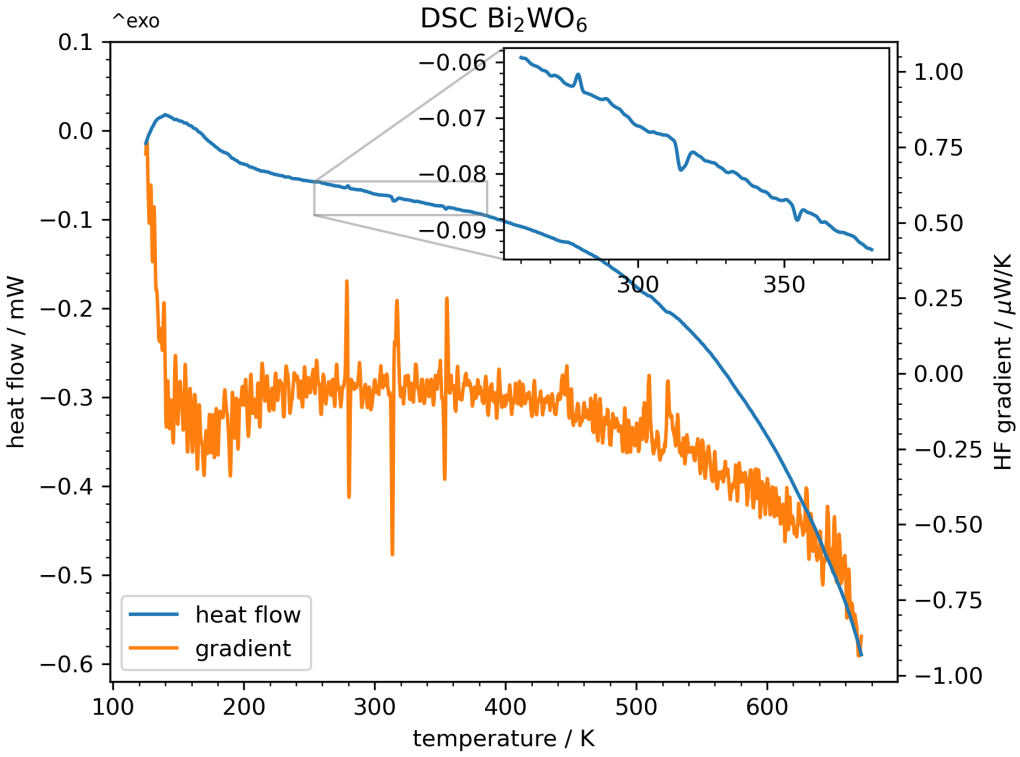

Figure 3.13: Heatflow data from DSC measurements on Bi_2WO_6 and the respective gradient. The central region with three small signals is magnified in the inset.

DSC measurements were performed for a continuous overview of the region around room temperature. The respective heatflow data are presented in Figure 3.13 along with the calculated gradient of the data series.

From the heatflow gradient the triad of three tiny signals at 280 K, 315 K and 355 K become apparent and are magnified in the inset. The first is exothermic and coincides exactly with onset of the reported dielectric in features in [45], while the second is endothermic at which the reported features again vanish. It is reasonable to assume these are related to the same effect of bismuth movement along c away

from the oxygen basal plane. [45]

Two small step signals at 445 K and 500 K also become visible in the heatflow gradient. They coincide with several parameter changes discussed above. Whether these are truly related needs to be further checked. The same holds for the broad signal at the low end of the temperature range which is tentatively attributed to an effect of the measurement device and procedure.

Even though no direct relationship can be deduced from these data, the similarities in occurrence are striking.

3.5 Conclusion

The results from Rietveld refinements and subsequent analysis of derived parameters are in general of limited significance due to the inaccuracy of the determined oxygen positions. General trends in parameters obtained from structure refinements show correlations to already reported features. However, the applicability of the ellipsoid analysis is severely limited due to the uncertainties in the oxygen positions and thus polyhedral coordination.

It has become clear that specific parameter derived from the refined atomic positions are susceptible to different critical points. Nonetheless, the changes and trends correlate strongly with effects visible in other techniques such as Raman spectroscopy and electric permittivity.

Also, the model free autocorrelation analysis clearly shows that these changes are not artifacts of a fitting or refinement process gone wrong, but are information contained in the data.

Poetically put: the data tells a story, we simply are not able to understand it (fully)(yet).

Our results confirm the LT phase transition at below 200 K described by Yoneda, Takeda and Tsurumi [44] and can tentatively pinpoint it to 150 K. Furthermore, our DSC results and interpretation of the reported permittivity data of Hirose, Kawaminami and Obara [45] suggest that there exists a series of subtle phase transition in the range from 280 K to 350 K. Two additional critical points at 500 K and 700 K could be identified. The literature known features appear in our results also at their reported temperatures and show significant impact on the studied parameters. It is thus reasonable to assume that the newly identified critical are a result of actual sample effects. Another finding is the distinctively different behavior of the two bismuth coordinations. Identification of single factors that are responsible for the observed effects however is hard. Some of our current results even contradict the interpretation in the literature that attribute certain effects for instance only to Bi. Usually multiple structural units and respective parameters of those cations are affected simultaneously and show changes at the critical points, although to more or less extent. As such, our result suggest that it is especially the interplay between the chemically and structurally distinct layers that is the underlying working principle. The precise structural interpretation, however, needs more reliable atomic position.

More sophisticated refinement techniques could partially mitigate the problem of scattering contrast. In the refinements presented here, only restriction on minimum bond lengths were imposed on the system. A related technique also taking too long bond length into account is based on the bond-valence sum of the coordination polyhedron as a boundary for the fitting. If a given BVS range has to be achieved, the bond lengths within the coordination polyhedra mutually limit themselves to prevent extreme values.

As the BVS is calculated from the bond length which are in turn calculated from the atomic positions the BVS presents a certain degree of abstraction from possibly unstable atomic positions. This was apparent above, since the step like features in the fractional coordinates did not propagate through these abstraction layers and the BVS showed rather smooth trends. However, as already mentioned above, the bond-valence theory is strictly only applicable to room-temperature structures since the r_0 and b parameter in Equation 2.1 are experimentally obtained from room-temperature datasets. Brown himself point out that bond lengths of high-temperature structures need a proper treatment to be comparable with RT parameter and that special electronic effects like the SOJTE need to be accounted for. [7, 157]

For our Rietveld refinements no change in symmetry was assumed. This factor that has to be critically assessed in future studies based on the current results. Given the hints for positional disorder, especially for bismuth, a refinement with split but occupationally restrained position or doubled unit cells could give further insights, whether there is a change of symmetry in the system.

Some parameters of the ellipsoid analysis have not been addressed in here for reasons of the limited data basis, but could become valuable if this circumstance changes. For instance the ellipsoid orientation, i.e. the direction of the ellipsoids radii vectors with respect to the crystallographic axes, offers convenient proxy-parameters for the octahedral tilting Often the tilting is gauged by the angles of polyhedral edges related to crystallographic axes or each other. However, these angles of the polyhedral edges may be affected by changes in the ligand perimeter itself, especially in case of SOJTE distorted polyhedra with pronounced off-centering.

Lifting of some limitations in the *pieface* software package used for the MBE calculations could offer additional insights into the structural behavior. For instance, the analysis of the full BiO_8 antiprism is currently limited by inability to address specific symmetry-equivalent atoms as mentioned above. Additionally, the irregular cuboctahedral void within the perosvskite slab of $Bi_2W_2O_9$ is of interest, since its volume and shape is determined by the tilting of the WO-octahedra. In this case the analysis of its maximal inscribing ellipsoid, that is the largest ellipsoid fitting within a set of points, is more desirable as its center and smallest radius correspond to the position and radius of potential A-site cations. The *pieface* software package would benefit from respective extensions.

The multiple indications of subtle changes in the local coordination found in this study and the corresponding literature makes it worth to reinvestigate the systems. Temperature-dependent neutron and high-resolution synchrotron diffraction, for accurate oxygen positions and more details on the local range from PDF analysis

are recommended for further studies. For Bi_2WO_6 two such HT studies have been performed already, however, with rather widely spaced temperature steps in the intermediate range between 300 K to 800 K. [34, 43]

With the knowledge gained from the here presented experiments one is able to develop an effective measurement plan and address the specific temperatures ranges of interest in more detail.

4 Synthesis and Structure of Ruddlesden-Popper-type $H_2W_2O_7$

4.1 Formation and Morphology

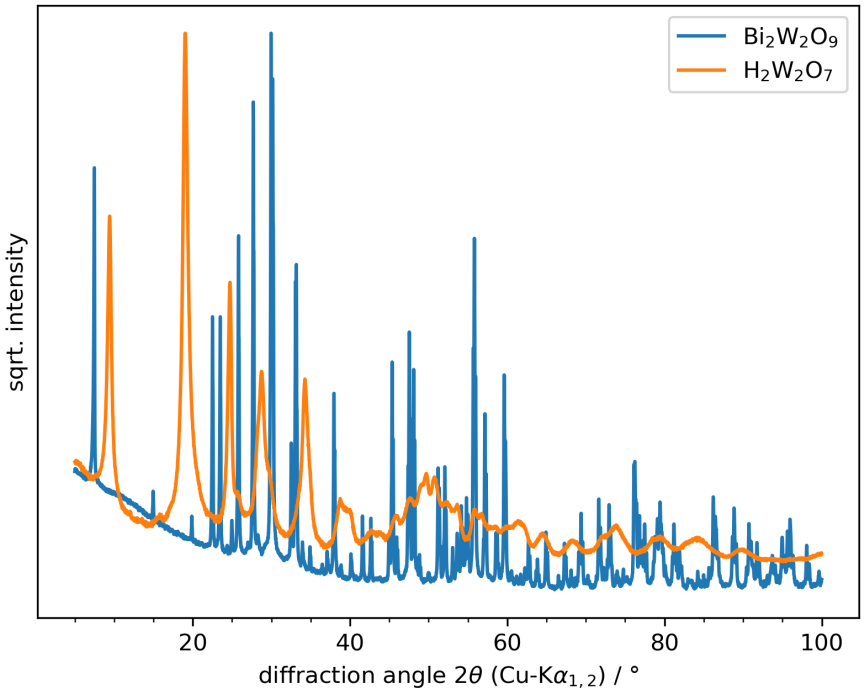

Figure 4.1: XPD pattern of the educt $Bi_2W_2O_9$ and product $H_2W_2O_7$ of the leaching synthesis.

When comparing the in-house XPD pattern of the parent $Bi_2W_2O_9$ before leaching and resulting $H_2W_2O_7$ in Figure 4.1 two key features can be recognized. The sharp reflections in the educt material, indicating a large mean crystallite size, have evolved to broad features in the product. Additionally, the first signal, attributed to the (002) reflection, has visibly shifted as a result of the smaller unit cell. Without the bismuth interlayer the spacing between the perovskite layers reduces.

Attempts on a structure solution for $H_2W_2O_7$ from this data alone quickly revealed to be futile. Indexing of the few reflections provided no definitive candidate for a suitable space group. The data quality allowed for no further knowledge to be gained in addition to already reported features.

The combination of the apparent low crystallinity of the sample and the low X-ray scattering contribution of oxygen compared to the heavy metal prevented a meaningful description of the assumed octahedral network. To overcome these limitations, additional powder diffraction measurements were performed with neutron radiation on deuterated samples, which is covered in section 4.3.

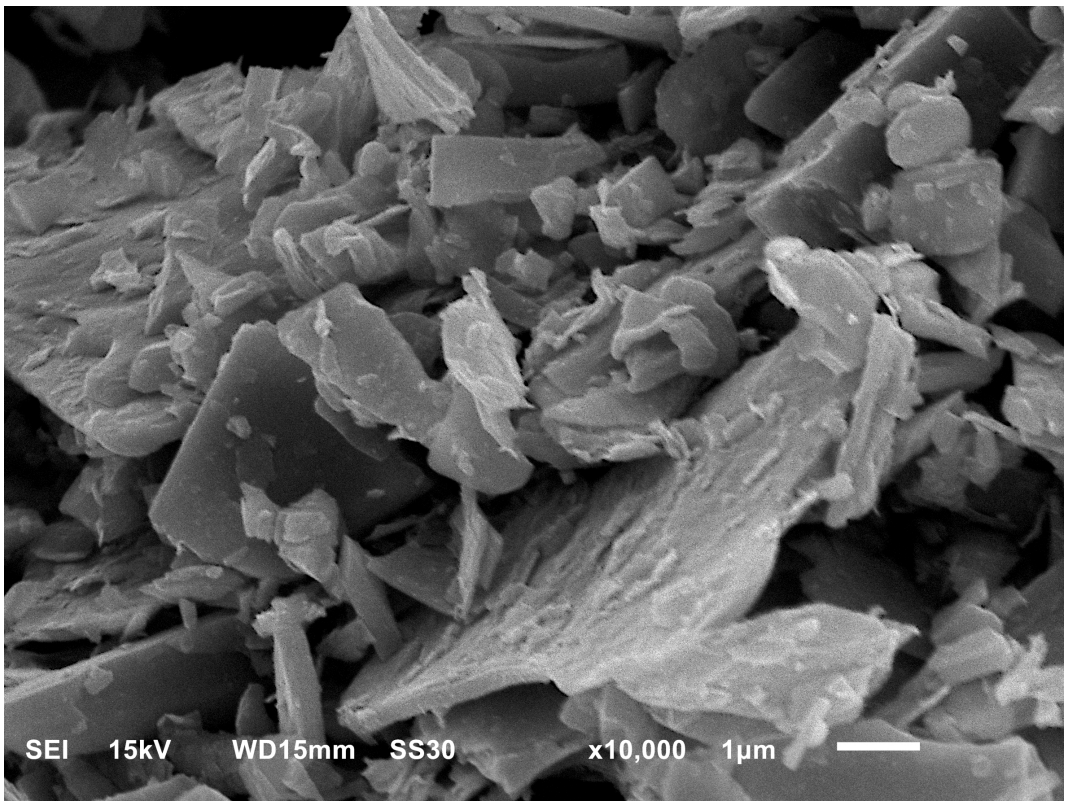

Figure 4.2: SEM micrograph of $H_2W_2O_7$ particles obtained from leaching synthesis showing highly anisotropic platelet-like shapes and signs of further delamination.

The leaching leads to strongly anisotropic, platelet-like particles as can be seen from the SEM micrographs in Figure 4.2. Notably, these show signs of delamination on the platelet surfaces. The distribution of apparent particle sizes is quite broad. There are large platelets up to a few µm in lateral extent and sub µm in thickness. Also, small fragments with sizes <100 nm are visible at higher magnifications.

The low crystallite size of the product can be attributed to the introduction of defects and disorder. The TEM micrographs in Figure 4.3 show typical defect motifs. They involve rotation of layers as indicated by the different direction of the square

grids in Figure 4.3a. These grids are formed by the lattice fringes of the checkerboard arrangement of octahedra typical for perovskite-like structures. Additionally, modulations in the form of Moiré-patterns are visibleFigure 4.3b, i.e. alternating regions of clearly visible lattice fringes and region of low contrast. This contrast modulation is a result of local structural incoherence. Possible lateral and vertical sources are, for instance, incommensurately rotated layers or slight buckling/wrinkling, respectively.

The layered nature becomes even more apparent from the side view of a particle depicted in Figure 4.3c. For this purpose a platelet was cut in the respective direction by focus ion beam (FIB) preparation. The lower half of Figure 4.3c shows a regular arrangement of individual layers whose double octahedral nature is clearly discernible.

The upper part shows typical defect motifs that can be expected from layered materials. Close to the top of the image the aforementioned buckling or wrinkling of partially delaminated layers is apparent. At the image center a larger split is visible which ends in stacking fault which appears to be a locally confined stack of three octahedra.

In Figure 4.3d a side view of a region closer to the particle edge is depicted. Here, the stacking is severely distorted and patches of ordered arrangements are only found locally.

4.2 Spectroscopic characterization of hydrogen environment

^{1}H MAS NMR spectroscopy was performed to get further information on the number of individual hydrogen positions and their environment. The main region of the obtained spectrum is shown in Figure 4.4, additional sidebands at distances in integers of the spinning frequency are not shown. Visual inspection and fitting with pseudo-Voigt profiles reveals at least two distinct signals, however adding a third profile yields a significant better fit quality and reduces the χ^2 value from about 30 to 8.

The broadness of the signals in ^{1}H solid-state NMR is usually caused by anisotropic interactions, such as dipolar coupling or chemical shift anisotropy. [158] These are usually reduced or suppressed, respectively, by the MAS technique but even the high spinning rate of 40kHz does not separate the broad features into narrower contributions. In other layered perovskites even with medium spinning rates additional features are distinguishable. [159] This indicates strong dipolar coupling between the protons, which is consistent with their expected close proximity within the coordinated water molecule. An additional reason for apparent line broadening can be chemical shift dispersion by local disorder. [160] Minor differences in the local environment of the nucleus cause a range of isotropic signals to appear close to each other and overlap, resulting in a broadened signal. In case of this layered compound, such differences could be slight variance in the distances between or small shifts of the layers. This is comparable to XRD, where disorder in form of small variances

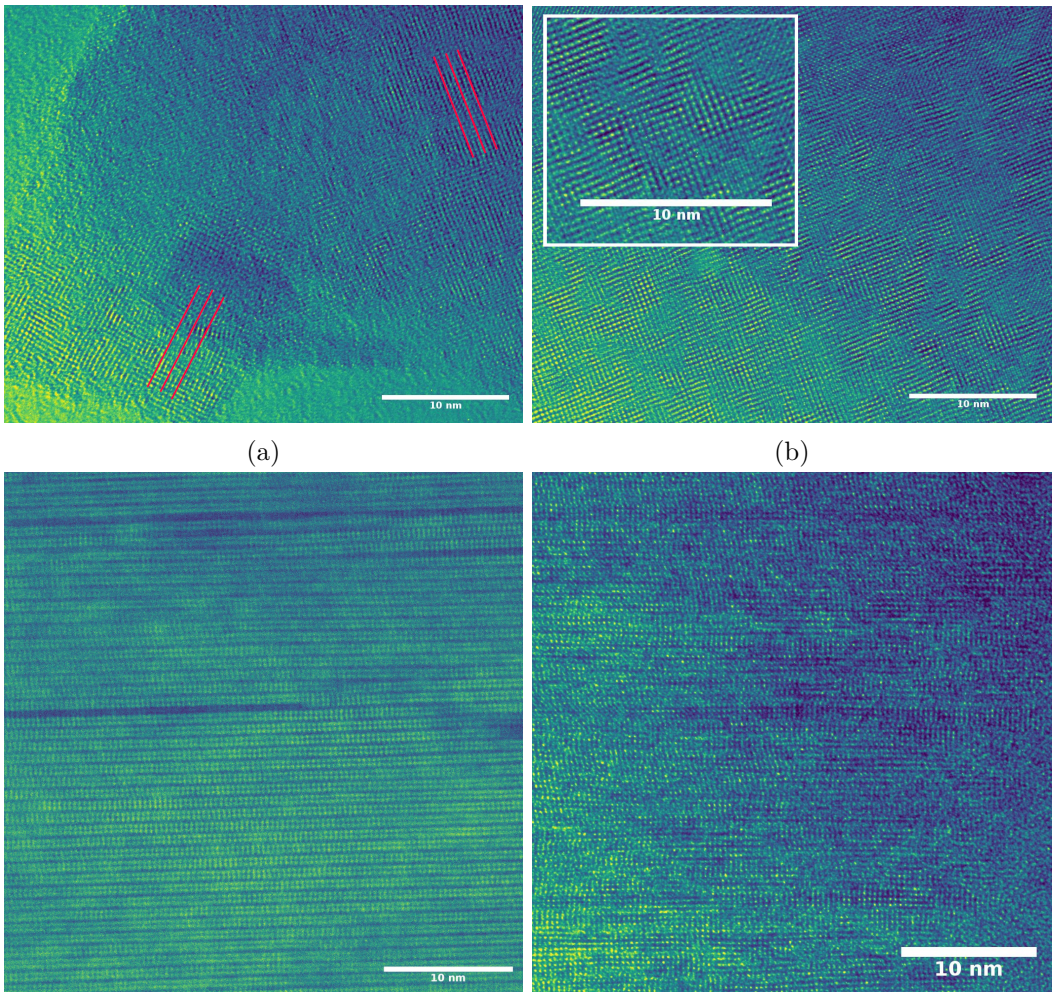

(a) (b)

(c) (d)

Figure 4.3: TEM micrographs of different defect themes. (a) Rotation of individual layers against each other with direction of lattices fringes indicated by red lines (particle top view). (b) Modulation in form of Moiré-patterns (particle top view). (c) Regions of consistent double layer stacking together with delamination and layer steps (particle side view, particle center). (d) Severely disordered regions with pronounced layer condensation (particle side view, towards edge)

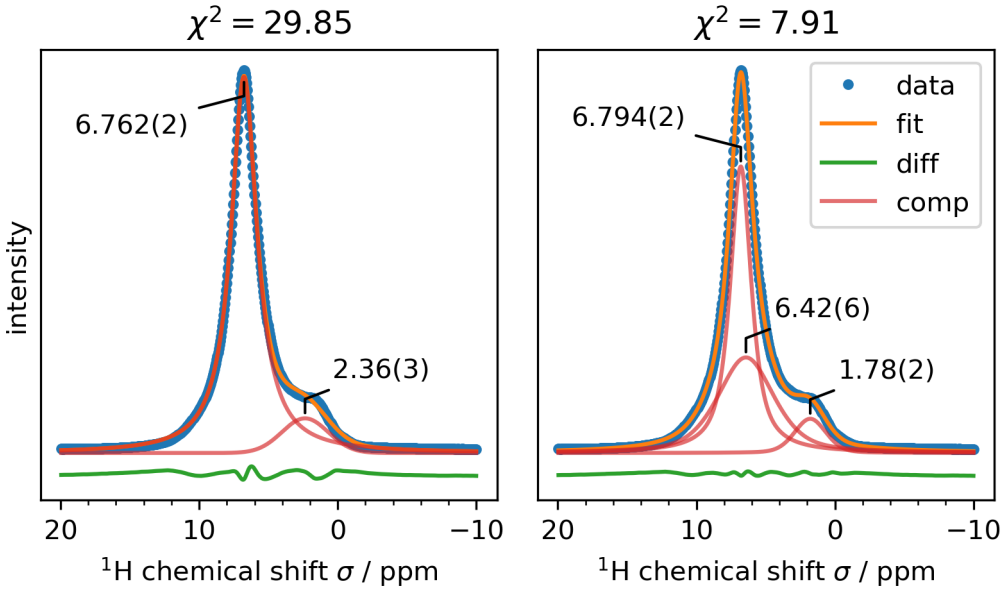

Figure 4.4: ^{1}H magic-angle spinning (MAS) NMR Hahn-echo spectrum of the hydrotungstate and respective fits with pseudo-Voigt functions. The strong signals at 6.7 ppm and 6.4 ppm are attributed to the hydrogen atoms in the structural water. The high-field signal at 1.8 ppm is attributed to OH species in the form of surface hydroxyl groups or at defect sites.

in the d-spacing of diffracting planes cause the reflection's linewidth to increase via micro-strain broadening. The data does not allow to distinguish between these effects. In principle, the strong $^1H-^1H$ dipolar coupling could be overcome by even higher spinning rates or stronger magnetic fields but also higher temperatures to increase the proton dynamics. [161]

Following the interpretation of Nogueira et al., the strong signals at 6.7 ppm and 6.4 ppm are attributed to the hydrogen atoms in the structural water. [121] The presence of two, slightly shifted signals indicates two distinct proton positions with similar but slightly different environments. The high-field signal at 1.8 ppm is attributed to OH species in the form of surface hydroxyl groups or at defect sites. The latter could include amorphous regions where protons bind to oxygen sites in a random fashion. Another possibility is the binding of two single protons to both apical oxygen atoms on either side of the double octahedra columns.

Additional water in the interlayer space and the associated hydrogen bonds are presumed to appear in an intermediate range similar to other studies on hydrated perovskites. [161] As no such signals could be observed here, irreversibility of the dehydration step at 393 K is likely.

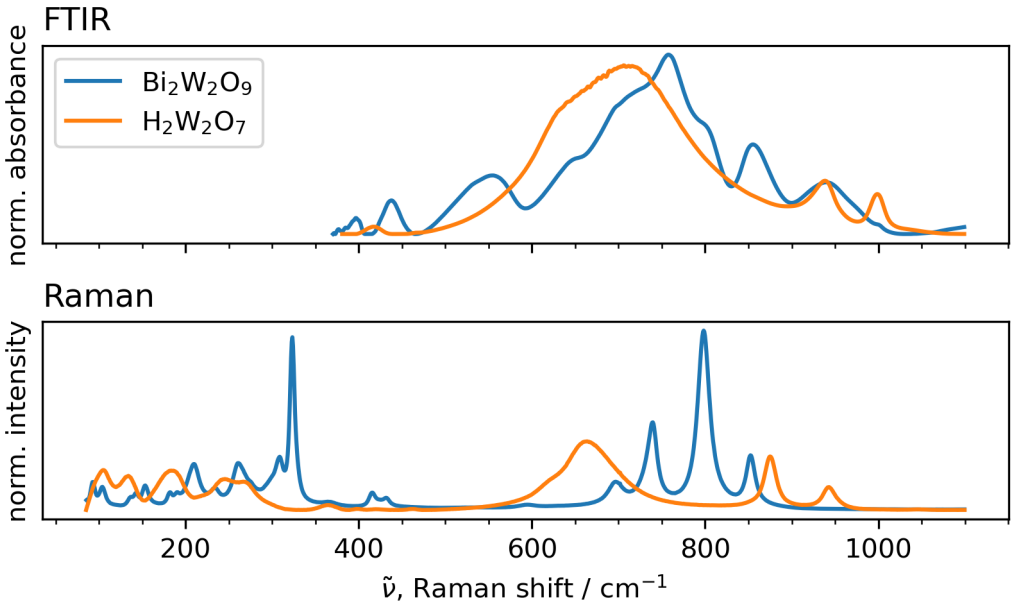

Figure 4.5: Comparison of FTIR and Raman spectra of $H_2W_2O_7$ and $Bi_2W_2O_9$ up to 1100 cm^{-1} showing major differences in the peak positions between 600 cm^{-1} and 800 cm^{-1}. Signals attributed to the BiO vibrations in the range below 500 cm^{-1} are gone after the leaching.

In Figure 4.5 the FTIR and Raman spectra of $H_2W_2O_7$ up to 1100 cm^{-1} are shown. After the leaching the Raman signals attributed to the BiO vibrations

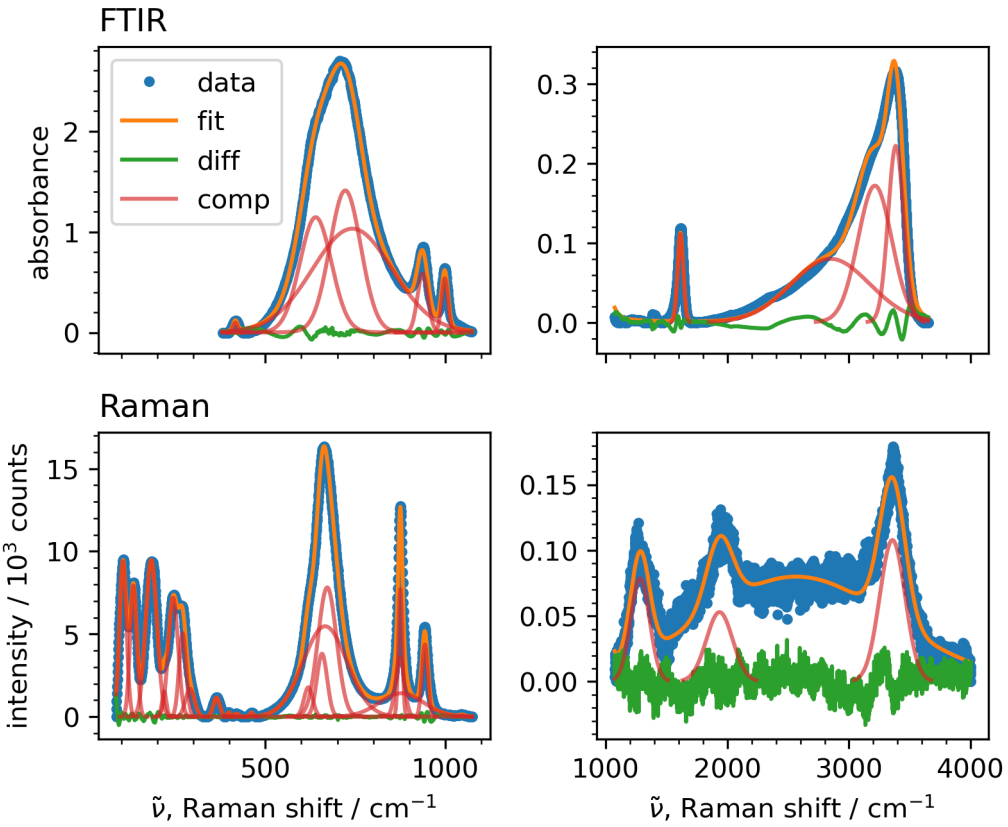

Figure 4.6: Fit of FTIR and Raman spectra of $H_2W_2O_7$

Table 4.1: Spectroscopic mode assignment of $H_2W_2O_7$ and comparison with the parent BiW_2O_9, the single layer hydrotungstate H_2WO_4 and WO_3.

	$H_2W_2O_7$		$Bi_2W_2O_9$[162]		H_2WO_4[84]		WO_3[84]	
Assignment	IR	Ra	IR	Ra	IR	Ra	IR	Ra
ν(OH)	3386.2(7)	3357(4)			3390			
	3218(7)				3170			
	2863(23)							
unassigned		1936(8)						
σ(OH)	1615.3(6)				1620			
unassigned		1283(5)						
ν(W=O)	998.8(1)	1047(2)			948	948		
ν(W=O−W)	937.1(1)	943.5(1)	936					
ν(O−W−O)		878.5(4)						
		875.4(1)	855	851			870	
		874.2(1)						
			799	799			815	807
			759	739				
	740.9(8)				730		755	715
	721.0(7)		709	699				
		672(3)	647		680			
		666.1(2)					665	
	638.7(9)	657.5(8)				645		
		619(1)						
Overtone or combination			550					
σ(W−O−W)		461.6(4)	435	431				434
H_2O librations	416.6(4)	420.1(6)			420			
ν(W−OH_2), H_2O librations		398.8(4)			370	377	380	
		364.2(2)			330		330	327
σ(W−O−W)		290(2)			270		280	273
ν(W−O−W)		269.8(2)				253		
		243.8(3)						
		218.7(2)				235	225	218
lattice modes		182.9(1)				192		187
		133.1(1)				150		134
		104.2(1)				90		93

in the range below $500\,cm^{-1}$ are gone which is most prominently visible by the missing BiO stretching vibration at $325\,cm^{-1}$. Furthermore, in the region of the WO stretching vibrations around $800\,cm^{-1}$ the signals appear at lower and higher wavenumbers. The higher-wavenumber features can be attributed to the presence of W=O double bonds in the long-bond-short-bond motif also known from the single layer hydrotungstate H_2WO_4. Signals of the structural water in $H_2W_2O_7$ are located above $1100\,cm^{-1}$ as shown in Figure 4.6 together with the results of the peak fitting. The respective spectral assignments are given in Table 4.1.

The low-intensity signal at $1400\,cm^{-1}$ indicate trace amounts of surface adsorbed water. Bending vibrations in the structural water lead to the signal at $1650\,cm^{-1}$. The region of OH stretch vibration around $3000\,cm^{-1}$ can be described by three signals in FTIR and a single peak in the Raman spectrum. Interpretation of the Raman signal is difficult due to its low SNR, however, the FTIR signals can be attributed to OH groups in different hydrogen bonding environments.

The spectra and peak positions are very similar to other reported hydrated tungstates and particular the single layer compound H_2WO_4. [84] In terms of the proton environment, the double-layer and single-layer compound are highly comparable. However, the results are not definitive and ambiguous interpretations regarding disorder motifs in the interlayer and the hydrogen bonding are possible.

The deuterated sample for neutron diffraction was also investigated with FTIR in order to study the proton-deuterium exchange behavior. We noticed a spoilage of the deuterated samples with protium, whose implications are discussed further below in section 4.3.

Figure 4.7 shows the region of H_2O and D_2O bending vibration from $1250\,cm^{-1}$ to $1700\,cm^{-1}$. Over the course of one hour the D_2O signal vanishes almost completely while the H_2O gains in intensity. This shows a rapid exchange of deuterium with protium upon contact with atmospheric moisture. However, since ATR is a surface sensitive technique these results not necessarily represent the bulk behavior. The H_2O signal is quite strong to begin with, due to a leakage in the storage container. A full exchange, however, did not take place even though the sample was kept in the leaky environment for about a week before the spoilage was noticed and the presented ATR experiments were performed. The presence of interlayer water as a prerequisite for rapid proton insertion was identified in [87]. Since the compound was dried beforehand and is thus deprived of the interlayer water the exchange rates in to the bulk may actually be lower.

4.3 Comparison of different structure model candidates

The investigations on the atomic structure of the hydrotungstate are based on classical approaches for solving structure from powder diffraction data including the previous knowledge of the structural features from spectroscopic investigations and the TEM micrographs.

The compound was probed for non-linear optical properties, i.e. SHG to poten-

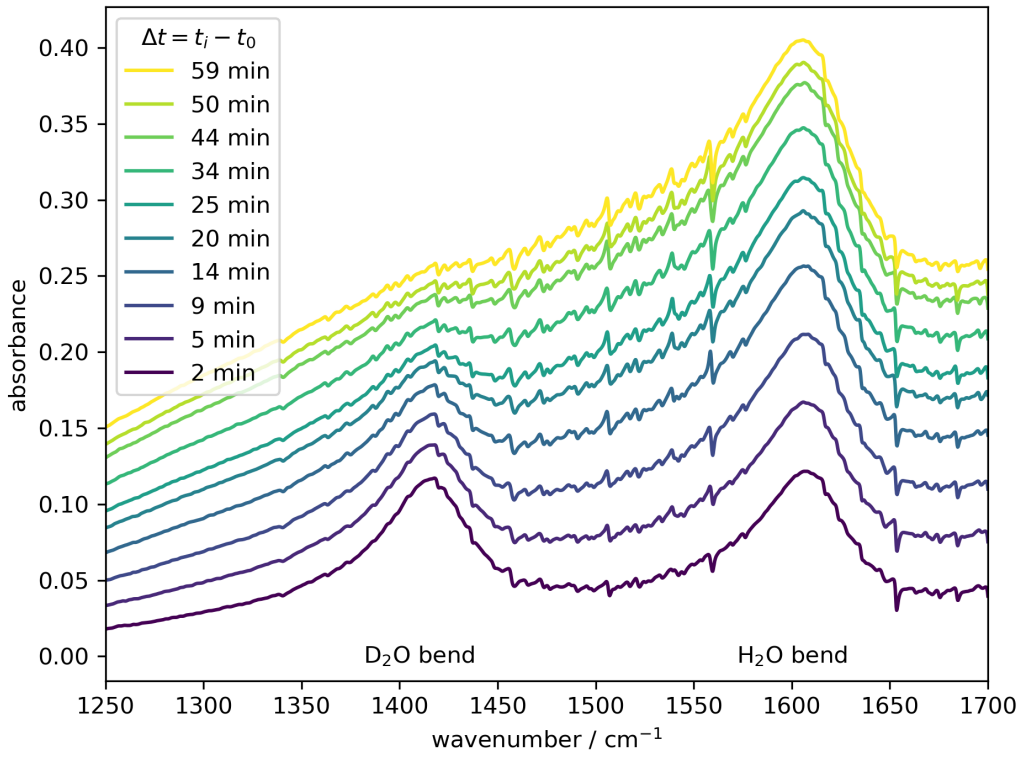

Figure 4.7: Time-dependent ATR infrared spectroscopy measurement series of deuterated hydrotungstate. Upon contact with atmospheric water the intensity of the D_2O-bending signal vanishes almost completely over the course of one hour.

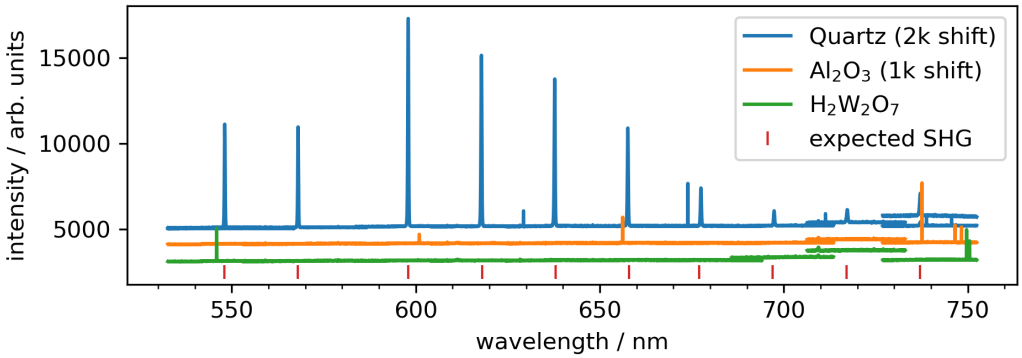

Figure 4.8: SHG response of $H_2W_2O_7$ in comparison to Quartz and Al_2O_3 as positive and negative references, respectively. Only some noise signals and no intensities at the expected wavelengths could be detected, thus centrosymmetry can not be excluded.

tially rule out centrosymmetric structure model candidates. Absence of an inversion center is a prerequisite for SHG, so any related intensity is a strong evidence for a non-centrosymmetric structure. [163] However, no intensities at doubled frequencies were found, as can be seen in Figure 4.8, hence centrosymmetric space groups could not be excluded and were considered as viable options.

Reproducing the attempts by Kudo, Ohkawa et al., the structure of the parent $Bi_2W_2O_9$ in space group $Pna2_1$ served as a starting point. [91] The assignment of space group $Pnab$ as the symmetry of the parent $Bi_2W_2O_9$ is fairly recent and the results in this section do not reflect this development. The below presented trials of the different structure models were performed before the report of the apparent higher symmetry became known to the author. The author deemed a retroactive inclusion of a model in $Pnab$ would not provide a significant merit given the findings of our other structural investigations.

Starting from the $Bi_2W_2O_9$ model in space group $Pna2_1$, the cell dimension were adjusted based on the retrieved values from a Pawley refinement in this space group and the bismuth oxide interlayer was removed while keeping the tungsten oxide arrangement intact. Additional orthorhombic space groups with comparable cell dimensions were sought via an indexing of the few reflections in the X-ray diffraction pattern. Models that exhibit the structural features based on our previous knowledge, such as the perovskitic resemblance of individual and the shift between adjacent layers, could be constructed in the space groups $P222$ and $P222_1$. Additionally, a model was constructed in the space group $Pnam$, a supergroup to $Pna2_1$.

Subsequent Rietveld refinements of these models against the X-ray diffraction data resulted in structures which were characterized by generally highly deformed octahedra with too close O-O and W-O proximity. Application of anti-bump distance and angle restraints to prevent unphysical oxygen positions tended to run into the set limits. Presumably, the calculation favored the unphysical arrangements to account for the disorder in the sample. The low scattering contributions of oxygen and resulting lack of information contained in the in-house X-ray data prevented a more robust refinement. Furthermore, information on hydrogen atoms were also completely missing.

Thus, experiments using neutron radiation were performed to mitigate the problems of the low scattering power and to later on refine the structure models simultaneously against the X-ray and neutron datasets.

The synthesis route was adapted to produce a deuterated sample and the experimental procedures were carried out applying Schlenk-techniques. While the leaching and washing itself was straightforward, the subsequent drying, handling and packaging of the deuterated sample was a likely source of errors. Especially the low evaporation rates of the heavy water lead to difficulties in an effective removal without risking the degradation of the fragile hydrotungstate sample. Ideally the whole procedure would have been performed in a glove box, but "wet" glove boxes where water containing samples can be processed were not available.

Despite the applied measures, the sample was nonetheless spoiled with protium. It is presumed to stem from atmospheric water leaking into the storage container.

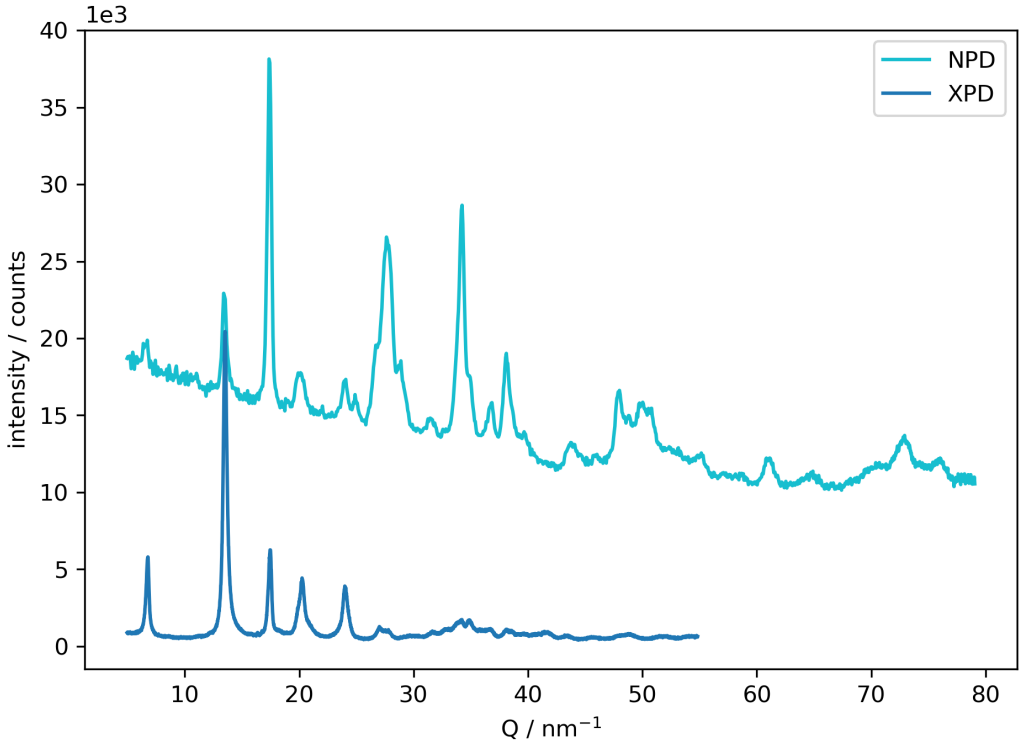

Figure 4.9: Neutron and X-ray powder diffraction patterns. Note that the neutron dataset is not shifted, the high background is the result of incoherent scattering from protium.

The unfortunate spoilage of the deuterated sample had some implications for the course of the project. It affected the quality of the data from neutron powder diffraction. The exchange of deuterium with protium resulted in a less effective usage of the neutron radiation due to loss of intensity in the incoherent scattering not contributing to the structure solution. This resulted in a high incoherent scattering background, as can be seen in Figure 4.9.

On the other hand, the spoilage incidentally opened the possibility to extend the direction of the NMR investigations to also include heteronuclear experiments. However, the preliminary results did not add significantly to the structure solution and a more thorough investigation was beyond the possibilities of the project.

Even with the additional information from the neutron experiments it became clear that due to the amount of defects and disorder in the produced sample it would be difficult to find a singular solution model that would describe the diffraction pattern satisfactorily. This shifted the aim of the investigations towards trials of the different specific structural motifs imposed by the space group symmetries and elaborating their plausibility, especially concerning the hydrogen environment.

Table 4.2: Selected agreement factors for different models from combined refinements.

		Rietveld					Pawley				
SG		$\#_P$	R_{wp}	R_{wp}'	wDW	GOF	$\#_P$	R_{wp}	R_{wp}'	wDW	GOF
	Co	56	9.5	27.5	0.176	6.1	751	5.1	16.2	0.500	3.5
$Pna2_1$	N		5.4	25.7	0.113	6.4		3.4	20.7	0.256	5.1
	X		18.1	28.2	0.063	6.0		9.1	14.6	0.244	3.1
	Co	52	9.4	26.7	0.175	6.0	937	3.9	12.0	1.043	2.7
$P222$	N		5.4	25.9	0.110	6.4		1.8	9.8	0.714	2.8
	X		17.9	27.0	0.065	5.9		7.8	12.6	0.328	2.7
	Co	55	9.0	26.6	0.215	5.8	923	3.9	12.3	1.025	2.7
$P222_1$	N		4.8	24.1	0.148	5.7		1.8	11.0	0.694	2.8
	X		17.5	27.4	0.067	5.8		7.8	12.7	0.331	2.7
	Co	45	9.9	30.4	0.180	6.4	750	5.0	16.2	0.495	3.4
$Pnam$	N		5.0	26.6	0.127	5.9		3.4	22.4	0.243	5.0
	X		19.8	31.6	0.053	6.5		8.9	14.4	0.252	3.0
	Co	52	7.4	24.1	0.248	4.8					
$Pnam$*	N		4.4	26.2	0.146	5.2					
	X		14.1	23.5	0.103	4.7					
	Co	57	6.3	18.0	0.376	4.0	1432	3.3	9.3	1.519	2.4
$P2_1/n$	N		3.4	16.6	0.240	4.0		1.3	6.7	1.087	2.9
	X		12.2	18.5	0.137	4.1		6.8	10.0	0.432	2.3

$\#_P$ is the number of refinement parameters
Co, X, N denotes combined, X-ray and neutron component
* with refined B_{eq} values

While preparing our results, Wang, Sun et al. reported on their structural investigations on the same compound. [96] Using DFT calculations they produced a structure model in space group $P2_1/n$ which they validated against X-ray diffraction data of their sample. This structure model was included retroactively in this study, both as combined-refined to our dataset and as published (denoted with §).

For all the selected space groups two refinements were performed, a Rietveld refinement of the prepared atomic structure model and a Pawley refinement of just the unit cell.

The agreement factors and number of fitted parameters are summarized in Table 4.2. R_{wp} is the weighted, integrated intensity scaled sum of residuals. R_{wp}' additionally accounts for the calculated background intensity in the scaling. This mitigates the unwanted effect of well-fitted background intensity dominating the R_{wp}. The effect of the background can especially be seen when comparing the two residual para-

meters of the neutron and X-ray partials, where in case of the neutron data the fitting of the high incoherent scattering background leads to deceptively small R_{wp} values. The GOF = $\sqrt{\frac{\chi^2}{\text{degrees of freedom}}}$ or regression standard error factors in the number of refined parameters. For all of those parameters low values represent a better agreement of model and experiment. The weighted Durbin-Watson parameter wDW represents the autocorrelation between the residuals of adjacent data points and is an indicator for underlying nature of the residuals. The low values indicate a fairly strong positive autocorrelation, which characterizes a mismatch between model and experiment. For comparison, purely statistical noise would also lead to high residuals in general, however, the wDW in this case would show a value close to 2 indicating low autocorrelation of the residuals.

For further details on the different agreement factors the reader is referred to the TOPAS software technical reference.

For the models in space groups $Pna2_1$, $P222$ and $P222_1$ there are no significant differences in the quality of the fit. The model in $Pnam$ has a minor decrease in agreement but also with a reduced number of parameters. However, the GOF is still slightly worse compared to the previous models. Upon additional refinement of the isotropic atomic displacement parameter B_{eq} values the fit improves drastically. The model in $P2_1/n$ clearly shows the greatest accordance to the experimental data. The R_{wp}' values are the lowest of all studied models. Also the wDW values are better than in the other refinements showing a reduction of the correlative mismatch. Although the model has the highest albeit not far off number of refined parameters, according to the GOF the increased degrees of freedom are justified by the superior description of the experimental data.

For the Pawley refinements the agreement factors correlate closely with the number of fitting parameters. The Pawley refinements show better agreement between calculated and experimental data, which is generally the case. The intensity of the reflections is decoupled from the scattering contributions of the constituents and each reflection's intensity is refined individually. As such, the number of fitting parameters is massively increased.

This gets especially problematic with this sample, as the diffraction patterns exhibit only a small number of broadened and overlapping reflections. This absence of distinct features in combination with a high number of fitting parameters allows for rather small residuals, which presumably even dominates the GOF. Arguably, the refined Pawley patterns here are actually overfitted impairing the significance of the obtained parameter values.

The lattice parameters from Rietveld and Pawley refinements are collected in Table 4.3.

In case of the Rietveld refinements the respective lattice parameters are highly similar between the different models. The values are the same within two and ten ESDs for the two short and the long lattice parameters, respectively.

In case of the Pawley refinements the values exhibit an additional significant digit, however, the discrepancies between the models are increased up to approximately

Table 4.3: Lattice parameters for different models from combined refinements.

SG		a/pm	b/pm	c/pm	γ/°
$Pna2_1$	Rietveld	513.54(15)	522.76(14)	1849.65(30)	
	Pawley	508.46(20)	527.16(22)	1850.6(4)	
$P222$	Rietveld	511.26(12)	523.49(15)	1849.72(30)	
	Pawley	508.68(22)	526.72(25)	1852.2(4)	
$P222_1$	Rietveld	513.26(13)	522.98(13)	1851.96(29)	
	Pawley	510.37(19)	525.25(20)	1853.5(4)	
$Pnam$	Rietveld	513.39(15)	522.24(14)	1849.65(30)	
	Pawley	512.16(21)	523.73(20)	1851.4(4)	
$Pnam$*		513.85(14)	523.56(12)	1854.26(30)	
$P2_1/n$	Rietveld	513.03(9)	523.32(9)	1852.69(20)	89.192(13)
	Pawley	512.60(25)	526.34(20)	1854.72(34)	88.871(29)

* with refined B_{eq} values

ten times the given ESDs for all parameters. Within the models the values of the two shorter lattice parameters show a larger absolute difference compared to the Rietveld refined values. For the long axis the values are comparable for both refinement types. However, these discrepancies are not considered to be a viable basis for interpretation due to the above-mentioned limited informative value of the experimental data with respect to the high number of fitting parameters.

The lattice parameters give no clear predication as to which model is superior as all show more or less consistent values with the idea of a Bi_2O_2-deprived $Bi_2W_2O_9$. From the agreement factors the model in space group $P2_1/n$ seems to perform best. However, the mere reproduction of the experimental data is not enough to validate a structure model. The actual atomic arrangement need to fulfill physical and chemical criteria to be considered meaningful.

To gauge the plausibility of the refined atomic structure models they were compared to each other as well as to known related compounds. The related compounds (RCs) are the parent $Bi_2W_2O_9$, the single layered H_2WO_4(using the model reported by Szymanski and Roberts [78]) and the three-dimensional WO_3. Detailed analyses and tabulated data for the individual structure types can be found further below.

The bond length distributions and mean bond lengths of the different polyhedra of all structures are plotted in Figure 4.10. The comprehensive bond length analysis for six-fold WO coordination from Gagné and Hawthorne is reproduced in the figure for reference. [164] The authors report a respective mean bond length of 195.1 pm, shown by the green line in the reference plot. [164] Generally, the different structures show diverse bond length distributions for their individual polyhedra. Some values lie well outside the reference distribution already indicating severe issues with regard

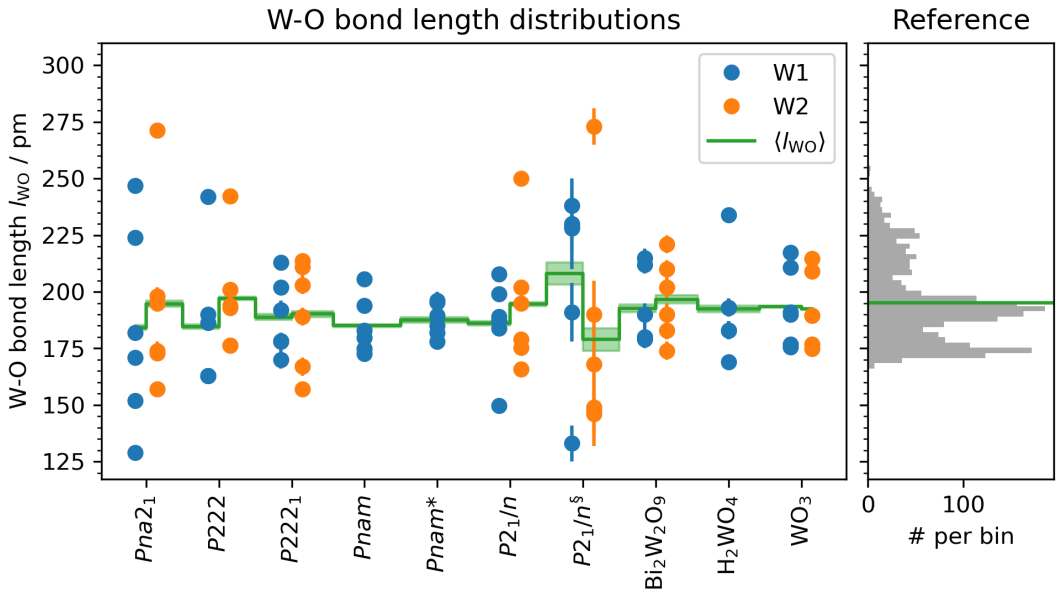

Figure 4.10: WO bond length distributions for the different structure models and reference structures. Additionally, the reference distribution of six-fold WO coordinations by Gagné and Hawthorne is reproduced for comparison. [164] Green lines corresponds to the average bond length of the refined and reference coordinations.

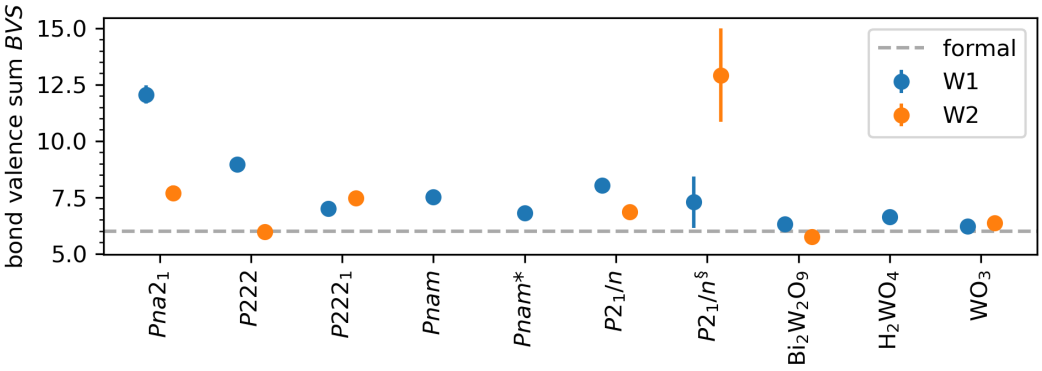

Figure 4.11: Bond valence sums of the WO coordinations in the different structure models. The expected formal valence of 6 v.u. is indicated by the dashed line.

to the meaningfulness of the respective refined models.

The comparison in Figure 4.11 shows the bond valence sums for all polyhedra. In all the refined structure models, except for the W2 polyhedron in spacegroup $P222$, the bond valence sum deviate significantly from the expected formal valence of 6 v.u. for the central tungsten atom. Notably, in the reported structure for single layer H_2WO_4 the BVS of 6.63(29) v.u. also deviates significantly from the formal value. However, Gagné and Hawthorne deem deviations of up to 7 %, i.e. 0.42 v.u. as acceptable for a structure verification, which overlaps with the uncertainty range. [164]

Additionally, two sets of geometrical parameters are visualized in Figure 4.12 to compare the polyhedral coordinations between different models and compounds. The respective values are listed in Table 4.4, Table 4.8, Table 4.15 and Table 4.20.

On one hand typical polyhedron parameters based directly on individual bond lengths $l_{WO}(i)$ and angles $\phi(i)$ were considered, such as polyhedral volume V_{poly}, average bond length $\langle l_{WO} \rangle$, bond length variance $\sigma^2(l_{WO})$, distortion index D, bond length distortion Δ, quadratic elongation $\langle \lambda \rangle$ and bond angle variance $\sigma^2(\phi)$.

On the other hand the parameters of the minimum bounding ellipsoid were analyzed, such as the ellipsoid volume V_{ellip}, average radius $\langle R \rangle$, radius variance $\sigma^2(R)$, the magnitude of the central atom dislocation from the ellipsoid center δ_{center} and the shape parameter S, which sign and magnitude describes a prolate (positive) or oblate (negative) distortion of the ellipsoid. For more details on the parameters see subsubsection 2.2.1.

Notably, the general features in the volume and mean bond length / radius parameters are highly similar for polyhedron and ellipsoid, indicating a close representation of the former by the latter. Also, the parameters bond length / radius variances $\sigma^2(l_{WO})$ and $\sigma^2(R)$, both distortion indices D and Δ as well as central atom dislocation δ_{center} in general seem to be fairly high correlated with only small deviations within individual structure models. The quadratic elongation shows analogous trends compared to the other parameter but with different relative mag-

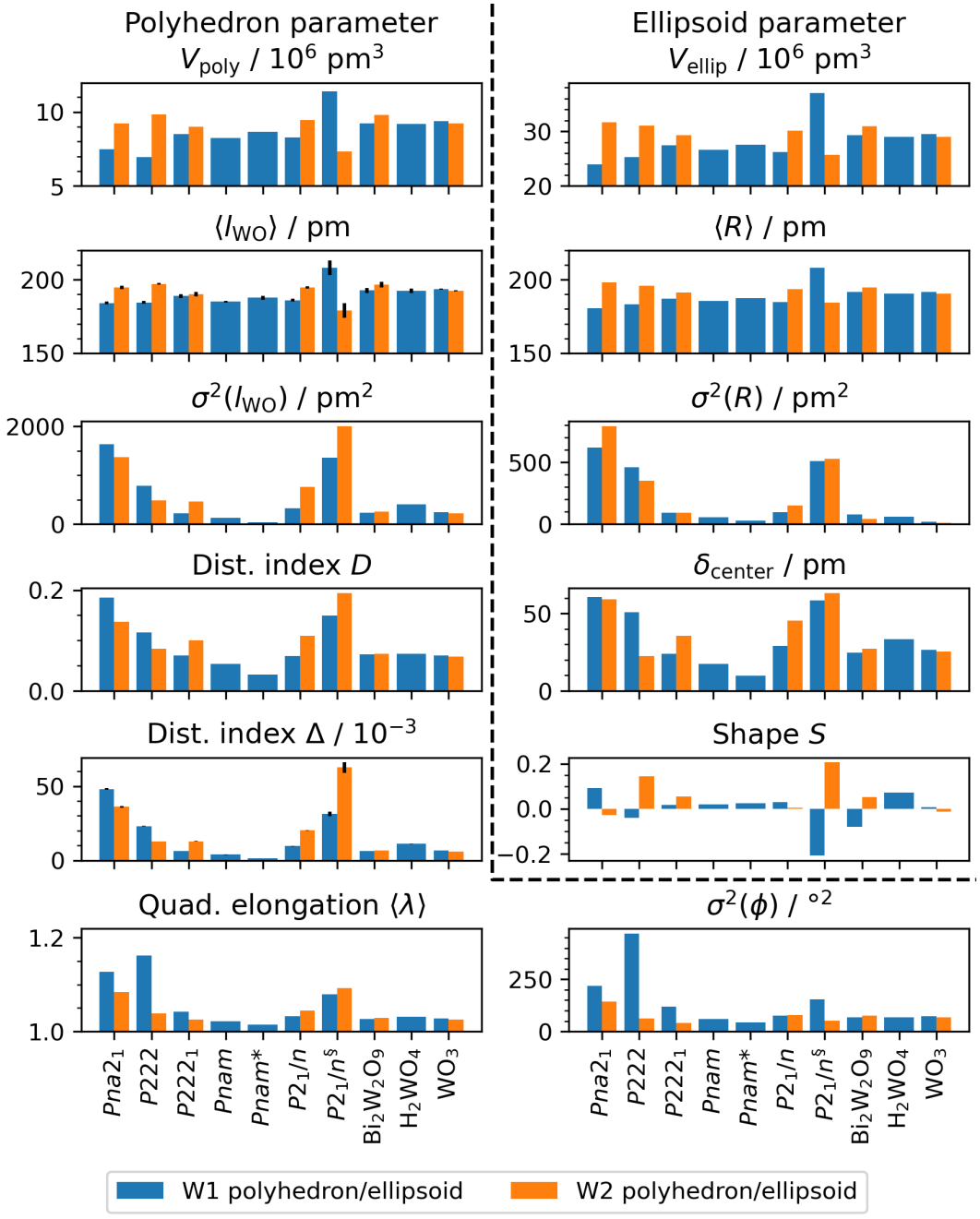

Figure 4.12: Visual comparison of the polyhedral coordinations between different models and compounds. Polyhedron parameters are polyhedral volume V_{poly}, average bond length $\langle l_{WO} \rangle$, bond length variance $\sigma^2(l_{WO})$, distortion index D, bond length distortion Δ, quadratic elongation $\langle \lambda \rangle$ and bond angle variance $\sigma^2(\phi)$. On the other hand the parameters of the minimum bounding ellipsoid: ellipsoid volume V_{ellip}, average radius $\langle R \rangle$, radius variance $\sigma^2(R)$, central atom dislocation δ_{center} and the shape parameter S.

Table 4.4: Geometrical parameters of the polyhedra in the reference compounds (RCs).

	$Bi_2W_2O_9$		H_2WO_4	WO_3	
	W1	W2	W1	W1	W2
V_{poly} / 10^6 pm^3	9.241	9.805	9.206	9.37	9.223
$\langle l_{WO} \rangle$ / pm	192.7(17)	196.7(18)	192.5(15)	193.53(29)	192.38(28)
$\sigma^2(l_{WO})$ / pm^2	231.2	257.2	409.2	247.4	223.8
Dist. index D	0.0719	0.073 05	0.073 71	0.070 58	0.067 44
Dist. index Δ / 10^{-3}	6.23(11)	6.65(12)	11.04(17)	6.604(20)	6.047(18)
Quad. elongation $\langle \lambda \rangle$	1.027	1.029	1.031	1.028	1.026
$\sigma^2(\phi)$ / °^{2}	67.38	74.55	66.33	73.36	68.05
V_{ellip} / 10^6 pm^3	29.31	30.91	28.95	29.49	29.02
$\langle R \rangle$ / pm	191.5	194.8	190.6	191.7	190.7
$\sigma^2(R)$ / pm^2	79.65	43.64	59.23	19.49	12.87
δ_{center} / pm	24.71	27.31	33.32	26.69	25.61
Shape S	−0.080 31	0.052 07	0.072 42	0.007 867	−0.012 81
BVS Σs_{ij} / v.u.	6.31(31)	5.75(30)	6.63(29)	6.21(6)	6.36(6)

nitudes across the models. The bond angle variances $\sigma^2(\phi)$ are comparable for most of the studied polyhedra pointing to a similar degree of angular distortion.

4.3.1 Related compounds (RCs)

The analysis of the related compounds provide the basis for the discussion of the other models in this study. Comparing polyhedral and ellipsoidal volumes, these show similar values and relative magnitudes for all the related compounds. Additionally, quadratic elongation, bond angle variances $\sigma^2(\phi)$ and ellipsoid radii variances $\sigma^2(R)$ indicate a similar magnitude of distortion from a regular octahedral shape. This is interpreted as a close resemblance in size and shape of the polyhedral perimeter based on the relative oxygen positions. Notably, this holds also for the single layer H_2WO_4 which exhibits a pronounced asymmetric W-O bonding situation, with the aforementioned long bond to the hydrogen bearing apical oxygen and the short bond to the opposite one. However, the shape parameter S shows different degrees of distortion for the individual RCs. While the ellipsoids are close to spheres for the tungsten trioxide case, the $Bi_2W_2O_9$ shows a slightly stronger prolate and oblate elliptic shapes. H_2WO_4 has an even more pronounced prolate shape which can be attributed to the asymmetry in the apical bonds. While respective mean bond and radius lengths are also comparable for the RCs, the width of the bond length distribution increases from WO_3 and $Bi_2W_2O_9$ to the single layer hydrotungstate H_2WO_4, which is also represented in the bond length variances $\sigma^2(l_{WO})$. For WO_3 the bond lengths of both tungsten atoms are highly comparable and lie grouped in

Table 4.5: Bond lengths and valences of the polyhedra of the related compound $Bi_2W_2O_9$.

W1			W2		
O_i	l_{WO}/pm	s_{ij}/v.u.	O_i	l_{WO}/pm	s_{ij}/v.u.
O7	215(4)	0.53(6)	O5(2)	221(4)	0.45(5)
O4	212(4)	0.58(6)	O8(2)	210(4)	0.61(7)
O3	190(5)	1.05(14)	O6	202(5)	0.76(10)
O9	180.0(30)	1.37(11)	O3	190(5)	1.05(14)
O4(2)	180(5)	1.37(19)	O8	183(4)	1.27(14)
O7(2)	179(4)	1.41(15)	O5	174(4)	1.61(18)
	BVS Σs_{ij}:	6.31(31)		BVS Σs_{ij}:	5.75(30)

Table 4.6: Bond lengths and valences of the polyhedra of the related compound H_2WO_4.

W1		
O_i	l_{WO}/pm	s_{ij}/v.u.
O1	234.0(30)	0.319(26)
O3	193(4)	0.97(10)
O3(3)	193(4)	0.97(10)
O3(2)	183(4)	1.27(14)
O3(4)	183(4)	1.27(14)
O2	169.0(30)	1.85(15)
	BVS Σs_{ij}:	6.63(29)

Table 4.7: Bond lengths and valences of the polyhedra of the related compound WO_3.

W1			W2		
O_i	l_{WO}/pm	s_{ij}/v.u.	O_i	l_{WO}/pm	s_{ij}/v.u.
O5	217.3(6)	0.501(10)	O6	214.7(5)	0.537(9)
O3(2)	210.7(8)	0.598(14)	O4(2)	209.0(8)	0.627(15)
O1	191.0(7)	1.019(22)	O2	189.5(7)	1.061(23)
O2	189.9(7)	1.050(23)	O1	189.5(7)	1.061(23)
O3	176.7(8)	1.50(4)	O4	176.8(8)	1.50(4)
O6	175.6(6)	1.545(30)	O5	174.8(6)	1.579(31)
	BVS Σs_{ij}:	6.21(6)		BVS Σs_{ij}:	6.36(6)

pairs close to the three maxima of the trimodal reference distribution. In $Bi_2W_2O_9$ (with space group $Pna2_1$) the values for W1 have a similar distribution as in WO_3 but for W2 are wider distributed. For H_2WO_4 the distribution is significantly irregular with max. and min. values near the distributions extrema. Those are attributed to the bonds to the hydrogen bearing and the opposite, double-bonded apical oxygen atoms, respectively. The respective bond valences sums of $Bi_2W_2O_9$ 6.31(31) v.u. and 5.75(30) v.u. are symmetrically close to the expected formal valence of six within their standard deviations. For WO_3 both values are slightly increased to 6.21(6) v.u. and 6.36(6) v.u., which is still well in the above-mentioned validity criterion of 0.42 v.u. deviation from the formal value. As also discussed above, in case of H_2WO_4 the value is significantly higher but still overlapping with the criterion range considering their uncertainty.

This increasing asymmetry in the W-O bonds is also reflected in the distortion indices D and Δ. A similar trend is also visible in the increased distance of the W atom from the center of the polyhedron-encompassing ellipsoid.

On one hand it can also be assumed that the double layered structure of $H_2W_2O_7$, with its increased perovskitic nature and resemblance to WO_3, is generally more rigid than the more flexible single layer hydrotungstate. Additionally, the possibly distorting influence of bismuth oxide interlayer on the tungsten oxide network is missing compared to $Bi_2W_2O_9$, opening the possibility for a relaxation towards a generally lower degree of polyhedral distortion. However, on the other hand especially the spectroscopic results suggest at least a tendency to form an asymmetric bonding situation of the apical oxygen atoms.

Chandler, Wajrak and Khan published a statistical survey of neutron diffraction determined water coordinations. The minimum, average, and maximum values for bond length and angle of water coordinated to higher valent metal cations are reported to be 93.4 pm, 98.3 pm and 101.6 pm as well as 103.9°, 109.2° and 113.8°, respectively. [165] For H_2WO_4 the OH bond lengths are l(O1-H1) = 79(3) pm and l(O1-H2) = 80(3) pm with a bond angle ϕ(H-O-H) = 110(3)°. The bond angle is close to the reported average value, however, the value of the OH bond lengths here are significantly too low. This is attributed to the structure being determined by X-ray diffraction which is only sensitive to the electron density. In case of hydrogen the only electron is located not at the nucleus but in the bond leading to the atoms distance being underestimated. W1, O1 and the H atoms are coplanar and O1 is approximately trigonally coordinated.

The similarities and trends in respective parameters of the RCs as well as the referenced surveys are considered as representative and a reasonable structure model for $H_2W_2O_7$ is thus expected to perform comparably.

4.3.2 Model in space group $Pna2_1$

The model in space group $Pna2_1$ is derived from the structure of the parent $Bi_2W_2O_9$ by removing the $Bi_2O_2^{2+}$ interlayer, shifting of the tungstate layers to close the gap and reduction of the cell parameters to the values from the Pawley refine-

Table 4.8: Geometrical parameters of the polyhedra models in space groups $Pna2_1$, $P222$ and $P222_1$.

	$Pna2_1$		$P222$		$P222_1$	
	W1	W2	W1	W2	W1	W2
V_{poly} / 10^6 pm^3	7.485	9.227	6.939	9.849	8.501	8.991
$\langle l_{WO} \rangle$ / pm	184.2(11)	194.7(13)	184.6(9)	197.2(7)	188.9(14)	190.1(14)
$\sigma^2(l_{WO})$ / pm^2	1632.0	1369.0	787.9	491.1	225.1	465.9
Dist. index D	0.185	0.1375	0.116	0.083 29	0.070 61	0.1007
Dist. index Δ / 10^{-3}	48.1(6)	36.1(5)	23.13(23)	12.64(9)	6.31(9)	12.89(19)
Quad. elongation $\langle \lambda \rangle$	1.127	1.084	1.161	1.039	1.042	1.025
$\sigma^2(\phi)$ / °^{2}	219.8	142.3	470.4	62.0	119.3	40.7
V_{ellip} / 10^6 pm^3	23.96	31.67	25.23	31.08	27.39	29.25
$\langle R \rangle$ / pm	180.5	198.3	183.2	195.9	187.2	191.4
$\sigma^2(R)$ / pm^2	619.7	792.4	460.7	350.4	92.89	93.42
δ_{center} / pm	60.54	59.25	50.94	22.46	24.08	35.73
Shape S	0.090 55	−0.029 11	−0.040 87	0.1439	0.017 27	0.054 74
BVS Σs_{ij} / v.u.	12.1(4)	7.70(33)	8.97(26)	5.97(12)	6.99(29)	7.46(30)

Table 4.9: Refined atomic parameters for the model in space group $Pna2_1$.

Site	Mult.	x	y	z	Atom	Occ.	$B_{eq}/10^4$ pm^2
W1	4	0.272(3)	0.951(2)	0.1374(2)	W^{+6}	1	1
W2	4	0.806(3)	0.504(3)	0.3452(2)	W^{+6}	1	1
O1	4	0.427(5)	0.230(5)	0.116(1)	O^{-2}	1	1
O2	4	0.068(4)	0.708(4)	0.358(1)	O^{-2}	1	1
O3	4	0.540(5)	0.726(5)	0.125(1)	O^{-2}	1	1
O4	4	0.051(5)	0.213(5)	0.334(1)	O^{-2}	1	1
O5	4	0.268(5)	0.060(4)	0.2000(8)	O^{-2}	1	1
O6	4	0.221(5)	0.976(5)	0.017(1)	O^{-2}	1	1
O7	4	0.861(5)	0.546(6)	0.428(1)	O^{-2}	1	1
H1	4	0.71(1)	0.104(9)	0.490(3)	^2H	0.63(1)[a]	1
					^1H	0.37(1)[a]	1
H2	4	0.478(9)	0.55(1)	0.494(3)	^2H	0.63(1)[a]	1
					^1H	0.37(1)[a]	1

[a] restrained to equal occupancy of 1 for each four-fold position giving 8 hydrogen atoms in total

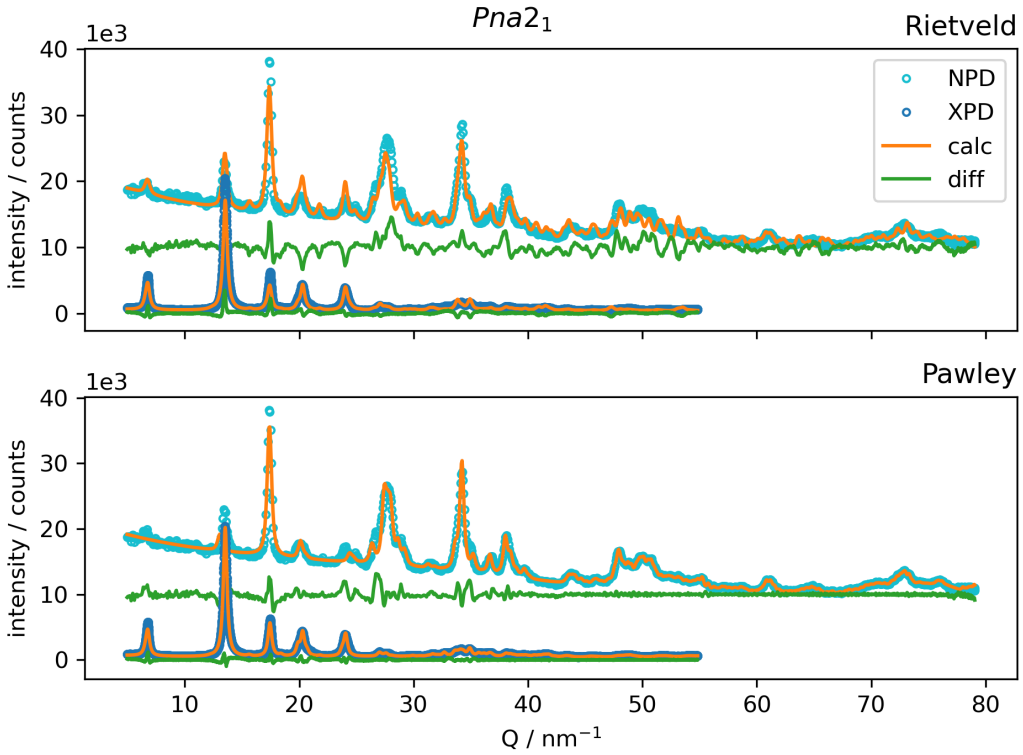

Figure 4.13: Experimental and calculated diffraction pattern from refinement with structure model in space group $Pna2_1$.

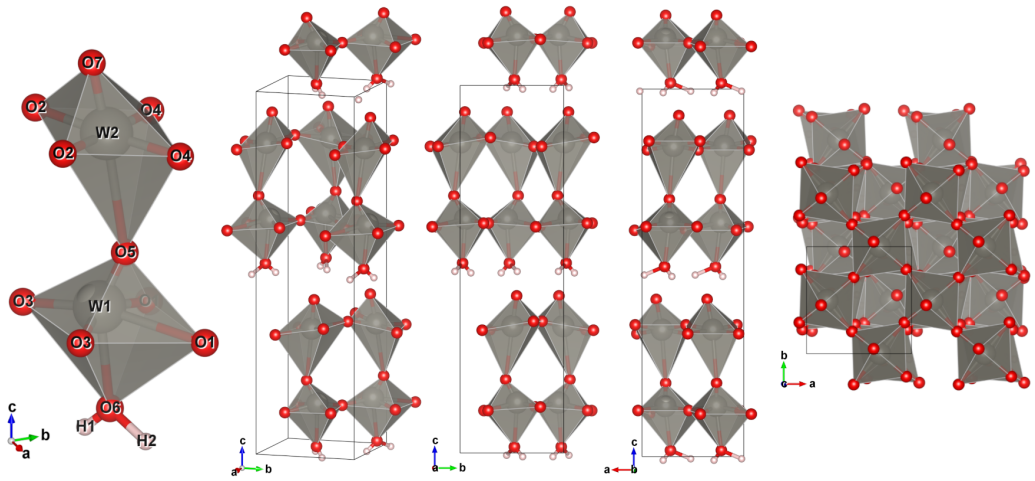

Figure 4.14: Refined structure model in space group $Pna2_1$.

Table 4.10: Bond lengths and valences of the polyhedra of the structure model in space group $Pna2_1$

W1			W2		
O_i	l_{WO}/pm	s_{ij}/v.u.	O_i	l_{WO}/pm	s_{ij}/v.u.
O1	247.0(30)	0.224(18)	O5	271.4(16)	0.116(5)
O6	224.0(20)	0.418(23)	O4(2)	198(4)	0.84(9)
O3(2)	182.0(30)	1.30(11)	O2	195.0(30)	0.91(7)
O1(2)	171.0(30)	1.75(14)	O4	174(4)	1.61(18)
O3	152.0(30)	2.92(24)	O2(2)	173.0(30)	1.66(14)
O5	129.0(18)	5.44(27)	O7	157.0(30)	2.55(21)
	BVS Σs_{ij}:	12.1(4)		BVS Σs_{ij}:	7.70(33)

ment. The subsequent Rietveld refinement resulted in a model which shows the long-bond/short-bond motif comparable to H_2WO_4, however with very high distortion in both octahedral units. The volumetric parameters for the W2 polyhedron are close to the values of the RCs in contrast to the W1 polyhedron where a large discrepancy exists. This difference between the two polyhedra holds also for $\langle l_{WO} \rangle$ and, to a lesser extent, $\langle R \rangle$. However, the spatial asymmetry for both polyhedra is huge which is reflected by the extremely broad bond length distribution. The variances $\sigma^2(l_{WO})$ and $\sigma^2(R)$, both distortion indices and the out-of-ellipsoid-center dislocation δ_{center} all exhibit the highest values of all models refined in this study. The values for quadratic elongation and bond angle variance are also amongst the highest in our results and only exceeded by the W1 polyhedron of the model in space group $P222$.

In closer inspection of the individual polyhedral arrangements several major issues become apparent. With 129.0(18) pm and 152.0(30) pm the W1-$O5_{ap}$ and W1-$O3_{eq}$ bonds, respectively, are unphysically short and far outside the reference distribution. The longest bond W1-$O1_{eq}$ in this polyhedron is not only at the very end of the reference distribution but actually also lies in the equatorial or sheet plane. This is contrary to the situation in H_2WO_4, where the hydrogen carrying oxygen atom on the apex forms the longest bond, which would correspond here to $O6_{ap,H}$. All W1-O bond angles deviate by at least $\pm 10°$ from orthogonality, leading to a large bond angle variances $\sigma^2(\phi)$. In the W2 polyhedron the shortest bond W2-O7 with a length of 157.0(30) pm is also just outside the reference distribution. With 271.4(16) pm the bond length W1-O5 is the largest encountered in our results and well beyond the maximum reference values. The O_{eq}-plane and O_{ap}-axis are significantly tilted out of orthogonality. However, since the equatorial W-O-W angles are close to 90°, the bond angle variance is still lower than in the W1 polyhedron. Due to the large contribution of the few very short bonds the respective bond valence sums are 12.1(4) v.u. (W1) and 7.70(33) v.u. (W2) and are thus approx. 100 % and 28 % higher compared to the formal tungsten valency of 6 v.u..

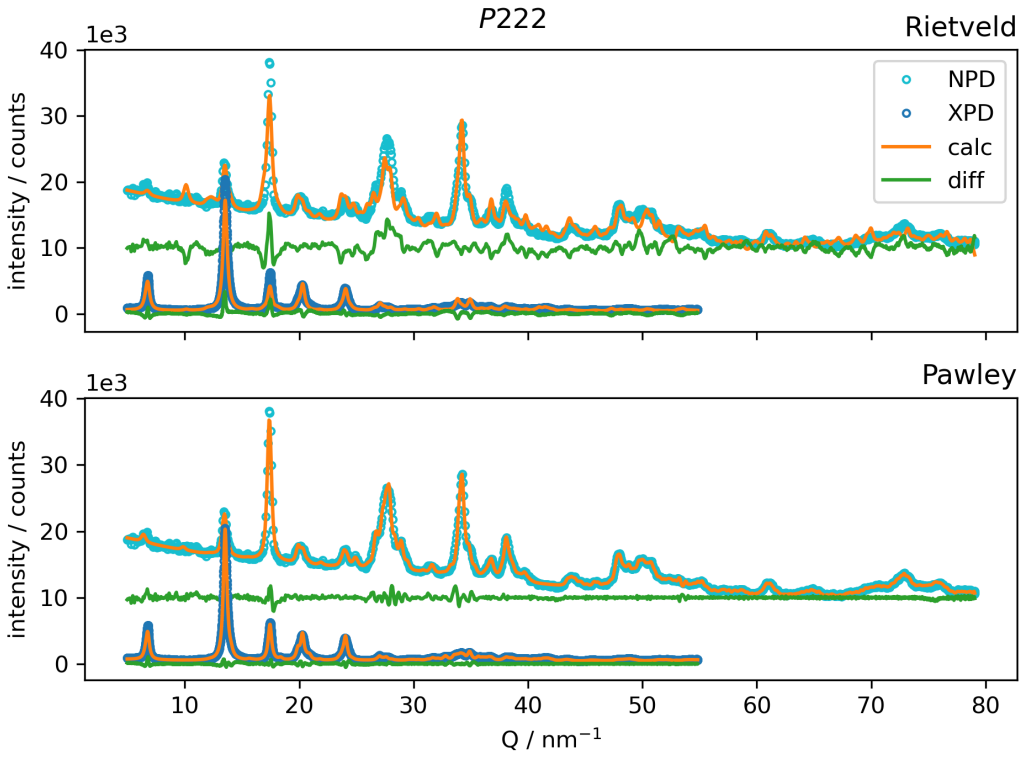

Figure 4.15: Experimental and calculated diffraction pattern from refinement with structure model in space group $P222$.

Within the O-H coordination the bond lengths of l(O6-H1) = 75(6) pm and l(O6-H2) = 118(6) pm ($\langle l_{OH} \rangle$ = 96(4) pm) deviate symmetrically from the expected value of 98.3 pm. However, their values are well outside the reported min/max values of 93.4 pm and 101.6 pm. The bond angle ϕ(H-O-H) = 112(6)° is slightly larger than the average value of 109.2°, but below the max value of 113.8°. The W atom is elevated by 24(7)° from the H_2O-plane, which can be interpreted as a tendency towards coplanarity. Notably, in this structure model the hydrogen atoms are bonded to only a single side of the pervoskite sheet contrasting the alternating fashion in H_2WO_4. While this can in principle allow for a hydrogen bonding to the next layer, it seems very unlikely to have such a directed nature. This accumulation of charges on opposite sides of the sheets is assumed to be energetically unfavorable.

This structure model clearly shows major flaws with regard to the W-O network and can thus safely be ruled out as an appropriate candidate for an average structure solution.

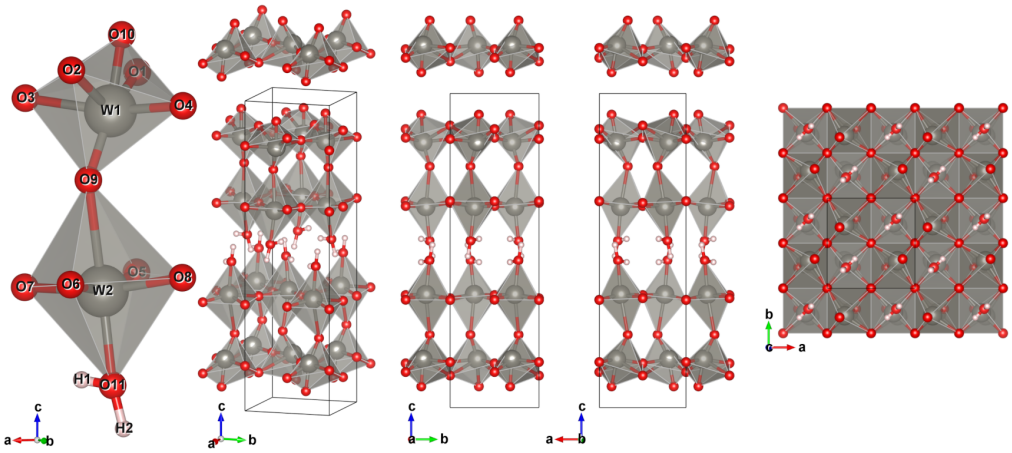

Figure 4.16: Refined structure model in space group $P222$.

Table 4.11: Refined atomic parameters for the model in space group $P222$.

Site	Mult.	x	y	z	Atom	Occ.	$B_{eq}/10^4\,\mathrm{pm}^2$
W1	4	0.199(3)	0.305(3)	0.1542(2)	W	1	1
W2	4	0.246(3)	0.272(3)	0.3606(2)	W	1	1
O1	2	0	0.5	0.113(2)	O	1	1
O2	2	0.5	0	0.102(2)	O	1	1
O3	2	0.5	0.5	0.141(2)	O	1	1
O4	2	0	0	0.145(2)	O	1	1
O5	2	0	0.5	0.343(2)	O	1	1
O6	2	0.5	0	0.348(2)	O	1	1
O7	2	0.5	0.5	0.358(2)	O	1	1
O8	2	0	0	0.343(2)	O	1	1
O9	4	0.328(4)	0.229(5)	0.2321(9)	O	1	1
O10	4	0.142(5)	0.324(5)	0.067(1)	O	1	1
O11	4	0.215(5)	0.231(5)	0.468(1)	O	1	1
H1	4	0.32(1)	0.326(9)	0.463(3)	^{2}H	0.64(1)[a]	1
					^{1}H	0.36(1)[a]	1
H2	4	0.179(9)	0.199(9)	0.518(2)	^{2}H	0.64(1)[a]	1
					^{1}H	0.36(1)[a]	1

[a] restrained to equal occupancy of 1 for each four-fold position giving 8 hydrogen atoms in total

Table 4.12: Bond lengths and valences of the polyhedra of the structure model in space group $P222$

W1			W2		
O_i	l_{WO}/pm	s_{ij}/v.u.	O_i	l_{WO}/pm	s_{ij}/v.u.
O2	242.0(30)	0.257(21)	O9	242.3(18)	0.255(13)
O4	190.1(16)	1.04(5)	O11	201.0(20)	0.78(4)
O3	186.3(17)	1.16(5)	O6	194.0(16)	0.94(4)
O9	163.0(20)	2.17(12)	O8	192.9(17)	0.97(5)
O10	163.0(20)	2.17(12)	O7	176.4(16)	1.51(7)
O1	163.0(30)	2.17(18)	O5	176.3(17)	1.52(7)
	BVS Σs_{ij}:	8.97(26)		BVS Σs_{ij}:	5.97(12)

4.3.3 Model in space group $P222$

In comparison to the previous structure in $Pna2_1$, the structure in $P222$ shows generally lower distortion, with exception of quadratic elongation and bond angle variance of the W1 polyhedron. All equatorial oxygen atoms O1 to O8 are located on special positions with a twofold multiplicity and only a variable z component. There exist two different W-O polyhedral coordinations from which the W2 polyhedron likewise is the more regular one. The W1 polyhedron is severely distorted, which is most prominently visible in the large values for quadratic elongation and the bond angle variance. It shows the lowest volume in this study as well as a significantly lower average bond length relative to the RCs. Accordingly, the ellipsoidal volume and average radii are also lower than in the RCs. The three shortest W-O bonds have the same length of 163(3) pm which is unphysically short and outside the reference distribution, similar as in the previous model. Two of these bonds are the apical W1-$O9_{ap}$ and -$O10_{ap}$ bonds of the relatively flat irregular octahedron, also reflected by an oblate MBE ($S < 0$). The third is the equatorial W1-$O1_{eq}$ bond, however, the term equatorial is in this case debateable. The O1 atom is elevated by an angle of 39(2)° out of the plane of the other equatorial oxygen atoms. This leads to a close proximity to $O10_{ap}$ with an O-O distance of only 145(4) pm and a corresponding angle ϕ($O10_{ap}$-W1-$O1_{eq}$) = 52.6(15)°, a structural motif commonly found in peroxotungstates. [166, 167] This reflected by the extreme value of the bond angle variance, the largest encountered in this study. However, due to the lack of a corresponding peroxo stretching vibration feature at typically around 800 cm to 900 cm such an arrangement is not backed by the IR spectrum of the compound. Due to the three short WO bonds the BVS again takes on a large value of 8.97(26) v.u.. The wide distribution of bond lengths, as also seen in the value of $\sigma^2(l_{WO})$, lead to comparatively high values of the distribution indices D and Δ. The W1 polyhedron exhibits the largest quadratic elongation value of this study which is attributed to the combination of small polyhedron volume and wide bond length distribution. The

comparably high value for the out-of-ellipsoid-center dislocation δ_{center} additionally reflects the highly distorted nature of this polyhedron.

The W2 polyhedron shows slightly larger volumetric parameter as well as mean bond lengths and radii compared to the RCs polyhedra with exception of the $Bi_2W_2O_9$ W2 polyhedron, whose respective values correspond closely. The bond lengths are within the reference distribution albeit close to the edges for the longest and shortest bonds. With 176.3(17) pm and 176.4(16) pm the shortest bonds connect to the equatorial $O5_{eq}$ and $O7_{eq}$, respectively, and usually correspond to W=O double bonds. However, a two-fold doubly bonded oxygen as bridging atom (W=O=W) between adjacent corner-sharing octahedra seems highly unlikely and no other literature report of such an arrangement could be found. The bonds to the apical oxygens are the longest in this polyhedron leading to a pronounced prolate shape of the MBE. Unexpectedly, the W2-$O9_{ap}$ bond is longer than the W2-$O11_{ap,H}$ bond to the hydrogen carrying oxygen atom, which is contrary to what can be seen in H_2WO_4. This could be rationalized by a similar situation of reduced charge at the O9 due to a double bond to W1, however, this bond is unphysically short as mentioned above raising doubts about the validity of this motif. The resulting BVS with 5.97(12) v.u. for this polyhedron coincides with the formal value and the distortion indices, quadratic elongation, bond angle variance as well as δ_{center} are comparable to those of the layered RCs.

The hydrogen-oxygen bond angle of 113(6)° is comparable to the expected value within its standard deviation. The bond length to H2 is with 95(5) pm as expected but to H1 with 72(6) pm significantly too short. Furthermore, there is an accumulation of all protons in a single interlayer while the other remains empty. This is presumed to be energetically even more unfavorable than in the previous model. An additional contraindication is the fact that the hydrogen positions are not only coplanar with W2 and O11 but W2-$O11_{ap}$-H2 are with a bond angle of 172(4)° also almost colinear. This is neither consistent with a tetragonal nor a trigonal coordinated oxygen.

Especially, the distortion in W1 coordination and hydrogen accumulation in a single interlayer are highly doubtful and eliminate this model for a plausible average structure description.

4.3.4 Model in space group $P222_1$

The differences between the two polyhedra in the $P222_1$ structure model are generally not as pronounced as in the previous models and the polyhedral and ellipsoid parameters are fairly close to those of the layered RCs. Most notably, the polyhedral columns parallel to the c-axis consist of two symmetry equivalent stacked polyhedra, while in the previous models these were non-equivalent. This leads to the water molecules being coordinated to both ends of individual W2 polyhedral columns and none of the W1 columns. Where the polyhedron in H_2WO_4 exhibits a short and a long bond only to the opposing apical oxygen atoms, respectively, in this model a similar short and long bond motif additionally exist within the layer/equatorial

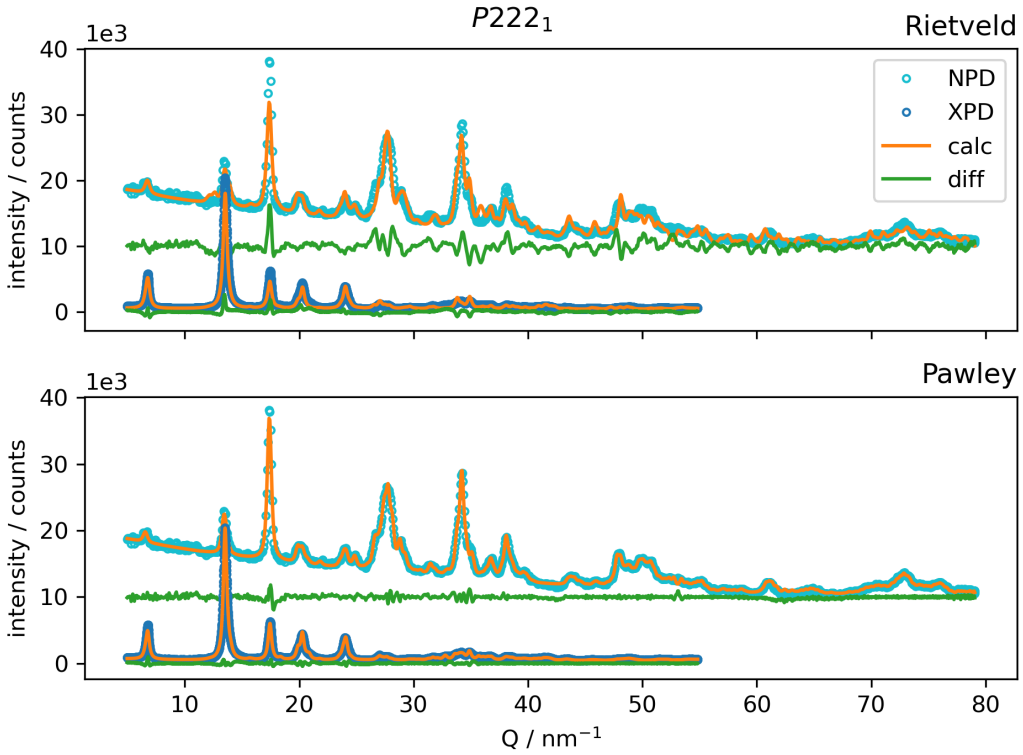

Figure 4.17: Experimental and calculated diffraction pattern from refinement with structure model in space group $P222_1$.

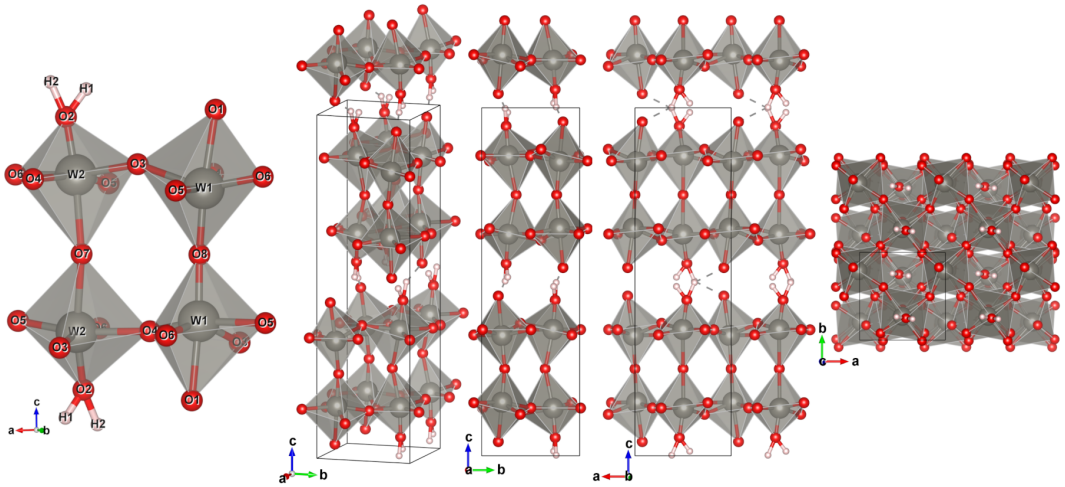

Figure 4.18: Refined structure model in space group $P222_1$.

Table 4.13: Refined atomic parameters for the model in space group $P222_1$.

Site	Mult.	x	y	z	Atom	Occ.	$B_{eq}/10^4\,\mathrm{pm}^2$
W1	4	0.982(4)	0.207(3)	0.1542(2)	W^{+6}	1	1
W2	4	0.497(5)	0.728(3)	0.1368(2)	W^{+6}	1	1
O1	4	0.924(5)	0.170(4)	0.041(1)	O^{-2}	1	1
O2	4	0.539(5)	0.750(6)	0.053(1)	O^{-2}	1	1
O3	4	0.277(5)	0.394(5)	0.119(1)	O^{-2}	1	1
O4	4	0.819(4)	0.502(5)	0.138(1)	O^{-2}	1	1
O5	4	0.244(5)	0.920(4)	0.153(1)	O^{-2}	1	1
O6	4	0.727(5)	0.009(5)	0.137(1)	O^{-2}	1	1
O7	2	0.5	0.648(5)	0.25	O^{-2}	1	1
O8	2	0	0.235(9)	0.25	O^{-2}	1	1
H1	4	0.569(8)	0.73(1)	0.487(2)	^2H	0.66(1)[a]	1
					^1H	0.34(1)[a]	1
H2	4	0.382(8)	0.760(9)	0.498(2)	^2H	0.66(1)[a]	1
					^1H	0.34(1)[a]	1

[a] restrained to equal occupancy of 1 for each four-fold position giving 8 hydrogen atoms in total

Table 4.14: Bond lengths and valences of the polyhedra of the structure model in space group $P222_1$

W1			W2		
O_i	l_{WO}/pm	s_{ij}/v.u.	O_i	l_{WO}/pm	s_{ij}/v.u.
O1	213.0(30)	0.56(5)	O7	213.8(7)	0.550(12)
O5	202.0(30)	0.76(6)	O3	211(4)	0.59(6)
O3	192(4)	0.99(11)	O4	203(4)	0.74(8)
O8	178.3(6)	1.436(28)	O6	189(4)	1.08(12)
O4	178(4)	1.45(16)	O5	167(4)	1.95(21)
O6	170(4)	1.80(20)	O2	157.0(20)	2.55(14)
	BVS Σs_{ij}:	6.99(29)		BVS Σs_{ij}:	7.46(30)

plane between W1-$O4_{eq}$-W2 and W2-$O5_{eq}$-W1. Such a motif in the equatorial plane is, however, present in $Bi_2W_2O_9$. The oxygen atoms $O7_{ap}$ and $O8_{ap}$ shared between the stacked polyhedra are located on special positions with a twofold multiplicity and only a variable y component.

The volumetric parameters for W1 polyhedron as well as average bond length and average ellipsoid radii are slightly lower compared to the RCs. All bond lengths are within the bounds of the reference distribution and the bond length variance is comparable to $Bi_2W_2O_9$. The length of the two shortest bonds W1-$O6_{eq}$ and W1-$O8_{ap}$ is in the regime of double bonds. However, similar to the situation in the previous model these are bridging atoms and the second bond to W2 and W1, respectively, is also quite short. The longest bond in the W1 polyhedron is to the apical $O1_{ap}$ atom. The additional lack of any other direct bonding partner would result in three lone electron pairs dangling into the interlayer space. Both factors would lead to a significant negative charge on this atom. This could be slightly mitigated, as the distance of 180(5) pm to the H2 proton of the adjacent layer suggest a hydrogen bond. The resulting BVS deviates by approx. 10 % from the formal value. The bond angle variance and quadratic elongation are value compared to the RCs. The values for the distortion indices and δ_{center} are similar to those of $Bi_2W_2O_9$.

The the coordinated water carrying W2 polyhedron is very similar to WO_3 in terms of volumetric parameters, average bond length and average ellipsoid radii. However, with regard to its wide bond length distribution and associated bond length variance it more resembles H_2WO_4. Correspondingly, it shows higher values of the distortion indices fitting more closely to the single-layer hydrotungstate than any other RC. Comparing the apical bonds the situation is opposite to the W1 octahedron. The two W2-$O7_{ap}$-bonds to the oxygen atom connecting the two stacked W2 polyhedra are with 213.8(7) pm elongated. Such a bond length is plausible in an asymmetric short-bond-long-bond motif but not in a symmetric bridging situation like in this case. The other apical bond W2-$O2_{ap,H}$ to the hydrogen carrying oxygen on the contrary is with 157.0(20) pm the shortest bond in this model. This bond length is not only outside the lower limit of the reference distribution but also far too short for the coordinated water. From the single layer hydrotungstate it can be expected to be fairly long.

The BVS is with 7.46(30) v.u. about approx. 25 % higher than the formal valence of six. The distortion indices D and Δ are slightly higher than those of the RCs whereas the values for quadratic elongation is comparable to and the bond angle variance smaller than in the RCs. The out-of-ellipsoid-center dislocation δ_{center} is close to the value of the single layer hydrotungstate.

The protons in the previous models were unfavorably accumulated and the resulting opposite charges of proton rich and poor regions, respectively, were separated by one or even two layer thicknesses. This model exhibits the lowest charge separation of the models so far as the oppositely charged columns are directly adjacent to each other. However, similar to the previous structure model, the approximate colinearity of W2, $O2_{ap}$ and H2 and additional coplanarity in conjunction with H1 are

Table 4.15: Geometrical parameters of the polyhedra model in space group *Pnam* and with refined B_{eq} values.

	Pnam	*Pnam**
	W1	W1
V_{poly} / 10^6 pm^3	8.226	8.649
$\langle l_{WO} \rangle$ / pm	185.0(6)	187.6(12)
$\sigma^2(l_{WO})$ / pm^2	131.6	44.02
Dist. index D	0.053 48	0.032 18
Dist. index Δ / 10^{-3}	3.846(26)	1.250(16)
Quad. elongation $\langle \lambda \rangle$	1.021	1.014
$\sigma^2(\phi)$ / °^{2}	59.96	43.55
V_{ellip} / 10^6 pm^3	26.63	27.56
$\langle R \rangle$ / pm	185.4	187.5
$\sigma^2(R)$ / pm^2	56.67	31.05
δ_{center} / pm	17.5	9.653
Shape S	0.0189	0.025 53
BVS Σs_{ij} / v.u.	7.52(14)	6.80(23)
* with refined B_{eq} values		

mutual exclusive for tetragonal and trigonal oxygen coordination. Additionally, the water HOH angle with 61(4)° only half of the expected value and thus far too narrow. The OH bond lengths are 92(5) pm and 103(5) pm to H1 and H2, respectively, which is slightly beyond but still largely overlapping with the reference min/max range within the standard deviation.

In general, based on the parameter values, the W1 polyhedron shows more similarity to $Bi_2W_2O_9$ whereas W2 is closer to H_2WO_4. While the individual WO polyhedra are comparable to the layered RCs judged by their overall geometric parameters, there exist major inconsistencies within their specific bonding scheme, especially with regard to the apical WO bonds. Furthermore, these inconsistencies increase when taking the adjacent polyhedra into account, which disqualifies also this model for a plausible average structure description.

4.3.5 Model in space group *Pnam*

While the previous structure model in itself is not plausible, it could be thought of as a tautomeric isomer of an average structure. In such an average structure the protons are delocalized between all the sheet-terminating oxygen positions. With regard to the proton environment this structure model represents a time and space average taking into account the mobility of the hydrogen atoms as well as hydrogen bonding between the sheets as indicated by NMR and FTIR spectroscopy. This idea was investigated with this model and with *Pnam* a higher symmetry was chosen to

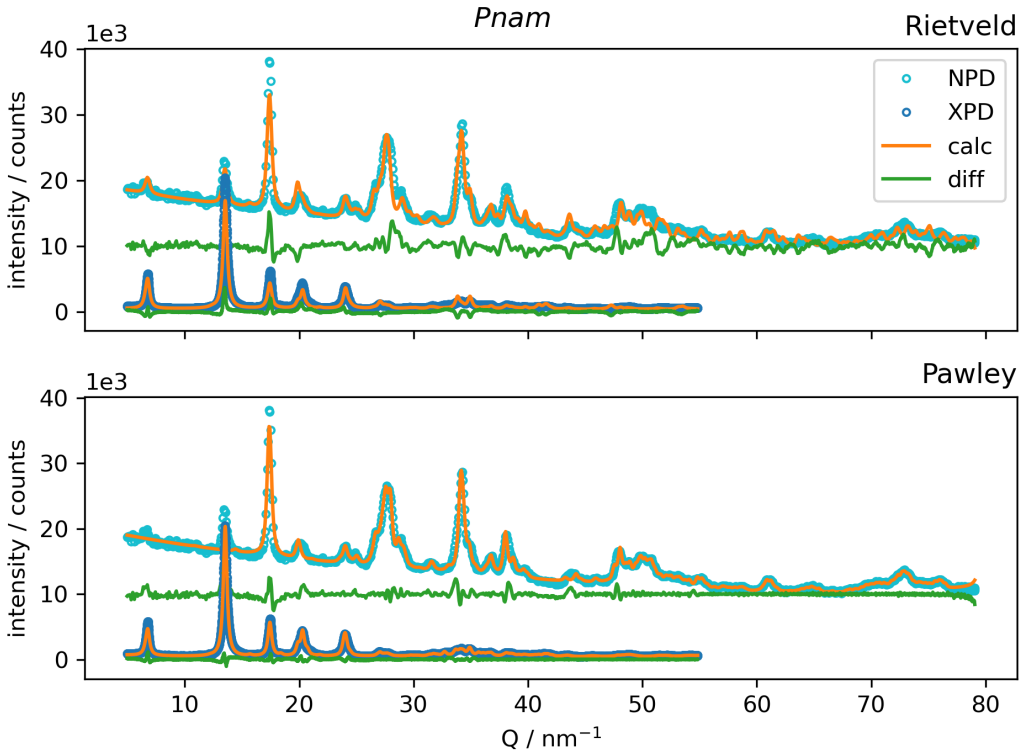

Figure 4.19: Experimental and calculated diffraction pattern from refinement with structure model in space group *Pnam*.

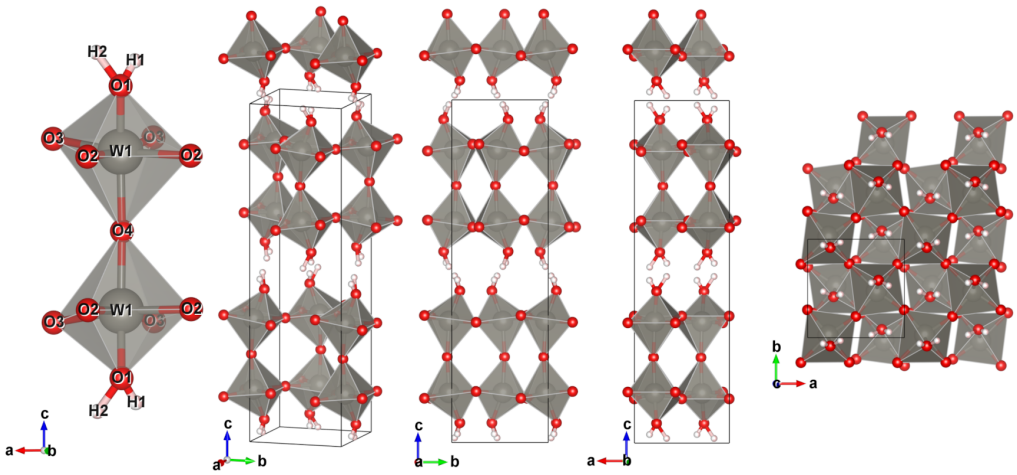

Figure 4.20: Refined structure model in space group *Pnam*.

Table 4.16: Refined atomic parameters for the model in *Pnam*.

Site	Mult.	x	y	z	Atom	Occ.	$B_{eq}/10^4\,\mathrm{pm}^2$
W1	8	0.289(1)	0.528(2)	0.1453(1)	W^{+6}	1	1
O1	8	0.267(3)	0.416(2)	0.0577(7)	O^{-2}	1	1
O2	8	0.070(2)	0.252(3)	0.1490(7)	O^{-2}	1	1
O3	8	0.002(3)	0.717(3)	0.1291(6)	O^{-2}	1	1
O4	4	0.299(4)	0.547(3)	0.25	O^{-2}	1	1
H1	8	0.34(1)	0.441(9)	0.025(3)	^2H	0.324(9)[a]	1
					^1H	0.08(5) [a]	1
H2	8	0.161(6)	0.470(6)	0.014(2)	^2H	0.455(7)[a]	1
					^1H	0.14(5) [a]	1

[a] restrained to equal net occupancy of 0.5 for both eight-fold positions giving 8 hydrogen atoms in total

Table 4.17: Bond lengths and valences of the polyhedra of the structure model in space group *Pnam*

W1		
O_i	l_{WO}/pm	s_{ij}/v.u.
O2	205.6(16)	0.687(31)
O4	194.00(30)	0.940(13)
O2(2)	183.0(16)	1.27(6)
O3(2)	179.8(18)	1.38(7)
O3	174.9(18)	1.57(8)
O1	172.7(14)	1.67(7)
	BVS Σs_{ij}:	7.52(14)

reduce the degrees of freedom. The occupancy parameter of the hydrogen atoms were restrained to a total of eight hydrogen atoms per unit cell to comply with the compound stoichiometry. The agreement factors for the refinement with this model are slightly higher than for the previous models, however, it also exhibits significantly fewer fitting parameters.

The single WO polyhedron in this model is characterized by lower volumetric parameters, average bond length and ellipsoid radius compared to the related compounds. The width of bond length distribution and respective variance are comparable to $Bi_2W_2O_9$. As expected, the long-bond/short-bond motif to the apical oxygen atoms reported for H_2WO_4 is not represented in this model due to the delocalized hydrogen atoms. However, a presumed overall longer apical oxygen bonding due to averaging can also not be observed. The average apical bond length of 183.3(7) pm in this model is significantly smaller compared to the value of 201.5(21) pm in the single layer hydrotungstate and even about 12 pm below the overall average bond length given by the statistical survey. The WO bond to the hydrogen bearing apical oxygen $O1_{ap}$ is actually the shortest in the polyhedron while the longest bond lies in the equatorial plane to one of the symmetry equivalent $O2_{eq}$ atoms. As a consequence of the number of short bonds the bond valence sum of $BVS = 7.52(14)$ v.u. deviates by roughly 25 % from the formal value. The values of the distortion indices D and Δ as well as quadratic elongation $\langle\lambda\rangle$ are even lower than those of $Bi_2W_2O_9$ and WO_3. Also, the bond angle variance $\sigma^2(\phi)$ is slightly lower compared to the RCs.

The occupancies of the two hydrogen position were not restrained to be equally filled in order to evaluate the possibility of a preferred average position. The refined occupancies indicate the H2 position to be slightly favored over H1 with a ratio of about 3:2. The $O1_{ap}$-H2 bond with a length of 102(4) pm is slightly larger than the reported maximum value but the literature average of 98.3 pm is still covered by the standard deviation. In case of the less occupied H1 site, the respective $O1_{ap}$-H2 bond length of 73(6) pm is significantly too low. The H_2O bond angle of 64(5)° is only 58 % of the reported average angle. Regarding the ion mobility in the interlayer space it is reasonable to assume that also two hydroxyl groups could be formed instead of a water molecule. This is in line with DFT calculations for structures with additional electrochemically inserted protons, which indicate a significant amount of added protons bind to vacant apical oxygen atoms. [96] The possibility of hydroxyl groups was not specifically accounted for in this model which might cause the deviations from a more regular water-like arrangement.

Additionally, the results of a refinement of this model with refined isotropic displacement parameter B_{eq} are shown here as an example. The B_{eq}-values take on very high values for the tungsten and oxygen while being negative and thus unphysical for hydrogen. This behavior is similar also for the other models but was not studied in detail and hence is not given here. Overall, there are only small differences to the model with fixed B_{eq} parameters. The polyhedral and ellipsoid volume are slightly increased and hence closer to the RCs values. The average bond length behaves in the same way. The difference to the average values of the RCs and the

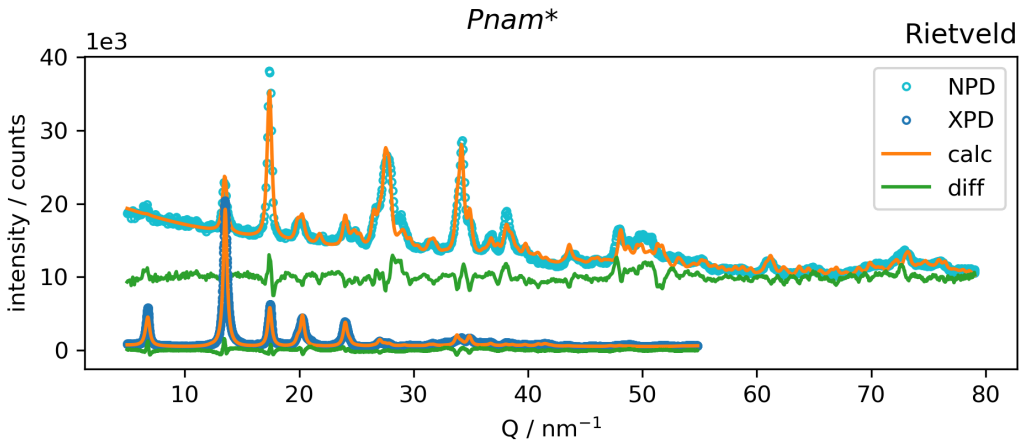

Figure 4.21: Experimental and calculated diffraction pattern from refinement with structure model in space group *Pnam* with refined B_{eq}-values.

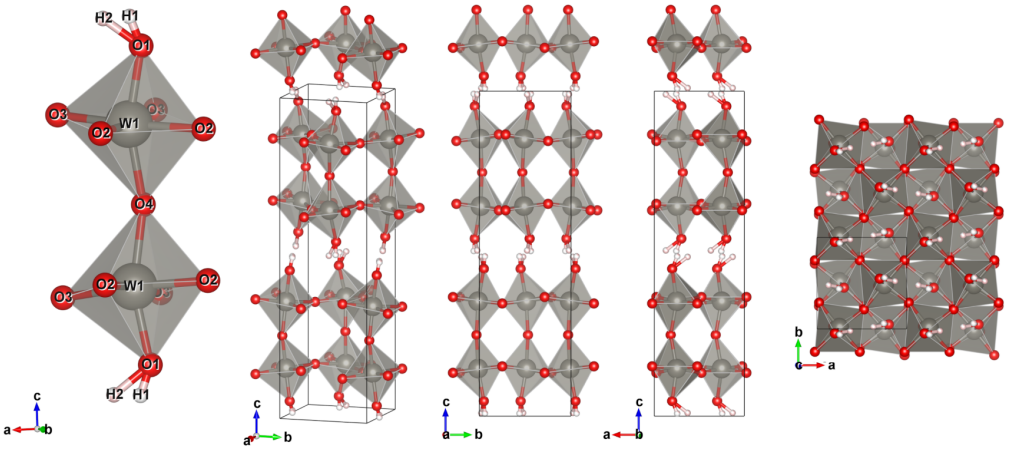

Figure 4.22: Refined structure model in space group *Pnam* with refined B_{eq}-values.

Table 4.18: Refined atomic parameters for the model in space group *Pnam* with refined B_{eq}-values.

Site	Mult.	x	y	z	Atom	Occ.	$B_{eq}/10^4\,\mathrm{pm}^2$
W1	8	0.252(4)	0.513(4)	0.1463(1)	W^{+6}	1	9.2(2)
O1	8	0.301(3)	0.451(3)	0.0465(6)	O^{-2}	1	2.7(3)
O2	8	0.023(4)	0.250(5)	0.1533(7)	O^{-2}	1	5.8(4)
O3	8	0.976(3)	0.713(2)	0.1334(5)	O^{-2}	1	2.5(2)
O4	4	0.317(3)	0.531(3)	0.25	O^{-2}	1	1.8(3)
H1	8	0.245(7)	0.439(6)	0.008(2)	^2H	0.16(1) [a]	−2.8(8)
					^1H	0.07(3) [a]	−2.8(8)
H2	8	0.129(4)	0.478(3)	0.0099(8)	^2H	0.342(4)[a]	−5.3(6)
					^1H	0.43(3) [a]	−5.3(6)

[a] restrained to equal net occupancy of 0.5 for both eight-fold positions giving 8 hydrogen atoms in total

Table 4.19: Bond lengths and valences of the polyhedra of the structure model in space group *Pnam* with refined B_{eq}-values.

W1		
O_i	l_{WO}/pm	s_{ij}/v.u.
O2	196(4)	0.89(10)
O4	195.3(6)	0.907(18)
O1	189.6(13)	1.06(4)
O3	185.0(30)	1.20(10)
O2(2)	182(4)	1.30(14)
O3(2)	178.0(30)	1.45(12)
	BVS Σs_{ij}:	6.80(23)

literature survey is reduced, however, the actual value is nonetheless significantly below the reference values. Due to the overall shorter bonds the respective BVS is about 13 % higher than the formal value.

In comparison to the model with fixed isotropic displacement parameters and the layered RCs, here the bond length distribution is narrower, additionally represented by a smaller value of the bond length variance. Also, all distortion parameters are lower. As such, the polyhedral arrangement resembles more that of WO_3. The comparably low polyhedral distortion is attributed to a more pronounced averaging of the tungsten and oxygen positions due to the large B_{eq}-values. It is presumed to be the result of a compensation of long range structural disorder in the sample. Unexpectedly, there are significant differences in the B_{eq} values of the equatorial oxygen atoms. The highest value for all oxygens can be found at the equatorial O2. This is contrary to the expectation that the layer terminating apical oxygen O1 would show the highest displacement. If hydrogen atoms were being statistically bound to it, it is assumed to result in a smearing of electron density around the average oxygen position.

The refined hydrogen positions are very close to each other with OH distances of l(O1-H1) = 77(4) pm and l(O1-H2) = 1.12(3) pm and a very narrow H_2O angle of only 33(3)°. With an asymmetric proton occupancy ratio H2:H1 = 10:3, the refinement favors a hydroxo motif over a water-like arrangement with half occupied hydrogen positions. However, the negative B_{eq} values for hydrogen atoms point out severe problems with the description of the hydrogen environment rendering attempts on an interpretation futile.

4.3.6 Model in space group $P2_1/n$

Wang, Sun et al. reported on their investigation on the hydrotungstate concluding on a structure model in spacegroup $P21/n$. [96] The authors claim to have validated their structural model by Rietveld refinement of X-ray diffraction data and the reported structure was included in the polyhedral analysis for reference. The results from the reported structure model are superscripted with § to discern from our results from combined X-ray and neutron refinement.

A superficial analysis of the reported model shows very broad W-O bond length distributions and respective high variances for both polyhedra. The actual bond lengths partly lie far outside the reference distribution and can be considered unphysical. The irregular bonding results in generally high distortion parameters. No comments were given on the hydrogen environment, as this refinement was done on X-ray data. Being based only on X-ray data, the Rietveld refinement seems to be affected by the same, aforementioned problems of intrinsic disorder in the sample and scattering characteristics of the constituents, i.e. strong scattering by W vs. low contributions by O. Without going into detail, the reported structure can hardly be considered validated in terms of the applied criteria.

Our combined Rietveld refinement of this model on neutron and X-ray data show the best agreement factors of this study. The increase to the previous models is

Table 4.20: Geometrical parameters of the polyhedra model in space group $P2_1/n$ from our combined refinements and as published (denoted with §).

	$P2_1/n$		$P2_1/n$§	
	W1	W2	W1	W2
V_{poly} / 10^6 pm^3	8.296	9.464	11.38	7.346
$\langle l_{WO} \rangle$ / pm	186.1(10)	194.5(8)	208(5)	179(5)
$\sigma^2(l_{WO})$ / pm^2	331.3	762.8	1356.0	2005.0
Dist. index D	0.068 99	0.1091	0.1497	0.1943
Dist. index Δ / 10^{-3}	9.57(10)	20.15(16)	31.3(15)	62.6(35)
Quad. elongation $\langle \lambda \rangle$	1.033	1.045	1.079	1.092
$\sigma^2(\phi)$ / °^{2}	75.68	78.79	153.2	51.1
V_{ellip} / 10^6 pm^3	26.23	30.12	36.98	25.66
$\langle R \rangle$ / pm	184.6	193.4	208.0	184.3
$\sigma^2(R)$ / pm^2	98.4	153.0	511.2	527.1
δ_{center} / pm	29.19	45.38	58.45	63.37
Shape S	0.029	0.004 862	−0.2079	0.2068
BVS Σs_{ij} / v.u.	8.03(20)	6.85(17)	7.3(11)	12.9(21)

Table 4.21: Refined atomic parameters for the model in space group $P2_1/n$.

Site	Mult.	x	y	z	Atom	Occ.	$B_{eq}/10^4$ pm^2
W1	4	0.4076(1)	0.245(2)	0.245(3)	W	1	1
W2	4	0.6183(1)	0.257(2)	0.223(2)	W	1	1
O1	4	0.2936(6)	0.696(4)	0.798(4)	O	1	1
O2	4	0.3810(9)	0.997(3)	0.011(4)	O	1	1
O3	4	0.3948(7)	0.528(3)	0.473(3)	O	1	1
O4	4	0.6195(8)	0.961(3)	0.478(3)	O	1	1
O5	4	0.5836(7)	0.532(3)	0.064(3)	O	1	1
O6	4	0.4861(6)	0.184(3)	0.282(4)	O	1	1
O7	4	0.7015(7)	0.654(3)	0.758(4)	O	1	1
H1	4	0.786(2)	0.745(8)	0.303(9)	^{2}H	0.57(1)[a]	1
					^{1}H	0.43(1)[a]	1
H2	4	0.755(2)	0.834(7)	0.283(8)	^{2}H	0.57(1)[a]	1
					^{1}H	0.43(1)[a]	1

[a] restrained to equal occupancy of 1 for each four-fold position giving 8 hydrogen atoms in total

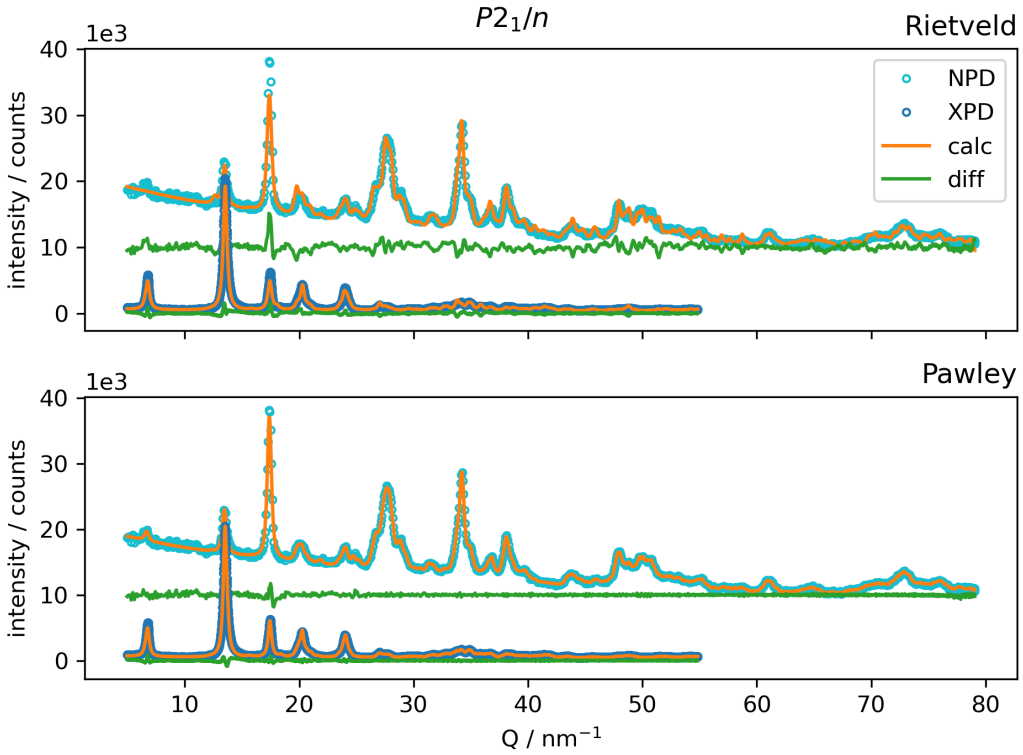

Figure 4.23: Experimental and calculated diffraction pattern from refinement with structure model in space group $P2_1/n$.

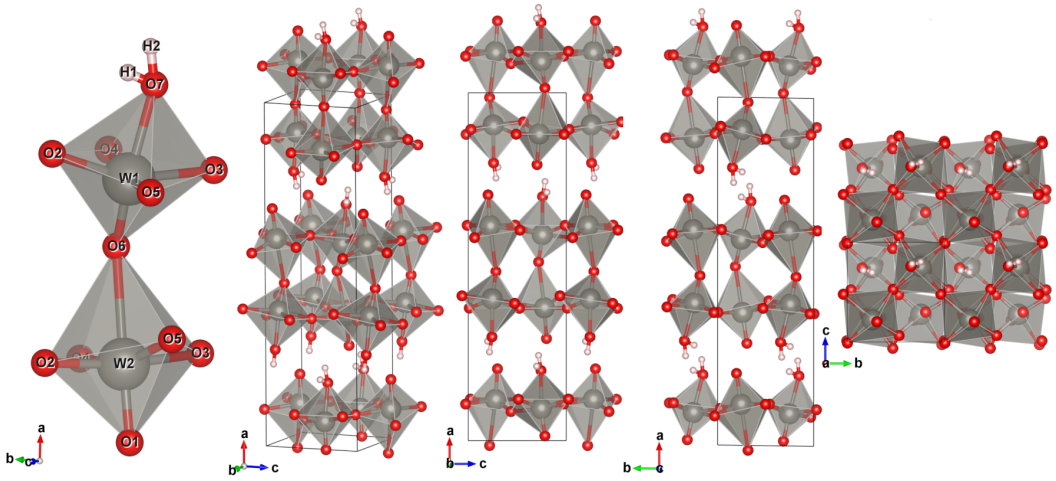

Figure 4.24: Refined structure model in space group $P2_1/n$.

Table 4.22: Bond lengths and valences of the polyhedra of the structure model in space group $P2_1/n$ as published by Wang, Sun et al. [96]

W1			W2		
O_i	l_{WO}/pm	s_{ij}/v.u.	O_i	l_{WO}/pm	s_{ij}/v.u.
O7	238(8)	0.29(6)	O6	273(8)	0.111(24)
O2	230(20)	0.36(19)	O3	190(15)	1.0(4)
O5	229(6)	0.36(6)	O4	168(11)	1.9(6)
O4	228(11)	0.37(11)	O2	149(17)	3.2(15)
O3	191(13)	1.0(4)	O5	148(10)	3.3(9)
O6	133(8)	4.9(11)	O1	146(10)	3.4(9)
	BVS Σs_{ij}:	7.3(11)		BVS Σs_{ij}:	12.9(21)

Table 4.23: Bond lengths and valences of the polyhedra of the structure model in space group $P2_1/n$ from our combined refinement

W1			W2		
O_i	l_{WO}/pm	s_{ij}/v.u.	O_i	l_{WO}/pm	s_{ij}/v.u.
O7	207.9(14)	0.645(25)	O6	250.1(12)	0.206(7)
O5	199.0(30)	0.82(7)	O4	202.0(19)	0.76(4)
O3	189.0(20)	1.08(6)	O3	195.0(19)	0.91(5)
O4	187.0(30)	1.14(9)	O2	179.0(30)	1.41(12)
O2	184.0(30)	1.23(10)	O5	175.4(18)	1.55(8)
O6	149.6(13)	3.12(11)	O1	165.8(12)	2.01(7)
	BVS Σs_{ij}:	8.03(20)		BVS Σs_{ij}:	6.85(17)

significant even though this models also has the highest number of fitting parameters. Besides that, a major point in favor of this model is the fact that the long bond short bond motif to the polyhedron apices known from single layer H_2WO_4 is well reproduced, as can be seen in Figure 4.24. However, the detailed analysis reveals problems in the refined geometry. The W1 polyhedron has a distinct disparate bond length distribution, with a majority grouped around the expected WO bond length and a single outlier. The latter corresponds to the apical oxygen $O6_{ap}$ shared between the stacked octahedra. With its length of only 149.6(13) pm it lies far outside the reference distribution. Notably, the opposite bond to the hydrogen carrying oxygen atom $O7_{ap,H}$ is with 207.9(14) pm only moderately elongated with respect to the equatorial bonds. This is contrasting the case of the single layer H_2WO_4, where the respective bond to $O1_{ap,H}$ is with 234.0(30) pm distinctly longer than the all other bonds in the polyhedron. The bond length variance is comparable to other layered RC. Due to the single extremely short bond the resulting BVS is about 33 % larger than the formal value and nowhere near the validity criterion of max. 6 %.

The W2 polyhedron bond distribution is comparable to the single layer H_2WO_4 with a single significantly elongated bond to the apical $O6_{ap}$, even though no protons are attached here. The distribution stretches a broader range with the min/max values lying outside the limits of the reference distribution. This is again reflected in the bond length variance being significantly higher than for the RCs. The BVS of 6.85(17) v.u. differs by about 14 % from the formal value and also exceeds the validation criterion.

When comparing the equatorial oxygen bonds shared between both polyhedra, a longer than average bond to one tungsten atom is accompanied by a shorter to the other one. The exception is the O2 atom where both are shorter than average. The apical $O6_{ap}$ atom connecting the stacked octahedra shows the strongest bond asymmetry with bond lengths of l(W1-O6) = 149.6(13) pm and l(W2-O6) = 250.1(12) pm, both outside the reference distribution. The fact that the especially apical bonds show the most severe deviations from the references further reinforces the hypothesis that the distortion mainly lies within the layer stacking direction, e.g. variable layer spacing.

The volume and the average bond length of the W2 polyhedron are on a par with the RCs while for W1 they deviate towards smaller values. The trends are again well represented in the respective ellipsoid parameters

With regard to bond length variance and the distortion parameters the situation is opposite. The values of the W1 polyhedron are comparable to the RCs and the values in W2 polyhedron are in this case significantly higher. The same is visible in the ellipsoid out-of-center dislocation, where in the W1 case the value is close to the layered RCs while in W2 it is increased.

In terms of their bond angle variance both polyhedra show only minor deviation from the RCs. The values are increased by a maximum of $10\,^{\circ 2}$, respectively 12 % from the RCs average.

The refined arrangement of the structural water at $O1_{ap,H}$ does not represent a

valid bonding scheme. The bond lengths of 62(5) pm and 82(4) pm to H1 and H2, respectively, are way too short. Also the angle of 60(5)° is only roughly half of the expected around 110°. In principle, the same argument as for the model in *Pnam* about the influence of possibly present hydroxyl groups can be made here.

With regard to the applied validation criteria, our combined Rietveld refinement on both neutron and X-ray data performs better than the refinements of Wang, Sun et al. on only X-ray data, making a strong case for the complementarity of both probes. [96] However, the discussed issues also present in this model again shows an inability to describe a consistent average structure for the compound.

4.3.7 Discussion on the Rietveld refinements

Generally, the additional information from the neutron diffraction were helpful and necessary to enable this study. However, the improvement was not as pronounced as hoped for. The main reason for the problems in the structure description is clearly the disorder in the sample and not in the lack of scattering contributions. The unfortunate spoilage of the sample with protium did not seem to have impacted the results much. All refinements (except for the one with refined B_{eq} values) show comparable H-D-ratios of approx. 1:2 to 1:3. With this ratio the resulting scattering length from a statistical hydrogen mixture is significant and also significantly different from oxygen. Any problems with regard to scattering contrast arising due to isotopic mixture on the hydrogen position can thus be ruled out.

From the Rietveld refinements no unequivocal conclusion on the best structure model for $H_2W_2O_7$ could be drawn, although the models in *Pnam* and $P2_1/n$ are performing best.

The structure model in *Pnam* describes a consistent average structure with agreement factors similar to the other orthorhombic models. It shows reasonable low values of the distortion parameter. The polyhedra and mean bond lengths are only slightly smaller than can be expected from the RCs and the bond valences are comparably close to the formal value.

The structure model in $P2_1/n$ shows the best agreement with the experimental data. The fact, that the bonding pattern is comparable to the single layer H_2WO_4 is a strong advocate in favor of this model. Similar to the previous model, the polyhedra and mean bond lengths are comparable to the RCs. The BVS values also deviate only moderately from the formal value. However, the maximum and minimum bond lengths lie well outside the reference distribution. Furthermore, most of the distortion parameters are significantly increased in comparison to the *Pnam* model and the RCs.

This study also shows the difficulty to quantify "distortion" with a single parameter, as trends are generally similar but individual parameters more susceptible to specific types of distortion

An arguably short-coming of the applied procedure is the non-exhaustive probing of the parameter space in all chosen space groups. An averaging with only partially occupied hydrogen positions, for instance, is in principle possible for all the structure

models. However, such works were considered futile based on the diffraction data at hand.

These structure models may, however, give an overview of possible features and motifs to encounter in large-box approaches, such as Monte-Carlo based individual atomic displacement, or for layer based stacking-fault estimation. As an example, one may extract specific motifs from the discussed hydrogen-rich interlayer environments. An according charge accumulation leading to electrostatic repulsion of adjacent layers could correspond to the regions of larger interlayer spacing observed in TEM micrographs.

On a more general note, it needs to be stated that the structures are results of a highly iterative, manual refinement process. Sometimes minor adjustments in the starting parameters on subsequent refinement runs were applied to guide the process towards seemingly more reasonable results. Even so, it is likely that the refinement results do not represent global minima of their respective residual surfaces.

The model refinements could have been driven to result in more sensible local arrangements with more restraints, especially with regard to bond-lengths and angles. In a sense the different symmetry restrictions work similarly. However, driving this too far would mean no information gain rather imposing order and biasing the refinement. Instead, the data tells a different story, namely the sample's actual atomic arrangement challenges the notion of a periodic unit cell, i.e. small-box Rietveld approaches are not suited to describe it.

Appendix

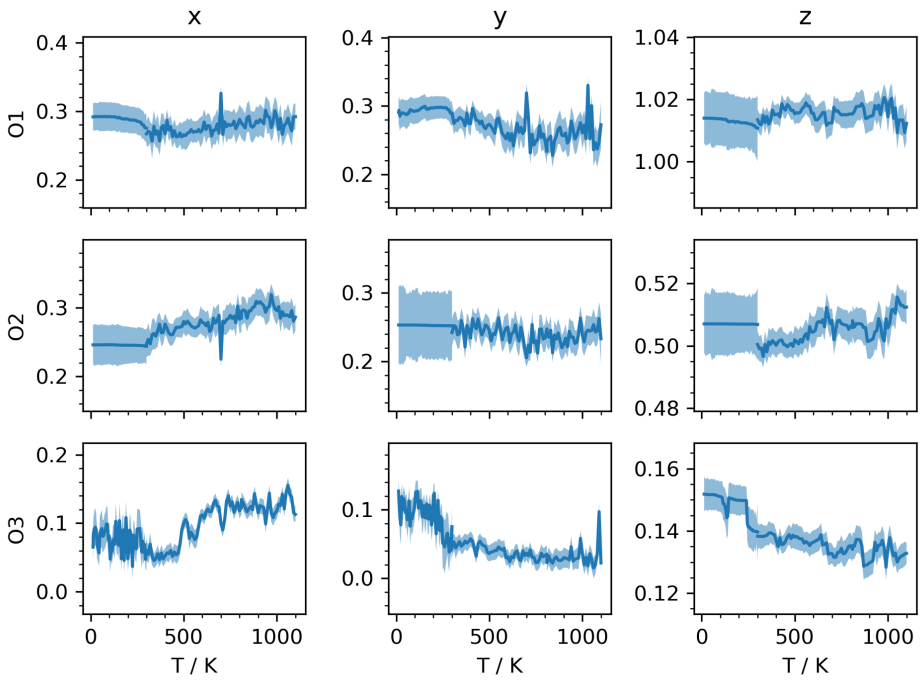

Figure A1: Temperature dependent positional coordinates of O1, O2 and O3 in Bi_2WO_6

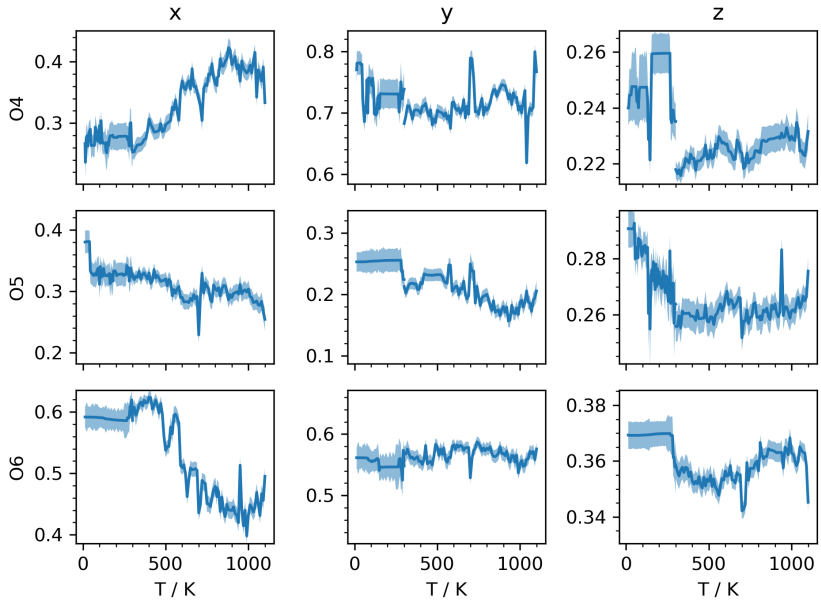

Figure A2: Temperature dependent positional coordinates of O4, O5 and O6 in Bi_2WO_6

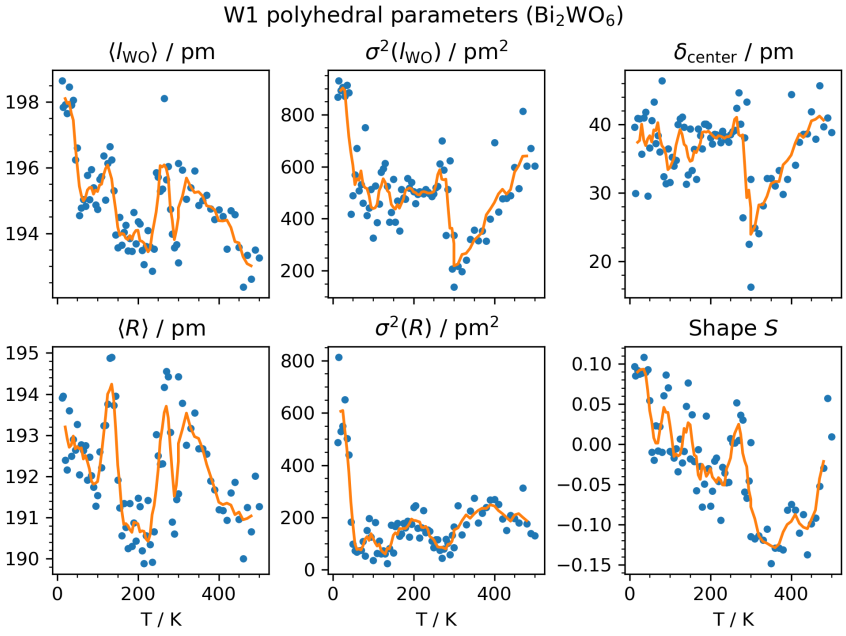

Figure A3: Bond length average and variance as well as ellipsoid parameters for the tungsten coordination in Bi_2WO_6 below 500 K. Each plotted line is a rolling average with a window size of five data points and serves as guide for the eye.

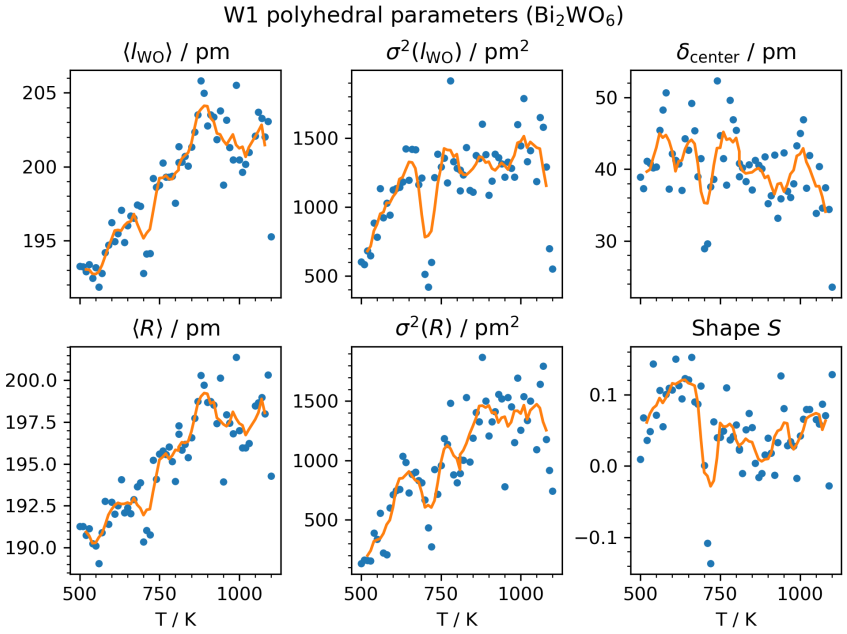

Figure A4: Bond length average and variance as well as ellipsoid parameters for the tungsten coordination in Bi_2WO_6 above 500 K. Each plotted line is a rolling average with a window size of five data points and serves as guide for the eye.

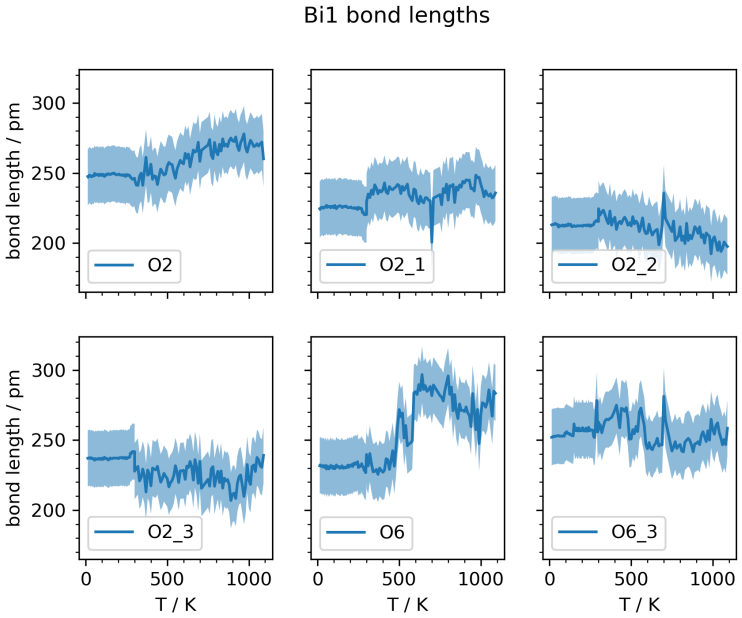

Figure A5: Bond lengths in the Bi1 coordination in Bi_2WO_6

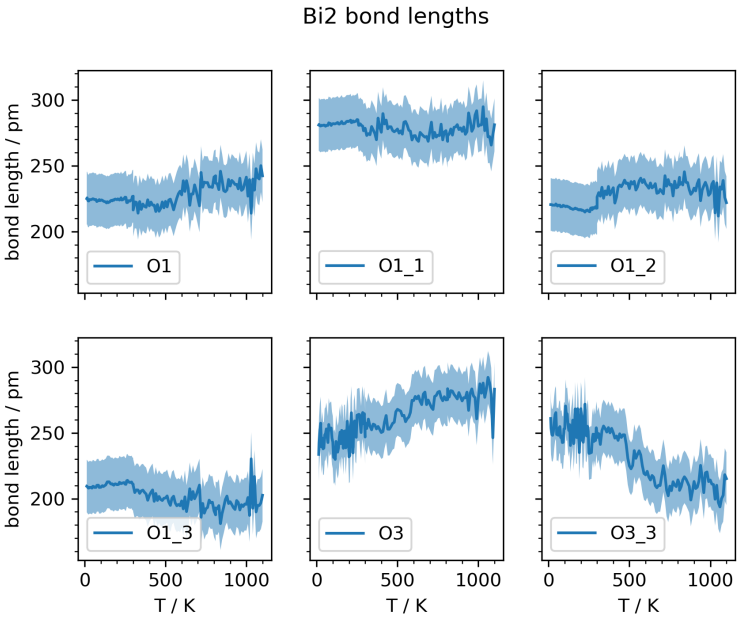

Figure A6: Bond lengths in the Bi2 coordination in Bi_2WO_6

List of Figures

1.1 Schematics of structure types covered in this thesis or related to those. 2
1.2 Three-dimensional networks of octahedra in the perovskite and perovskite-like structure types. 3
1.3 Examples of Aurivillius-type structures with varying n 6
1.4 Structure of Bi_2WO_6 9
1.5 Bi coordination in Bi_2WO_6 9
1.6 Structure of $\gamma'''-Bi_2WO_6$ 12
1.7 Structure of $\gamma' Bi_2WO_6$ 12
1.8 Structure of $Bi_2W_2O_9$ 15
1.9 Bi coordination in $Bi_2W_2O_9$ 15
1.10 Examples of Ruddlesden-Popper-type structures with varying n . . . 16
1.11 Structure of the $n = 1$ RP-like hydrotungstate H_2WO_4 in SG $Pmcn$ 19
1.12 Structure of the $n = 1$ RP-like hydrotungstate H_2WO_4 in SG $P2_12_12_1$ 19
1.13 Structure of $n = 2$ RP $H_2W_2O_7$ from PDF refinement 24
1.14 Related structural motifs with corner-sharing WO-octahedra 24

3.1 HT XRD autocorrelation 37
3.2 Parameters from Rietveld refinement of Bi_2WO_6 38
3.3 Temperature dependent positional coordinates of W1, Bi1 and Bi2 in Bi_2WO_6 40
3.4 Bond length development for the tungsten coordination in Bi_2WO_6 . 42
3.5 Temperature-dependent bond valence sum for the tungsten coordination in Bi_2WO_6 42
3.6 W1 polyhedral parameters of Bi_2WO_6 43
3.7 Temperature-dependent bond valence sum for both bismuth coordinations in Bi_2WO_6 45
3.8 Bi polyhedral parameters of Bi_2WO_6 46
3.9 Low-temperature $BiWO_6$ Raman spectra 47
3.10 High-Temperature $BiWO_6$ Raman spectra 48
3.11 Autocorrelation of the $BiWO_6$ Raman spectra 48
3.12 Selected modes from Raman peak fitting. Naming scheme: s - stretch, b - bending, t - translational, ap - apical oxygen, eq - equatorial oxygen. 50
3.13 Heatflow data from DSC measurements on Bi_2WO_6 51

4.1 XPD pattern of the educt $Bi_2W_2O_9$ and product $H_2W_2O_7$ of the leaching synthesis. 55
4.2 SEM micrograph of platelet-like $H_2W_2O_7$ particles 56

4.3 TEM micrographs of different defect themes 58
4.4 Fit of ^{1}H MAS NMR Hahn-echo spectrum of the hydrotungstate . . 59
4.5 Comparison of FTIR and Raman spectra of $Bi_2W_2O_9$ and $H_2W_2O_7$ 60
4.6 Fit of FTIR and Raman spectra of $H_2W_2O_7$ 61
4.7 Time-dependent ATR infrared spectroscopy measurement series of deuterated hydrotungstate. Upon contact with atmospheric water the intensity of the D_2O-bending signal vanishes almost completely over the course of one hour. 64
4.8 Second harmonic generation response of $H_2W_2O_7$ 64
4.9 Neutron and X-ray powder diffraction patterns 66
4.10 WO bond length distributions for the different structure models and reference structures 70
4.11 Bond valence sums of the WO coordinations in the different structure models 71
4.12 Visual comparison of the polyhedral coordinations between different models and compounds 72
4.13 Experimental and calculated diffraction pattern from refinement with structure model in space group $Pna2_1$. 77
4.14 Refined structure model in space group $Pna2_1$. 77
4.15 Experimental and calculated diffraction pattern from refinement with structure model in space group $P222$. 79
4.16 Refined structure model in space group $P222$. 80
4.17 Experimental and calculated diffraction pattern from refinement with structure model in space group $P222_1$. 83
4.18 Refined structure model in space group $P222_1$. 83
4.19 Experimental and calculated diffraction pattern from refinement with structure model in space group $Pnam$. 87
4.20 Refined structure model in space group $Pnam$. 87
4.21 Experimental and calculated diffraction pattern from refinement with structure model in space group $Pnam$ with refined B_{eq}-values. . . . 90
4.22 Refined structure model in space group $Pnam$ with refined B_{eq}-values. 90
4.23 Experimental and calculated diffraction pattern from refinement with structure model in space group $P2_1/n$. 94
4.24 Refined structure model in space group $P2_1/n$. 94

A1 Temperature dependent positional coordinates of O1, O2 and O3 in Bi_2WO_6 99
A2 Temperature dependent positional coordinates of O4, O5 and O6 in Bi_2WO_6 100
A3 W1 polyhedral parameters of Bi_2WO_6 below 500 K 100
A4 W1 polyhedral parameters of Bi_2WO_6 above 500 K 101
A5 Bond lengths in the Bi1 coordination in Bi_2WO_6 101
A6 Bond lengths in the Bi2 coordination in Bi_2WO_6 102

List of Tables

4.1 Spectroscopic mode assignment and comparison 62
4.2 Selected agreement factors for different models from combined refinements. 67
4.3 Lattice parameters for different models from combined refinements. 69
4.4 Geometrical parameters of the polyhedra in the reference compounds (RCs). 73
4.5 Bond lengths and valences of the polyhedra of the related compound $Bi_2W_2O_9$. 74
4.6 Bond lengths and valences of the polyhedra of the related compound H_2WO_4. 74
4.7 Bond lengths and valences of the polyhedra of the related compound WO_3. 74
4.8 Geometrical parameters of the polyhedra models in space groups $Pna2_1$, $P222$ and $P222_1$. 76
4.9 Refined atomic parameters for the model in space group $Pna2_1$. . . 76
4.10 Bond lengths and valences of the polyhedra of the structure model in space group $Pna2_1$ 78
4.11 Refined atomic parameters for the model in space group $P222$. . . . 80
4.12 Bond lengths and valences of the polyhedra of the structure model in space group $P222$ 81
4.13 Refined atomic parameters for the model in space group $P222_1$. . . . 84
4.14 Bond lengths and valences of the polyhedra of the structure model in space group $P222_1$ 84
4.15 Geometrical parameters of the polyhedra model in space group $Pnam$ and with refined B_{eq} values. 86
4.16 Refined atomic parameters for the model in $Pnam$. 88
4.17 Bond lengths and valences of the polyhedra of the structure model in space group $Pnam$ 88
4.18 Refined atomic parameters for the model in space group $Pnam$ with refined B_{eq}-values. 91
4.19 Bond lengths and valences of the polyhedra of the structure model in space group $Pnam$ with refined B_{eq}-values. 91
4.20 Geometrical parameters of the polyhedra model in space group $P2_1/n$ from our combined refinements and as published (denoted with §). . 93
4.21 Refined atomic parameters for the model in space group $P2_1/n$. . . . 93
4.22 Bond lengths and valences of the polyhedra of the structure model in space group $P2_1/n$ as published by Wang, Sun et al. [96] 95

4.23 Bond lengths and valences of the polyhedra of the structure model in space group $P2_1/n$ from our combined refinement 95

List of Abbreviations

2D two-dimensional. 1, 5, 11, 30
3D three-dimensional. 1, 5, 20, 26
ADP atomic displacement parameter. 10
ATR attenuated total reflection. 32, 53, 54
BVS bond valence sum. 41, 44
CV cyclovoltammetry. v
DFT density-functional theory. v, 22, 25
DSC differential scanning calorimetry. 10, 14, 27, 34, 36
DTA differential thermal analysis. 10
EDX energy dispersive X-ray spectroscopy. 28, 34
FIB focus ion beam. 47
FTIR Fourier-transform infrared spectroscopy. 32, 33, 50, 51, 53, 54, 76
HOMO highest occupied molecular orbital. 4
HT high-temperature. 4, 30, 35–37, 39, 40
HTB hexagonal tungsten bronze. 25
ITB intergrowth tungsten bronze. 25
JTE Jahn-Teller effect. 4
LT low-temperature. 4, 5, 14, 30, 35–39, 44
LUMO lowest unoccupied molecular orbital. 4
MAS magic-angle spinning. 47, 49
MBE minimal bounding ellispoid. 31, 36
NMR nuclear magnetic resonance. v, 33, 47, 49, 56, 76
NPD neutron powder diffraction. v, 10, 41
NPDF neutron radiation pair-distribution function. v
PDF pair distribution function. v, 10, 21, 22, 24, 44
PJTE pseudo Jahn-Teller effect. 2, 4
PT phase transition. 5, 41
PTB perovskite-type tungsten bronze. 23, 25
RCs related compounds. 59, 61, 65, 87
RP Ruddlesden-Popper. 16–20, 24
RT room-temperature. 10, 18, 29, 36, 39
SC single-crystal. 14
SEM scanning electron microscopy. 34, 46
SG space group. 1, 3, 4, 16, 19
SHG second-harmonic generation. v, 33, 54
SNR signal-to-noise ratio. 37, 53
SOJTE second-order Jahn-Teller effect. 4, 8, 10

TD temperature-dependent. 36
TEM transmission electron microscopy. v, 21, 34, 46
UV ultraviolet. 26, 33
vdW van-der-Waals. 20
VSEPR valence structure electron pair repulsion. 8
XPD X-ray powder diffraction. 22, 28, 45
XRD X-ray diffraction. 10, 13, 14, 47

Bibliography

[1] P. M. Woodward, A. W. Sleight, T. Vogt, *Journal of Physics and Chemistry of Solids* **1995**, *56*, 1305–1315, DOI 10.1016/0022-3697(95)00063-1.

[2] K. Meisel, *Z. Anorg. Allg. Chem.* **1932**, *207*, 121–128, DOI 10.1002/zaac.19322070113.

[3] T.-S. Chang, P. Trucano, *J Appl Crystallogr* **1978**, *11*, 286–288, DOI 10.1107/s0021889878013333.

[4] M. M. Vijatovic Petrovic, J. D. Bobic in *Magnetic, Ferroelectric, and Multiferroic Metal Oxides*, (Ed.: B. D. Stojanovic), Metal Oxides, Elsevier, **2018**, pp. 35–49, DOI 10.1016/B978-0-12-811180-2.00002-5.

[5] V. M. Goldschmidt, *Naturwissenschaften* **1926**, *14*, 477–485, DOI 10.1007/bf01507527.

[6] R. J. D. Tilley, *Perovskites: Structure–Property Relationships*, 1st ed., Wiley, **2016**, DOI 10.1002/9781118935651.

[7] M. Kunz, I. Brown, *Journal of Solid State Chemistry* **1995**, *115*, 395–406, DOI 10.1006/jssc.1995.1150.

[8] I. B. Bersuker, *Chem. Rev.* **2013**, *113*, 1351–1390, DOI 10.1021/cr300279n.

[9] I. B. Bersuker, *Chem. Rev.* **2021**, *121*, 1463–1512, DOI 10.1021/acs.chemrev.0c00718.

[10] A. M. Glazer, *Acta Cryst B* **1972**, *28*, 3384–3392, DOI 10.1107/S0567740872007976.

[11] P. M. Woodward, *Acta Cryst B* **1997**, *53*, 32–43, DOI 10.1107/S0108768196010713.

[12] C. J. Howard, H. T. Stokes, *Acta Crystallogr B Struct Sci* **1998**, *54*, 782–789, DOI 10.1107/s0108768198004200.

[13] P. M. Woodward, *Acta Cryst B* **1997**, *53*, 44–66, DOI 10.1107/S0108768196012050.

[14] H. Hamdi et al., *Phys. Rev. B* **2016**, *94*, 245124, DOI 10.1103/PhysRevB.94.245124.

[15] P. Woodward, A. Sleight, T. Vogt, *Journal of Solid State Chemistry* **1997**, *131*, 9–17, DOI 10.1006/jssc.1997.7268.

[16] C. J. Howard, V. Luca, K. S. Knight, *J. Phys.: Condens. Matter* **2001**, *14*, 377, DOI 10.1088/0953-8984/14/3/308.

[17] I. Lefkowitz, M. B. Dowell, M. A. Shields, *Journal of Solid State Chemistry* **1975**, *15*, 24–39, DOI 10.1016/0022-4596(75)90267-4.

[18] P. Roussel, P. Labbé, D. Groult, *Acta Crystallogr B Struct Sci* **2000**, *56*, 377–391, DOI 10.1107/s0108768199016195.

[19] S. Ayyappan, G. N. Subbanna, C. N. R. Rao, *Chem. Eur. J.* **1995**, *1*, 165–170, DOI 10.1002/chem.19950010305.

[20] C. Balázsi et al., *Solid State Ionics*, XIV International Symposium on the Reactivity of Solids **2001**, *141–142*, 411–416, DOI 10.1016/S0167-2738(01)00806-2.

[21] B. O. Loopstra, P. Boldrini, *Acta Cryst* **1966**, *21*, 158–162, DOI 10.1107/S0365110X66002469.

[22] B. O. Loopstra, H. M. Rietveld, *Acta Cryst B* **1969**, *25*, 1420–1421, DOI 10.1107/S0567740869004146.

[23] B. Aurivillius, *Ark. Kemi* **1949**, *1*, 463–480.

[24] B. Aurivillius, *Ark. Kemi* **1949**, *1*, 499–512.

[25] B. Aurivillius, *Ark. Kemi* **1950**, *2*, 519–527.

[26] E. C. Subbarao, *J. Am. Ceram. Soc.* **1962**, *45*, 166–169, DOI 10.1111/j.1151-2916.1962.tb11113.x.

[27] T. Jardiel, A. C. Caballero, M. Villegas, *J. Ceram. Soc. Jpn.* **2008**, *116*, 511–518, DOI 10.2109/jcersj2.116.511.

[28] T. Kikuchi, *Materials Research Bulletin* **1979**, *14*, 1561–1569, DOI 10.1016/0025-5408(72)90226-7.

[29] P. Millan, A. Ramirez, A. Castro, *J Mater Sci Lett* **1995**, *14*, 1657–1660, DOI 10.1007/BF00422667.

[30] M. García-Guaderrama et al., *Materials Research Bulletin* **2012**, *47*, 3850–3854, DOI 10.1016/j.materresbull.2012.08.038.

[31] S. Luo et al., *Materials Research Bulletin* **2001**, *36*, 531–540, DOI 10.1016/S0025-5408(01)00516-5.

[32] R. Wolfe, R. Newnahm, M. Kay, *Solid State Commun.* **1969**, *7*, 1797–1801, DOI 10.1016/0038-1098(69)90288-9.

[33] K. S. Knight, *Mineral. mag.* **1992**, *56*, 399–409, DOI 10.1180/minmag.1992.056.384.13.

[34] N. A. McDowell, K. S. Knight, P. Lightfoot, *Chem. - Eur. J.* **2006**, *12*, 1493–1499, DOI 10.1002/chem.200500904.

[35] P. S. Halasyamani, *Chem. Mater.* **2004**, *16*, 3586–3592, DOI 10.1021/cm049297g.

[36] H. Okudera et al., *Acta Crystallogr B Struct Sci Cryst Eng Mater* **2018**, *74*, 295–303, DOI 10.1107/s2052520618006133.

[37] H. Djani, E. Bousquet et al., *Phys. Rev. B* **2012**, *86*, 054107, DOI 10.1103/PhysRevB.86.054107.

[38] O. C. Gagné, F. C. Hawthorne, *Acta Cryst B* **2018**, *74*, 79–96, DOI 10.1107/S2052520617017541.

[39] J. Galy et al., *Journal of Solid State Chemistry* **1975**, *13*, 142–159, DOI 10.1016/0022-4596(75)90092-4.

[40] C. Pirovano et al., *Solid State Ionics* **2001**, *140*, 115–123, DOI 10.1016/S0167-2738(01)00699-3.

[41] M. W. Stoltzfus et al., *Inorg. Chem.* **2007**, *46*, 3839–3850, DOI 10.1021/ic061157g.

[42] C. E. Mohn, S. Stølen, *Phys. Rev. B* **2011**, *83*, 014103, DOI 10.1103/PhysRevB.83.014103.

[43] Y. Yoneda, S. Kohara et al., *Jpn. J. Appl. Phys.* **2012**, *51*, 09LE06, DOI 10.1143/jjap.51.09le06.

[44] Y. Yoneda, H. Takeda, T. Tsurumi in *Proceedings of the 12th Asia Pacific Physics Conference (APPC12)*, JPS Conference Proceedings 1, Journal of the Physical Society of Japan, **2014**, DOI 10.7566/JPSCP.1.012103.

[45] T. Hirose, M. Kawaminami, K. Obara, *Phys. Status Solidi A* **1991**, *124*, 137–146, DOI 10.1002/pssa.2211240112.

[46] A. Watanabe, *J. Solid State Chem.* **1982**, *41*, 160–165, DOI 10.1016/0022-4596(82)90198-0.

[47] V. K. Yanovskii, V. I. Voronkova, *Phys. Status Solidi A* **1986**, *93*, 57–66, DOI 10.1002/pssa.2210930106.

[48] V. I. Voronkova, E. P. Kharitonova, O. G. Rudnitskaya, *Journal of Alloys and Compounds* **2009**, *487*, 274–279, DOI 10.1016/j.jallcom.2009.07.101.

[49] K. S. Knight, *Ferroelectrics* **1993**, *150*, 319–330, DOI 10.1080/00150199308211450.

[50] P. S. Berdonosov et al., *Journal of Solid State Chemistry* **2004**, *177*, 2632–2634, DOI 10.1016/j.jssc.2004.03.004.

[51] V. Yanovskii, V. Voronkova et al., *Dokl. Akad. Nauk SSSR*, Struktura i Svojstva Segnetoehlektricheskikh Kristallov Bi2WO6 **1975**, *222*, 94–95.

[52] X. Tian et al., *CrystEngComm* **2018**, *20*, 2669–2680, DOI 10.1039/c8ce00189h.

[53] A. Castro et al., *Chem. Mater.* **2003**, *15*, 3395–3401, DOI 10.1021/cm030224r.

[54] L. Zhou et al., *J. Phys. Chem. C* **2010**, *114*, 18812–18818, DOI 10.1021/jp107061p.

[55] A. Watanabe, M. Goto, *J. Common Met.* **1978**, *61*, 265–272, DOI 10.1016/0022-5088(78)90222-9.

[56] Y. Bando et al., *Acta Cryst A* **1979**, *35*, 142–145, DOI 10.1107/S0567739479000255.

[57] J.-C. Champarnaud-Mesjard, B. Frit, A. Watanabe, *J. Mater. Chem.* **1999**, *9*, 1319–1322, DOI 10.1039/a900992b.

[58] H. Djani, E. E. McCabe et al., *Phys. Rev. B* **2020**, *101*, DOI 10.1103/physrevb.101.134113.

[59] M. Mączka, L. Macalik, S. Kojima, *J. Phys.: Condens. Matter* **2011**, *23*, 405902, DOI 10.1088/0953-8984/23/40/405902.

[60] M. Maczka, W. Paraguassu et al., *Phys. Rev. B* **2010**, *81*, 104301, DOI 10.1103/physrevb.81.104301.

[61] H.-Y. Chen, A. W. Sleight, *Journal of Solid State Chemistry* **1986**, *63*, 70–75, DOI 10.1016/0022-4596(86)90153-2.

[62] S. N. Ruddlesden, P. Popper, *Acta Crystallogr.* **1957**, *10*, 538–539, DOI 10.1107/S0365110X57001929.

[63] S. N. Ruddlesden, P. Popper, *Acta Crystallogr.* **1958**, *11*, 54–55, DOI 10.1107/S0365110X58000128.

[64] P. D. Battle et al., *Chem. Mater.* **1998**, *10*, 658–664, DOI 10.1021/cm970647r.

[65] B. V. Beznosikov, K. S. Aleksandrov, *Crystallogr. Rep.* **2000**, *45*, 792–798, DOI 10.1134/1.1312923.

[66] L. Glasser, *Inorg. Chem.* **2017**, *56*, 8920–8925, DOI 10.1021/acs.inorgchem.7b00884.

[67] C.-H. Lee et al., *Appl. Phys. Lett.* **2013**, *102*, 122901, DOI 10.1063/1.4798241.

[68] B.-H. Chen, *Journal of Solid State Chemistry* **1996**, *125*, 63–66, DOI 10.1006/jssc.1996.0265.

[69] J. G. Bednorz, K. A. Müller, *Z. Physik B - Condensed Matter* **1986**, *64*, 189–193, DOI 10.1007/BF01303701.

[70] R. E. Schaak, T. E. Mallouk, *Chem. Mater.* **2002**, *14*, 1455–1471, DOI 10.1021/cm010689m.

[71] Z. Cheng, J. Lin, *CrystEngComm* **2010**, *12*, 2646–2662, DOI 10.1039/C001929A.

[72] M. Lehtimäki, H. Yamauchi, M. Karppinen, *J. Solid State Chem.* **2013**, *204*, 95–101, DOI 10.1016/j.jssc.2013.05.012.

[73] B. Raveau in *Comprehensive Inorganic Chemistry II*, Elsevier, **2013**, pp. 63–102.

[74] W. H. Zachariasen, H. A. Plettinger, *Acta Cryst* **1961**, *14*, 229–230, DOI 10.1107/S0365110X61000772.

[75] I. Lindqvist et al., *Acta Chem. Scand.* **1950**, *4*, 1066–1074, DOI 10.3891/acta.chem.scand.04-1066.

[76] A. S. Koster, F. X. N. M. Kools, G. D. Rieck, *Acta Cryst B* **1969**, *25*, 1704–1708, DOI 10.1107/S0567740869004602.

[77] F. X. N. M. Kools, A. S. Koster, G. D. Rieck, *Acta Cryst B* **1970**, *26*, 1974–1977, DOI 10.1107/S0567740870005277.

[78] J. T. Szymanski, A. C. Roberts, *The Canadian Mineralogist* **1984**, *22*, 681–688.

[79] C. W. Scheele, *Sämmtliche Physische Und Chemische Werke*, (Eds.: S. F. 1.-1. Hermbstaedt, H. A. 1.-1. Rottmann), Rottmann, **1793**.

[80] W. B. Jensen, *J. Chem. Educ.* **2008**, *85*, 488, DOI 10.1021/ed085p488.

[81] M. L. Freedman, *J. Am. Chem. Soc.* **1959**, *81*, 3834–3839, DOI 10.1021/ja01524a009.

[82] H. Zocher, K. Jacobsohn, *Kolloidchem Beih* **1929**, *28*, 167–206, DOI 10.1007/BF02556733.

[83] E. Lalik et al., *J. Phys. Chem. C* **2021**, *125*, 23864–23879, DOI 10.1021/acs.jpcc.1c05121.

[84] M. Daniel et al., *J. Solid State Chem.* **1987**, *67*, 235–247, DOI 10.1016/0022-4596(87)90359-8.

[85] M. Freedman, S. Leber, *Journal of the Less Common Metals* **1964**, *7*, 427–432, DOI 10.1016/0022-5088(64)90039-6.

[86] J. B. Mitchell, W. C. Lo et al., *Chem. Mater.* **2017**, *29*, 3928–3937, DOI 10.1021/acs.chemmater.6b05485.

[87] J. B. Mitchell, N. R. Geise et al., *ACS Energy Lett.* **2019**, *4*, 2805–2812, DOI 10.1021/acsenergylett.9b02040.

[88] R. S. Mitchell, *American Mineralogist* **1963**, *48*, 935–939.

[89] B. Krebs, *Acta Crystallogr. B* **1972**, *28*, 2222–2231, DOI 10.1107/s0567740872005849.

[90] R. E. Schaak, T. E. Mallouk, *Chem. Commun.* **2002**, 706–707, DOI 10.1039/b110220f.

[91] M. Kudo, H. Ohkawa et al., *Inorg. Chem.* **2003**, *42*, 4479–4484, DOI 10.1021/ic0206746.

[92] A. M. Abakumov et al., *Chem. Mater.* **2005**, *17*, 1123–1134, DOI 10.1021/cm048791h.

[93] L. M. Kuti, S. S. Bhella, V. Thangadurai, *Inorg. Chem.* **2009**, *48*, 6804–6811, DOI 10.1021/ic900738m.

[94] P. C. Metz, R. Koch, S. T. Misture, *J Appl Crystallogr* **2018**, *51*, 1437–1444, DOI 10.1107/s1600576718011597.

[95] P. Metz, R. Koch, B. Cladek et al., *Powder Diffr.* **2016**, *31*, 126–134, DOI 10.1017/s0885715616000129.

[96] R. Wang, Y. Sun et al., *Adv. Energy Mater.* **2021**, *11*, 2003335, DOI 10.1002/aenm.202003335.

[97] B. Gerand, G. Nowogrocki, M. Figlarz, *Journal of Solid State Chemistry* **1981**, *38*, 312–320, DOI 10.1016/0022-4596(81)90062-1.

[98] B. Gerand, G. Nowogrocki, J. Guenot et al., *J. Solid State Chem.* **1979**, *29*, 429–434, DOI 10.1016/0022-4596(79)90199-3.

[99] J. R. Günter, M. Amberg, H. Schmalle, *Materials Research Bulletin* **1989**, *24*, 289–292, DOI 10.1016/0025-5408(89)90214-6.

[100] L. Seguin, M. Figlarz, J. Pannetier, *Solid State Ionics* **1993**, *63–65*, 437–441, DOI 10.1016/0167-2738(93)90141-O.

[101] M. Figlarz, *Progress in Solid State Chemistry* **1989**, *19*, 1–46, DOI 10.1016/0079-6786(89)90005-8.

[102] A. Coucou, M. Figlarz, *Solid State Ionics* **1988**, *28–30*, 1762–1765, DOI 10.1016/0167-2738(88)90457-2.

[103] F. Wöhler, *Ann. Phys. phys. Chem.* **1824**, *78*, 345–358, DOI 10.1002/andp.18240781202.

[104] P. G. Dickens, M. S. Whittingham, *Q. Rev. Chem. Soc.* **1968**, *22*, 30, DOI 10.1039/qr9682200030.

[105] H.-J. Lunk, H. Hartl, *ChemTexts* **2019**, *5*, 15, DOI 10.1007/s40828-019-0088-1.

[106] B. Ingham et al., *Phys. Rev. B* **2005**, *72*, 075109, DOI 10.1103/PhysRevB.72.075109.

[107] P. J. Wiseman, P. G. Dickens, *Journal of Solid State Chemistry* **1973**, *6*, 374–377, DOI 10.1016/0022-4596(73)90225-9.

[108] A. Hjelm, C. G. Granqvist, J. M. Wills, *Phys. Rev. B* **1996**, *54*, 2436–2445, DOI 10.1103/PhysRevB.54.2436.

[109] H. Lin et al., *J. Mater. Chem. A* **2014**, *2*, 12280–12288, DOI 10.1039/C4TA02465F.

[110] R. J. D. Tilley, *International Journal of Refractory Metals and Hard Materials*, The Chemistry of Non-sag Tungsten **1995**, *13*, 93–109, DOI 10.1016/0263-4368(95)00004-6.

[111] K. S. Aleksandrov, V. V. Beznosikov, *Phys. Solid State* **1997**, *39*, 695–715, DOI 10.1134/1.1130120.

[112] S. K. Deb, *Solar Energy Materials and Solar Cells*, Selected Papers from the Seventh International Meeting on Electrochromism (IME-7) **2008**, *92*, 245–258, DOI 10.1016/j.solmat.2007.01.026.

[113] C. G. Granqvist, *Solar Energy Materials and Solar Cells* **2000**, *60*, 201–262, DOI 10.1016/S0927-0248(99)00088-4.

[114] S. Hashimoto, H. Matsuoka, *J. Appl. Phys.* **1991**, *69*, 933, DOI 10.1063/1.347335.

[115] H. Quan, Y. Gao, W. Wang, *Inorg. Chem. Front.* **2020**, *7*, 817–838, DOI 10.1039/C9QI01516G.

[116] Z.-F. Huang et al., *Adv. Mater.* **2015**, *27*, 5309–5327, DOI 10.1002/adma.201501217.

[117] A. Shengelaya, K. Conder, K. A. Müller, *J Supercond Nov Magn* **2020**, *33*, 301–306, DOI 10.1007/s10948-019-05329-9.

[118] S. Reich, Y. Tsabba, *Eur. Phys. J. B* **1999**, *9*, 1–4, DOI 10.1007/s100510050735.

[119] S. Reich, G. Leitus et al., *J Supercond Nov Magn* **2009**, *22*, 343–346, DOI 10.1007/s10948-009-0443-3.

[120] H. Zheng et al., *Adv. Funct. Mater.* **2011**, *21*, 2175–2196, DOI 10.1002/adfm.201002477.

[121] H. I. Nogueira et al., *Materials Research Bulletin* **2004**, *39*, 683–693, DOI 10.1016/j.materresbull.2003.11.004.

[122] F. Kishimoto et al., *RSC Adv.* **2015**, *5*, 77839–77846, DOI 10.1039/C5RA15167H.

[123] D. Chen, H. Wen et al., *Materials Chemistry and Physics* **2009**, *116*, 507–513, DOI 10.1016/j.matchemphys.2009.04.024.

[124] D. Chen, Y. Sugahara, *Chem. Mater.* **2007**, *19*, 1808–1815, DOI 10.1021/cm062039u.

[125] Z. Wang, S. Zhou, L. Wu, *Adv. Funct. Mater.* **2007**, *17*, 1790–1794, DOI 10.1002/adfm.200601195.

[126] Z. Gu et al., *J. Phys. Chem. B* **2006**, *110*, 23829–23836, DOI 10.1021/jp065170y.

[127] J. Yin et al., *Crystal Growth & Design* **2013**, *13*, 759–769, DOI 10.1021/cg301469u.

[128] B. Wang, X. Dong et al., *J. Solid State Chem.* **2007**, *180*, 1125–1129, DOI 10.1016/j.jssc.2007.01.009.

[129] T. G. Novak et al., *Nanoscale Adv.* **2021**, *3*, 5166–5182, DOI 10.1039/D1NA00384D.

[130] L. Liang et al., *Sci Rep* **2013**, *3*, 1936, DOI 10.1038/srep01936.

[131] P. G. Dickens, S. A. Kay et al., *Solid State Ionics* **1987**, *23*, 9–14, DOI 10.1016/0167-2738(87)90075-0.

[132] J. B. Mitchell, R. Wang et al., *J. Electrochem. Soc.* **2022**, *169*, 030534, DOI 10.1149/1945-7111/ac58c8.

[133] H. Suzuki et al., *J. Mater. Chem. A* **2017**, *5*, 10280–10288, DOI 10.1039/C7TA01228D.

[134] K. R. Kendall et al., *Chem. Mater.* **1996**, *8*, 642–649, DOI 10.1021/cm9503083.

[135] T. R. Pope et al., *J. Mater. Chem. C* **2014**, *2*, 3223–3230, DOI 10.1039/C3TC32070G.

[136] R. Iimura, T. Hasegawa, S. Yin, *Inorg. Chem.* **2022**, *61*, 2509–2516, DOI 10.1021/acs.inorgchem.1c03364.

[137] J. Tang, Z. Zou, J. Ye, *Catalysis Letters* **2004**, *92*, 53–56, DOI 10.1023/B:CATL.0000011086.20412.aa.

[138] M. Teck et al., *J. Solid State Chem.* **2017**, *254*, 82–89, DOI 10.1016/j.jssc.2017.07.013.

[139] T. M. Khedr et al., *Journal of Environmental Chemical Engineering* **2022**, *10*, 107838, DOI 10.1016/j.jece.2022.107838.

[140] A. Kudo, S. Hijii, *Chem. Lett.* **1999**, *28*, 1103–1104, DOI 10.1246/cl.1999.1103.

[141] J. Tang, J. Ye, *J. Mater. Chem.* **2005**, *15*, 4246–4251, DOI 10.1039/B504818D.

[142] J. Kieffer, D. Karkoulis, *J. Phys.: Conf. Ser.* **2013**, *425*, 202012, DOI 10.1088/1742-6596/425/20/202012.

[143] M. Hoelzel et al., *Nucl. Instrum. Methods Phys. Res. Sect. Accel. Spectrometers Detect. Assoc. Equip.* **2012**, *667*, 32–37, DOI 10.1016/j.nima.2011.11.070.

[144] K. Momma, F. Izumi, *J. Appl. Crystallogr.* **2011**, *44*, 1272–1276, DOI 10.1107/s0021889811038970.

[145] A. Hjorth Larsen et al., *J. Phys.: Condens. Matter* **2017**, *29*, 273002, DOI 10.1088/1361-648X/aa680e.

[146] I. D. Brown, D. Altermatt, *Acta Crystallogr B Struct Sci* **1985**, *41*, 244–247, DOI 10.1107/S0108768185002063.

[147] J. Cumby, J. P. Attfield, *Nat Commun* **2017**, *8*, 14235, DOI 10.1038/ncomms14235.

[148] K. Robinson, G. V. Gibbs, P. H. Ribbe, *Science* **1971**, *172*, 567–570, DOI 10.1126/science.172.3983.567.

[149] W. H. Baur, *Acta Crystallogr B Struct Sci* **1974**, *30*, 1195–1215, DOI 10.1107/S0567740874004560.

[150] I. D. Brown, R. D. Shannon, *Acta Cryst A* **1973**, *29*, 266–282, DOI 10.1107/S0567739473000689.

[151] L. Bayarjargal et al., *Physics of the Earth and Planetary Interiors* **2018**, *281*, 31–45, DOI 10.1016/j.pepi.2018.05.002.

[152] D. Richard, M. Ferrand, G. J. Kearley, *J. of Neutron Res.* **1996**, *4*, 33–39, DOI 10.1080/10238169608200065.

[153] M. Newville et al., *LMFIT: Non-Linear Least-Square Minimization and Curve-Fitting for Python*, version 0.8.0, Zenodo, **2014**, DOI 10.5281/ZENODO.11813.

[154] M. Wojdyr, *J Appl Crystallogr* **2010**, *43*, 1126–1128, DOI 10.1107/S0021889810030499.

[155] L. Robben, *Z. Für Krist. - Cryst. Mater.* **2017**, *232*, 267–277, DOI 10.1515/zkri-2016-2000.

[156] M. Maczka, J. Hanuza et al., *Appl. Phys. Lett.* **2008**, *92*, 112911, DOI 10.1063/1.2896312.

[157] I. D. Brown, *Journal of Solid State Chemistry* **1989**, *82*, 122–131, DOI 10.1016/0022-4596(89)90231-4.

[158] B. Reif et al., *Nat Rev Methods Primers* **2021**, *1*, 1–23, DOI 10.1038/s43586-020-00002-1.

[159] M. G. Shelyapina et al., *Ceramics International* **2019**, *45*, 5788–5795, DOI 10.1016/j.ceramint.2018.12.045.

[160] K. Chen, *IJMS* **2020**, *21*, 5666, DOI 10.3390/ijms21165666.

[161] S. Tani et al., *Journal of Solid State Chemistry* **2006**, *179*, 3357–3364, DOI 10.1016/j.jssc.2006.06.030.

[162] M. Mączka, L. Macalik, J. Hanuza, *J. Raman Spectrosc.* **2009**, *40*, 2099–2103, DOI 10.1002/jrs.2378.

[163] S. K. Kurtz, T. T. Perry, *J. Appl. Phys.* **1968**, *39*, 3798–3813, DOI 10.1063/1.1656857.

[164] O. C. Gagné, F. C. Hawthorne, *IUCrJ* **2020**, *7*, 581–629, DOI 10.1107/S2052252520005928.

[165] G. S. Chandler, M. Wajrak, R. N. Khan, *Acta Cryst B* **2015**, *71*, 275–284, DOI 10.1107/S2052520615005387.

[166] K. Kamata et al., *Inorg. Chem.* **2007**, *46*, 3768–3774, DOI 10.1021/ic0701211.

[167] S.-Y. Hou et al., *Eur. J. Inorg. Chem.* **2006**, *2006*, 1670–1677, DOI 10.1002/ejic.200501008.